Roughness dependence of phonon-interface thermal transport: Theoretical model and Monte Carlo simulation

Xin Ran and Bingyang Cao*

Key Laboratory for Thermal Science and Power Engineering of Ministry of Education, Department of Engineering Mechanics, Tsinghua University, Beijing 100084, China

(Received 8 November 2023; revised 29 April 2024; accepted 28 May 2024; published 1 July 2024)

Recently, researchers have shown that nanostructured interfaces can manipulate the thermal boundary conductance at the interface, but their conclusions are contradictory, and mechanisms are unclear. In this paper, we investigate the impact of nanostructured interfaces on thermal boundary conductance by considering roughness dependence. To achieve this goal, first, an interface model accounting for spectral specularity and spectral specular and spectral diffuse scatterings is deduced. Next, the Monte Carlo framework of interface treatment for spectral specularity and spectral specular and spectral diffuse scatterings at heterogeneous interfaces is constructed. Then they are validated through comparisons with the discrete-ordinates method and experiments. Finally, the roughness dependence for thermal transport through planar and nanostructured interfaces is studied. Results give a nonmonotonic relationship between thermal boundary conductance and roughness for planar interface, and the manipulation of thermal boundary conductance by nanostructured interfaces depends on the system and interface geometries and the interface roughness. The effect of interface roughness is found to be the dominant impact factor in films with a thickness of tens of nanometers. Further investigations for these small-scale films show that the roughness of their horizontal and vertical interfaces impact thermal boundary conductance differently. Thus, the nonuniform roughness for horizontal and vertical interfaces is proposed to successfully expand the manipulation of thermal boundary conductance in films with small size.

DOI: 10.1103/PhysRevB.110.024302

I. INTRODUCTION

Interfaces may dominate thermal transport in current micro/nanoscale electronics and thermoelectrics [1,2]. Manipulation of interfacial phonon transport is crucial for the efficient thermal management of electronics and the optimization of thermoelectrics. Thermal boundary conductance, the reciprocal of thermal boundary resistance, is a key physical quantity measuring the ability of thermal transport across the interface, defined as the ratio of the heat flux across the interface over the temperature jump at the interface [3]. Small thermal boundary conductance results in the accumulation of thermal energy near the interface and the increase in the temperature of electronics, possibly leading to failures [4]. On the contrary, small thermal boundary conductance enhances the figure of merit of thermoelectrics and thus their efficiencies [5]. Therefore, increasing or decreasing thermal boundary conductance is an important means to achieve the efficient thermal management of electronics and the optimization of thermoelectrics.

Previous researchers have shown that nanostructured interfaces can effectively manipulate thermal boundary conductance, but their conclusions are contradictory, and mechanisms are unclear [6–12]. In detail, the molecular dynamics method was taken to simulate phonon transport through nanopillar interfaces, and thermal boundary conductances were found to be enhanced by these nanostructured interfaces [8]. An analytical relationship between thermal boundary conductance and structural features of nanostructured interfaces was developed based on the molecular dynamics method, and it also found that nanostructured interfaces could enhance thermal boundary conductance [9]. Some experiments and simulations confirmed the enhancement of thermal boundary conductance by nanostructured interfaces [11,13–16]. Furthermore, through combining analytical and molecular dynamics methods, the nanostructured interface was optimized to further increase thermal boundary conductance [10], and the impact of shape of nanostructured interfaces on the thermal boundary conductance enhancement was discussed by combining the phonon lattice Boltzmann method and the molecular dynamics method [17]. All the above researchers mainly attributed the enhancement through nanostructured interfaces to the additional thermal conduction pathway caused by the increase of contact area. On the contrary, it was found that the nanostructured interface could reduce thermal boundary conductance through Monte Carlo simulation [12]. Some experiments also derived the negative relationship between contact area and thermal boundary conductance by generating rough interfaces, which should increase the contact area as well [6,7]. Unlike the explanation of the thermal boundary conductance enhancement by the increase of contact area, the reduction is attributed to the increased resistive scattering. Therefore, it is necessary to further investigate the impact of

*Contact author: caoby@tsinghua.edu.cn

nanostructured interfaces on thermal boundary conductance and reveal the underlying mechanisms to better manipulate thermal boundary conductance using nanostructured interfaces.

A phonon interacting with the interface will either transmit or be reflected, quantified by its transmissivity, defined as the probability of phonon transmitting across the interface. There are generally two classical models for the phonon transmissivity, namely, acoustic mismatch model (AMM) [18] and diffuse mismatch model (DMM) [19]. AMM treated the interface as a completely smooth plane and phonons as the plane waves completely specularly scattered by the interface. It usually worked well at very low temperatures where the wavelengths of most phonons were extremely larger than the size of the interface asperity [18]. DMM treated the interface as a completely rough plane and phonons as the particles completely diffusely scattered by the interface. It often worked well at higher temperatures where the wavelengths of most phonons were comparable with or smaller than the size of the interface asperity [19]. The mixed mismatch model (MMM) based on the classical AMM and DMM was developed by assuming that phonons are partially specularly and partially diffusely scattered by the interface after introducing the specularity, defined as the probability of specular scattering and related to the interface roughness [20]. It worked well within a wider temperature range than AMM and DMM. These classical models all assumed that both specularity and phonon transmissivity were frequency independent [18–20]. However, both experiments and simulations indicated the spectral dependence of specularity and phonon transmissivity [21–23]. Thus, various interface models accounting for either completely spectral diffuse scattering or completely spectral specular scattering were developed under various assumptions and better predicted thermal boundary conductance, referred to spectral AMMs (SAMMs) and spectral DMMs (SDMMs) [24,25]. Recently, interface models considering the spectral specularity were developed through the weighted average of AMM and DMM or SAMMs and SDMMs, better predicting the measured phonon transmissivity [26–28]. However, on the one hand, either both specular and diffuse scatterings or one of them is frequency independent in these models [26–28]. On the other hand, the weighted average of AMM and DMM or SAMMs and SDMMs fails to satisfy the principle of detailed balance for spectral specularity. Therefore, there is still a lack of an interface model that considers spectral specularity and spectral specular and spectral diffuse scatterings and satisfies the principle of detailed balance to better understand interfacial phonon transport.

Many methods have been used in the research of interfacial phonon transport, mainly including the microscopic method [29–36], the mesoscopic method [37–40], and experiment [41–43]. Microscopic methods contain the molecular dynamics method [31,33,36], the Green's function method [30,32], the lattice dynamics method [34,35], etc. These methods are only suitable for small systems and computationally expensive for large systems. Experiments for interfacial phonon transport are challenging and not good at analyzing the detailed mechanisms. Mesoscopic methods are based on directly solving the phonon Boltzmann transport equation and suitable for larger systems, mainly including the deterministic method [37,38,40] and the statistical method [39,44]. The former is difficult for high-dimensional systems or systems with complex interfaces. The latter, also called the Monte Carlo method, can easily treat high-dimensional systems or systems with complex interfaces. The Monte Carlo framework of the treatment for the heterogeneous interface with frequency-independent phonon transmissivity was first established to simulate the thermal conductivity of nanoparticle composites [39]. Frequency-independent specularity and phonon transmissivity at heterogeneous interfaces were then considered in the Monte Carlo method for phonon transport across superlattice or nanostructured interfaces [45,46]. The Monte Carlo framework considering spectral specularity and spectral phonon transmissivity at homogenous interfaces was proposed for phonon transport in polycrystalline materials [44]. Based on SDMM, the Monte Carlo framework considering spectral phonon transmissivity at heterogeneous interfaces was then constructed [12]. Recently, spectral specularity and frequency-independent specular and spectral diffuse scatterings at heterogeneous interfaces were considered in the Monte Carlo method [28]. However, there is still a need to develop a Monte Carlo framework for spectral specularity and spectral specular and spectral diffuse scatterings at heterogeneous interfaces to further study interfacial phonon transport.

The goal of this paper is to investigate the impact of nanostructured interfaces on thermal boundary conductance by considering roughness dependence and giving the underlying mechanisms. To achieve this, an interface model and Monte Carlo framework accounting for spectral specularity and spectral specular and spectral diffuse scatterings at the interface will be deduced first in Sec. II. Next, they will be validated in Sec. III by comparisons with the discrete-ordinates method and experiments. Then Sec. IV will give the results and discussions, including spectral and angular-dependent transmissivity as well as phonon transport through planar interfaces and nanostructured interfaces with uniform and nonuniform roughnesses. Finally, Sec. V will remark on the conclusions.

II. THEORETICAL MODEL AND NUMERICAL METHOD

In this section, an interface model, called the spectral MMM (SMMM), and the Monte Carlo framework are derived sequentially. The interface model accounting for spectral specularity and spectral specular and spectral diffuse scatterings is first deduced based on partially specular and partially diffuse scattering. Then the Monte Carlo framework for spectral specularity and spectral specular and spectral diffuse scatterings at heterogeneous interfaces is developed based on SMMM.

A. SMMM

First, the SMMM accounting for spectral specularity and spectral specular and spectral diffuse scatterings is deduced. Phonons scattered by an interface will either transmit across the interface or be reflected, and according to the energy conservation law for interface scattering, the following equations

hold:

$$\alpha_{ij}(\theta_i, \omega, \mathrm{p}) = P_i(\omega, \mathrm{p})\alpha_{\mathrm{Specular},ij}(\theta_i, \omega, \mathrm{p}) + [1 - P_i(\omega, \mathrm{p})]\alpha_{\mathrm{Diffuse},ij}(\omega, \mathrm{p}), \tag{1}$$

$$\alpha_{ji}(\theta_j, \omega, \mathrm{p}) = P_j(\omega, \mathrm{p})\alpha_{\mathrm{Specular},ji}(\theta_j, \omega, \mathrm{p}) + [1 - P_j(\omega, \mathrm{p})]\alpha_{\mathrm{Diffuse},ji}(\omega, \mathrm{p}), \tag{2}$$

where α_{ij} and α_{ji} denote the total phonon transmissivity from side i to j and that in the reverse direction, respectively, with side labels i and j; $\alpha_{\mathrm{Specular},ij}$ and $\alpha_{\mathrm{Specular},ji}$ denote the phonon transmissivity for specular interface scattering from side i to j and that in the reverse direction, respectively; $\alpha_{\mathrm{Diffuse},ij}$ and $\alpha_{\mathrm{Diffuse},ji}$ denote the phonon transmissivity for diffuse interface scattering from side i to j and that in the reverse direction, respectively; P is the specularity; ω and p represent phonon angular frequency and polarization; and θ_i and θ_j represent the incident angles for the scattered phonons on sides i and j. The heat flux from side i to j is given as

$$q_{i\to j} = 2\pi \sum_{\mathrm{p}} \int_0^{\pi/2} \int_0^{\omega_{\mathrm{max,p},i}} \alpha_{ij}(\theta_i, \omega, \mathrm{p})\hbar\omega f(\omega, T_{\mathrm{e},i}) D_i(\omega, \mathrm{p}) v_{\mathrm{g},i}(\omega, \mathrm{p}) \cos\theta_i \sin\theta_i d\omega d\theta_i, \tag{3}$$

where $D_i(\omega, \mathrm{p})$ and $v_{\mathrm{g},i}$ denote the density of states and group velocity of the material on side i; $\omega_{\mathrm{max,p},i}$ is the maximum angular frequency of polarization p on side i; and $f(\omega, T_{\mathrm{e},i}) = 1/[\exp(\frac{\hbar\omega}{k_{\mathrm{B}}T_{\mathrm{e},i}}) - 1]$ represents the Bose-Einstein distribution at the emitted phonon temperature $T_{\mathrm{e},i}$ on side i with the reduced Plank's constant $\hbar$ and the Boltzmann's constant k_{B}. The definition for the emitted phonon temperature will be given in Sec. III. Similarly, the heat flux from side j to i is given as

$$q_{j\to i} = 2\pi \sum_{\mathrm{p}} \int_0^{\pi/2} \int_0^{\omega_{\mathrm{max,p},j}} \alpha_{ji}(\theta_j, \omega, \mathrm{p})\hbar\omega f(\omega, T_{\mathrm{e},j}) D_j(\omega, \mathrm{p}) v_{\mathrm{g},j}(\omega, \mathrm{p}) \cos\theta_j \sin\theta_j d\omega d\theta_j, \tag{4}$$

where $D_j(\omega, \mathrm{p})$ and $v_{\mathrm{g},j}$ denote the density of states and group velocity of the material on side j; $\omega_{\mathrm{max,p},j}$ is the maximum angular frequency of polarization p on side j; and $f(\omega, T_{\mathrm{e},j})$ represents the Bose-Einstein distribution at the emitted phonon temperature $T_{\mathrm{e},j}$ on side j. Thus, the total heat flux from side i to j is obtained as

$$\begin{aligned} q = {} & 2\pi \sum_{\mathrm{p}} \int_0^{\pi/2} \int_0^{\omega_{\mathrm{max,p},i}} \alpha_{ij}(\theta_i, \omega, \mathrm{p})\hbar\omega f(\omega, T_{\mathrm{e},i}) D_i(\omega, \mathrm{p}) v_{\mathrm{g},i}(\omega, \mathrm{p}) \cos\theta_i \sin\theta_i d\omega d\theta_i \\ & - 2\pi \sum_{\mathrm{p}} \int_0^{\pi/2} \int_0^{\omega_{\mathrm{max,p},j}} \alpha_{ji}(\theta_j, \omega, \mathrm{p})\hbar\omega f(\omega, T_{\mathrm{e},j}) D_j(\omega, \mathrm{p}) v_{\mathrm{g},j}(\omega, \mathrm{p}) \cos\theta_j \sin\theta_j d\omega d\theta_j. \end{aligned} \tag{5}$$

If the system is equilibrated at equilibrium temperature $T_{\mathrm{e},j}$, the emitted phonon temperatures on both sides equal $T_{\mathrm{e},j}$, and the total heat flux should be 0. Thus, the relation below is obtained:

$$\begin{aligned} & 2\pi \sum_{\mathrm{p}} \int_0^{\pi/2} \int_0^{\omega_{\mathrm{max,p},i}} \alpha_{ij}(\theta_i, \omega, \mathrm{p})\hbar\omega f(\omega, T_{\mathrm{e},j}) D_i(\omega, \mathrm{p}) v_{\mathrm{g},i}(\omega, \mathrm{p}) \cos\theta_i \sin\theta_i d\omega d\theta_i \\ & = 2\pi \sum_{\mathrm{p}} \int_0^{\pi/2} \int_0^{\omega_{\mathrm{max,p},j}} \alpha_{ji}(\theta_j, \omega, \mathrm{p})\hbar\omega f(\omega, T_{\mathrm{e},j}) D_j(\omega, \mathrm{p}) v_{\mathrm{g},j}(\omega, \mathrm{p}) \cos\theta_j \sin\theta_j d\omega d\theta_j. \end{aligned} \tag{6}$$

Then Eq. (5) can be rewritten as

$$q = 2\pi \sum_{\mathrm{p}} \int_0^{\pi/2} \int_0^{\omega_{\mathrm{max,p},i}} \alpha_{ij}(\theta_i, \omega, \mathrm{p})\hbar\omega [f(\omega, T_{\mathrm{e},i}) - f(\omega, T_{\mathrm{e},j})] D_i(\omega, \mathrm{p}) v_{\mathrm{g},i}(\omega, \mathrm{p}) \cos\theta_i \sin\theta_i d\omega d\theta_i. \tag{7}$$

Based on Eq. (1), Eq. (7) can be rewritten as

$$\begin{aligned} q = {} & 2\pi \sum_{\mathrm{p}} \int_0^{\pi/2} \int_0^{\omega_{\mathrm{max,p},i}} \{P_i(\omega, \mathrm{p})\alpha_{\mathrm{Specular},ij}(\theta_i, \omega, \mathrm{p}) + [1 - P_i(\omega, \mathrm{p})]\alpha_{\mathrm{Diffuse},ij}(\omega, \mathrm{p})\} \\ & \times \hbar\omega [f(\omega, T_{\mathrm{e},i}) - f(\omega, T_{\mathrm{e},j})] D_i(\omega, \mathrm{p}) v_{\mathrm{g},i}(\omega, \mathrm{p}) \cos\theta_i \sin\theta_i d\omega d\theta_i \\ = {} & 2\pi \sum_{\mathrm{p}} \int_0^{\pi/2} \int_0^{\omega_{\mathrm{max,p},i}} P_i(\omega, \mathrm{p})\alpha_{\mathrm{Specular},ij}(\theta_i, \omega, \mathrm{p})\hbar\omega [f(\omega, T_{\mathrm{e},i}) - f(\omega, T_{\mathrm{e},j})] D_i(\omega, \mathrm{p}) v_{\mathrm{g},i}(\omega, \mathrm{p}) \cos\theta_i \sin\theta_i d\omega d\theta_i \\ & + 2\pi \sum_{\mathrm{p}} \int_0^{\pi/2} \int_0^{\omega_{\mathrm{max,p},i}} [1 - P_i(\omega, \mathrm{p})]\alpha_{\mathrm{Diffuse},ij}(\omega, \mathrm{p})\hbar\omega [f(\omega, T_{\mathrm{e},i}) - f(\omega, T_{\mathrm{e},j})] D_i(\omega, \mathrm{p}) v_{\mathrm{g},i}(\omega, \mathrm{p}) \cos\theta_i \sin\theta_i d\omega d\theta_i \\ = {} & q_{\mathrm{Specular}} + q_{\mathrm{Diffuse}}, \end{aligned} \tag{8}$$

where

$$q_{\text{Specular}} = 2\pi \sum_{\text{p}} \int_0^{\pi/2} \int_0^{\omega_{\max,\text{p},i}} P_i(\omega, \text{p}) \alpha_{\text{Specular},ij}(\theta_i, \omega, \text{p}) \hbar\omega [f(\omega, T_{\text{e},i}) - f(\omega, T_{\text{e},j})] D_i(\omega, \text{p}) v_{\text{g},i}(\omega, \text{p}) \cos\theta_i \sin\theta_i d\omega d\theta_i$$

and

$$q_{\text{Diffuse}} = 2\pi \sum_{\text{p}} \int_0^{\pi/2} \int_0^{\omega_{\max,\text{p},i}} [1 - P_i(\omega, \text{p})] \alpha_{\text{Diffuse},ij}(\omega, \text{p}) \hbar\omega [f(\omega, T_{\text{e},i}) - f(\omega, T_{\text{e},j})] D_i(\omega, \text{p}) v_{\text{g},i}(\omega, \text{p}) \cos\theta_i \sin\theta_i d\omega d\theta_i$$

denote the heat fluxes induced by specular and diffuse scatterings, respectively. When the system is equilibrated at equilibrium temperature T_0, the emitted phonon temperatures on both sides should equal T_0, i.e., $T_{\text{e},i} = T_{\text{e},j} = T_0$. Then based on the relations above, the heat fluxes induced by both specular and diffuse scatterings, q_{Specular} and q_{Diffuse}, equal 0.

For the case where $T_{\text{e},i} = T_{\text{e},j} = T_0$, Eq. (5) is rewritten as

$$\begin{aligned} q =& 2\pi \sum_{\text{p}} \int_0^{\frac{\pi}{2}} \int_0^{\omega_{\max,\text{p},i}} \alpha_{ij}(\theta_i, \omega, \text{p}) \hbar\omega f(\omega, T_0) D_i(\omega, \text{p}) v_{\text{g},i}(\omega, \text{p}) \cos\theta_i \sin\theta_i d\omega d\theta_i \\ & - 2\pi \sum_{\text{p}} \int_0^{\frac{\pi}{2}} \int_0^{\omega_{\max,\text{p},j}} \alpha_{ji}(\theta_j, \omega, \text{p}) \hbar\omega f(\omega, T_0) D_j(\omega, \text{p}) v_{\text{g},j}(\omega, \text{p}) \cos\theta_j \sin\theta_j d\omega d\theta_j. \end{aligned} \tag{9}$$

After introducing a referenced equilibrium temperature T^{ref}, which is slightly lower than the equilibrium temperature T_0, Eq. (9) can be rewritten as below:

$$\begin{aligned} q =& (T_0 - T^{\text{ref}}) 2\pi \sum_{p} \int_0^{\pi/2} \int_0^{\omega_{\max,\text{p}}} \alpha_{ij}(\theta_i, \omega, \text{p}) C_i(\omega, \text{p}) v_{\text{g},i}(\omega, \text{p}) \cos\theta_i \sin\theta_i d\omega d\theta_i \\ & - (T_0 - T^{\text{ref}}) 2\pi \sum_{p} \int_0^{\pi/2} \int_0^{\omega_{\max,\text{p}}} \alpha_{ji}(\theta_j, \omega, \text{p}) C_j(\omega, \text{p}) v_{\text{g},j}(\omega, \text{p}) \cos\theta_j \sin\theta_j d\omega d\theta_j, \end{aligned} \tag{10}$$

where $C = \hbar\omega \frac{\mathrm{d}f}{\mathrm{d}T} D$ denotes the spectral heat capacity. Based on Eqs. (1), (2), and (10), the heat fluxes induced by specular and diffuse scatterings are given as

$$\begin{aligned} q_{\text{Specular}} =& (T_0 - T^{\text{ref}}) 2\pi \sum_{p} \int_0^{\pi/2} \int_0^{\omega_{\max,\text{p}}} P_i(\omega, \text{p}) \alpha_{\text{Specular},ij}(\theta_i, \omega, \text{p}) C_i(\omega, \text{p}) v_{\text{g},i}(\omega, \text{p}) \cos\theta_i \sin\theta_i d\omega d\theta_i \\ & - (T_0 - T^{\text{ref}}) 2\pi \sum_{p} \int_0^{\pi/2} \int_0^{\omega_{\max,\text{p}}} P_j(\omega, \text{p}) \alpha_{\text{Specular},ji}(\theta_j, \omega, \text{p}) C_j(\omega, \text{p}) v_{\text{g},j}(\omega, \text{p}) \cos\theta_j \sin\theta_j d\omega d\theta_j, \end{aligned} \tag{11}$$

$$\begin{aligned} q_{\text{Diffuse}} =& (T_0 - T^{\text{ref}}) 2\pi \sum_{p} \int_0^{\pi/2} \int_0^{\omega_{\max,\text{p}}} [1 - P_i(\omega, \text{p})] \alpha_{\text{Diffuse},ij}(\omega, \text{p}) C_i(\omega, \text{p}) v_{\text{g},i}(\omega, \text{p}) \cos\theta_i \sin\theta_i d\omega d\theta_i \\ & - (T_0 - T^{\text{ref}}) 2\pi \sum_{p} \int_0^{\pi/2} \int_0^{\omega_{\max,\text{p}}} [1 - P_j(\omega, \text{p})] \alpha_{\text{Diffuse},ji}(\omega, \text{p}) C_j(\omega, \text{p}) v_{\text{g},j}(\omega, \text{p}) \cos\theta_j \sin\theta_j d\omega d\theta_j. \end{aligned} \tag{12}$$

The demonstrations above indicate $q_{\text{Specular}} = 0$ and $q_{\text{Diffuse}} = 0$ when $T_{\text{e},i} = T_{\text{e},j} = T_0$, and thus, the two following relations are obtained as

$$\begin{aligned} & (T_0 - T^{\text{ref}}) 2\pi \sum_{p} \int_0^{\pi/2} \int_0^{\omega_{\max,\text{p}}} P_i(\omega, \text{p}) \alpha_{\text{Specular},ij}(\theta_i, \omega, \text{p}) C_i(\omega, \text{p}) v_{\text{g},i}(\omega, \text{p}) \cos\theta_i \sin\theta_i d\omega d\theta_i \\ & = (T_0 - T^{\text{ref}}) 2\pi \sum_{p} \int_0^{\pi/2} \int_0^{\omega_{\max,\text{p}}} P_j(\omega, \text{p}) \alpha_{\text{Specular},ji}\big(\theta_j, \omega, \text{p}\big) C_j(\omega, \text{p}) v_{\text{g},j}(\omega, \text{p}) \cos\theta_j \sin\theta_j d\omega d\theta_j, \end{aligned} \tag{13}$$

$$\begin{aligned} & (T_0 - T^{\text{ref}}) 2\pi \sum_{p} \int_0^{\pi/2} \int_0^{\omega_{\max,\text{p}}} [1 - P_i(\omega, \text{p})] \alpha_{\text{Diffuse},ij}(\omega, \text{p}) C_i(\omega, \text{p}) v_{\text{g},i}(\omega, \text{p}) \cos\theta_i \sin\theta_i d\omega d\theta_i \\ & = (T_0 - T^{\text{ref}}) 2\pi \sum_{p} \int_0^{\pi/2} \int_0^{\omega_{\max,\text{p}}} [1 - P_j(\omega, \text{p})] \alpha_{\text{Diffuse},ji}(\omega, \text{p}) C_j(\omega, \text{p}) v_{\text{g},j}(\omega, \text{p}) \cos\theta_j \sin\theta_j d\omega d\theta_j. \end{aligned} \tag{14}$$

The left and right terms in Eqs. (13) and (14) represent the heat flux from side i to j and that from side j to i induced by specular and diffuse scattering, respectively. The inelastic scattering and polarization conversion have been demonstrated to play significant roles in interface scattering in some cases but can be neglected in the others [20,21,47–51], so they were either considered or not in the previous interface models [24,25]. To derive an approximate interface model, in this paper, we do not include the impacts from inelastic scattering and polarization conversion for simplicity. Consequently, by ignoring inelastic scattering and polarization conversion and based on the principle of detailed balance, the spectral heat fluxes for each frequency and polarization in both directions in Eqs. (13) and (14) are equal as below:

$$\int_0^1 P_i(\omega,\mathrm{p})\alpha_{\mathrm{Specular},ij}(\mu_i,\omega,\mathrm{p})C_i(\omega,\mathrm{p})v_{\mathrm{g},i}(\omega,\mathrm{p})\mu_i d\mu_i = \int_0^1 P_j(\omega,\mathrm{p})\alpha_{\mathrm{Specular},ji}(\mu_j,\omega,\mathrm{p})C_j(\omega,\mathrm{p})v_{\mathrm{g},j}(\omega,\mathrm{p})\mu_j d\mu_j, \tag{15}$$

$$[1-P_i(\omega,\mathrm{p})]\alpha_{\mathrm{Diffuse},ij}(\omega,\mathrm{p})C_i(\omega,\mathrm{p})v_{\mathrm{g},i}(\omega,\mathrm{p}) = [1-P_j(\omega,\mathrm{p})]\alpha_{\mathrm{Diffuse},ji}(\omega,\mathrm{p})C_j(\omega,\mathrm{p})v_{\mathrm{g},j}(\omega,\mathrm{p}), \tag{16}$$

where $\mu_i = \cos\theta_i$ and $\mu_j = \cos\theta_j$.

Refer to the treatment of AMM for the specular scattering, i.e., treating the phonons as plane waves with the incident and transmitted angles satisfying Snell's law, and Eq. (15) can be revised as

$$P_i(\omega,\mathrm{p})\alpha_{\mathrm{Specular},ij}(\mu_i,\omega,\mathrm{p})C_i(\omega,\mathrm{p})v_{\mathrm{g},i}(\omega,\mathrm{p})\mu_i d\mu_i = P_j(\omega,\mathrm{p})\alpha_{\mathrm{Specular},ji}(\mu_j,\omega,\mathrm{p})C_j(\omega,\mathrm{p})v_{\mathrm{g},j}(\omega,\mathrm{p})\mu_j d\mu_j. \tag{17}$$

Snell's law gives [18]

$$\frac{v_{\mathrm{g},i}(\omega,\mathrm{p})}{\sin\theta_i} = \frac{v_{\mathrm{g},j}(\omega,\mathrm{p})}{\sin\theta_j}. \tag{18}$$

Then Eq. (17) can be rewritten as

$$P_i(\omega,\mathrm{p})\alpha_{\mathrm{Specular},ij}(\mu_i,\omega,\mathrm{p})C_i(\omega,\mathrm{p})v_{\mathrm{g},i}^3(\omega,\mathrm{p}) = P_j(\omega,\mathrm{p})\alpha_{\mathrm{Specular},ji}(\mu_j,\omega,\mathrm{p})C_j(\omega,\mathrm{p})v_{\mathrm{g},j}^3(\omega,\mathrm{p}). \tag{19}$$

With elastic scattering and neglecting polarization conversion, AMM gives the transmissivity as [18]

$$\alpha_{\mathrm{AMM},ij}(\theta_i,\omega,\mathrm{p}) = \alpha_{\mathrm{AMM},ji}(\theta_j,\omega,\mathrm{p}) = \frac{\frac{4\rho_j v_{\mathrm{g},j}(\omega,\mathrm{p})}{\rho_i v_{\mathrm{g},i}(\omega,\mathrm{p})}\frac{\cos\theta_j}{\cos\theta_i}}{\left[\frac{\rho_j v_{\mathrm{g},j}(\omega,\mathrm{p})}{\rho_i v_{\mathrm{g},i}(\omega,\mathrm{p})}+\frac{\cos\theta_j}{\cos\theta_i}\right]^2}, \tag{20}$$

where ρ denotes the mass density. Equation (20) holds when the spectra on both sides are identical, and in this case, the transmissivities for specular interface scattering are maximum [20]. However, if their spectra are different, the transmissivities should be corrected and smaller than those by Eq. (20) [20]. The principle for correcting refers to the maximum transmission model (MTM) [20,52], the generalization for the phonon radiation limit [52], with some modifications here. The MTM assumes that the transmissivity in one direction equals the extreme upper bound, i.e., 1, and that in the reverse direction is obtained based on the total heat flux being 0 at the equilibrium state, which should be <1. The MTM gives the maximum possible transmissivity under the ideal condition. Like the MTM, in this paper, we assume that the transmissivity in one direction equals the extreme upper bound for specular interface scattering, and that in the reverse direction is obtained based on the heat flux induced by specular scattering being 0 at the equilibrium state or Eq. (19), which should be smaller than that by Eq. (20). In detail, when $P_i(\omega,\mathrm{p})C_i(\omega,\mathrm{p})v_{\mathrm{g},i}^3(\omega,\mathrm{p}) \geqslant P_j(\omega,\mathrm{p})C_j(\omega,\mathrm{p})v_{\mathrm{g},j}^3(\omega,\mathrm{p})$, $\alpha_{\mathrm{Specular},ij}(\mu_i,\omega,\mathrm{p}) \leqslant \alpha_{\mathrm{Specular},ji}(\mu_j,\omega,\mathrm{p})$ is valid according to Eq. (19). Thus, the transmissivity from side j to i can reach the extreme upper bound for specular interface scattering and still be given by Eq. (20) as

$$\alpha_{\mathrm{Specular},ji}(\theta_j,\omega,\mathrm{p}) = \frac{\frac{4\rho_j v_{\mathrm{g},j}(\omega,\mathrm{p})}{\rho_i v_{\mathrm{g},i}(\omega,\mathrm{p})}\frac{\cos\theta_j}{\cos\theta_i}}{\left[\frac{\rho_j v_{\mathrm{g},j}(\omega,\mathrm{p})}{\rho_i v_{\mathrm{g},i}(\omega,\mathrm{p})}+\frac{\cos\theta_j}{\cos\theta_i}\right]^2}. \tag{21}$$

Then the transmissivity from side i to j is derived based on Eq. (19) as

$$\alpha_{\mathrm{Specular},ij}(\theta_i,\omega,\mathrm{p}) = \frac{P_j(\omega,\mathrm{p})C_j(\omega,\mathrm{p})v_{\mathrm{g},j}^3(\omega,\mathrm{p})}{P_i(\omega,\mathrm{p})C_i(\omega,\mathrm{p})v_{\mathrm{g},i}^3(\omega,\mathrm{p})}\frac{\frac{4\rho_j v_{\mathrm{g},j}(\omega,\mathrm{p})}{\rho_i v_{\mathrm{g},i}(\omega,\mathrm{p})}\frac{\cos\theta_j}{\cos\theta_i}}{\left[\frac{\rho_j v_{\mathrm{g},j}(\omega,\mathrm{p})}{\rho_i v_{\mathrm{g},i}(\omega,\mathrm{p})}+\frac{\cos\theta_j}{\cos\theta_i}\right]^2}. \tag{22}$$

When $P_i(\omega,\mathrm{p})C_i(\omega,\mathrm{p})v_{\mathrm{g},i}^3(\omega,\mathrm{p}) < P_j(\omega,\mathrm{p})C_j(\omega,\mathrm{p})v_{\mathrm{g},j}^3(\omega,\mathrm{p})$, $\alpha_{\mathrm{Specular},ij}(\mu_i,\omega,\mathrm{p}) > \alpha_{\mathrm{Specular},ji}(\mu_j,\omega,\mathrm{p})$ is valid according to Eq. (19). Thus, the transmissivity from side i to j can reach the extreme upper bound for specular interface scattering and still be given by Eq. (20) as

$$\alpha_{\mathrm{Specular},ij}(\theta_i,\omega,\mathrm{p}) = \frac{\frac{4\rho_j v_{\mathrm{g},j}(\omega,\mathrm{p})}{\rho_i v_{\mathrm{g},i}(\omega,\mathrm{p})}\frac{\cos\theta_j}{\cos\theta_i}}{\left[\frac{\rho_j v_{\mathrm{g},j}(\omega,\mathrm{p})}{\rho_i v_{\mathrm{g},i}(\omega,\mathrm{p})}+\frac{\cos\theta_j}{\cos\theta_i}\right]^2}. \tag{23}$$

Based on Eq. (19), transmissivity from side j to i is derived as

$$\alpha_{\mathrm{Specular},ji}(\theta_j,\omega,\mathrm{p}) = \frac{P_i(\omega,\mathrm{p})C_i(\omega,\mathrm{p})v_{\mathrm{g},i}^3(\omega,\mathrm{p})}{P_j(\omega,\mathrm{p})C_j(\omega,\mathrm{p})v_{\mathrm{g},j}^3(\omega,\mathrm{p})}\frac{\frac{4\rho_j v_{\mathrm{g},j}(\omega,\mathrm{p})}{\rho_i v_{\mathrm{g},i}(\omega,\mathrm{p})}\frac{\cos\theta_j}{\cos\theta_i}}{\left[\frac{\rho_j v_{\mathrm{g},j}(\omega,\mathrm{p})}{\rho_i v_{\mathrm{g},i}(\omega,\mathrm{p})}+\frac{\cos\theta_j}{\cos\theta_i}\right]^2}. \tag{24}$$

The correction above gives the maximum possible transmissivity for specular interface scattering. Through Eqs. (21)–(24), the transmissivities for both cases can be unified as

$$\alpha_{\text{Specular},ij}(\theta_i,\omega,\mathrm{p}) = \min\left\{1, \frac{P_j(\omega,\mathrm{p})C_j(\omega,\mathrm{p})v_{\mathrm{g},j}^3(\omega,\mathrm{p})}{P_i(\omega,\mathrm{p})C_i(\omega,\mathrm{p})v_{\mathrm{g},i}^3(\omega,\mathrm{p})}\right\} \frac{\frac{4\rho_j v_{\mathrm{g},j}(\omega,\mathrm{p})}{\rho_i v_{\mathrm{g},i}(\omega,\mathrm{p})}\frac{\cos\theta_j}{\cos\theta_i}}{\left[\frac{\rho_j v_{\mathrm{g},j}(\omega,\mathrm{p})}{\rho_i v_{\mathrm{g},i}(\omega,\mathrm{p})}+\frac{\cos\theta_j}{\cos\theta_i}\right]^2}, \tag{25}$$

$$\alpha_{\text{Specular},ji}(\theta_j,\omega,\mathrm{p}) = \min\left\{1, \frac{P_i(\omega,\mathrm{p})C_i(\omega,\mathrm{p})v_{\mathrm{g},i}^3(\omega,\mathrm{p})}{P_j(\omega,\mathrm{p})C_j(\omega,\mathrm{p})v_{\mathrm{g},j}^3(\omega,\mathrm{p})}\right\} \frac{\frac{4\rho_j v_{\mathrm{g},j}(\omega,\mathrm{p})}{\rho_i v_{\mathrm{g},i}(\omega,\mathrm{p})}\frac{\cos\theta_j}{\cos\theta_i}}{\left[\frac{\rho_j v_{\mathrm{g},j}(\omega,\mathrm{p})}{\rho_i v_{\mathrm{g},i}(\omega,\mathrm{p})}+\frac{\cos\theta_j}{\cos\theta_i}\right]^2}. \tag{26}$$

For the diffusely scattered phonons, the following relations hold [19,24]:

$$\alpha_{\text{Diffuse},ji}(\omega,\mathrm{p}) = r_{\text{Diffuse},ii}(\omega,\mathrm{p}) = 1-\alpha_{\text{Diffuse},ij}(\omega,\mathrm{p}), \tag{27}$$

where r denotes the reflectivity. Equation (27) indicates that the probability of a phonon transmitting across the interface from side j to i equals that being reflected back from side i to i. Based on Eqs. (16) and (27), the following equations are obtained:

$$\alpha_{\text{Diffuse},ij}(\omega,\mathrm{p}) = \frac{[1-P_j(\omega,\mathrm{p})]C_j(\omega,\mathrm{p})v_{\mathrm{g},j}(\omega,\mathrm{p})}{[1-P_i(\omega,\mathrm{p})]C_i(\omega,\mathrm{p})v_{\mathrm{g},i}(\omega,\mathrm{p})+[1-P_j(\omega,\mathrm{p})]C_j(\omega,\mathrm{p})v_{\mathrm{g},j}(\omega,\mathrm{p})}, \tag{28}$$

$$\alpha_{\text{Diffuse},ji}(\omega,\mathrm{p}) = \frac{[1-P_i(\omega,\mathrm{p})]C_i(\omega,\mathrm{p})v_{\mathrm{g},i}(\omega,\mathrm{p})}{[1-P_i(\omega,\mathrm{p})]C_i(\omega,\mathrm{p})v_{\mathrm{g},i}(\omega,\mathrm{p})+[1-P_j(\omega,\mathrm{p})]C_j(\omega,\mathrm{p})v_{\mathrm{g},j}(\omega,\mathrm{p})}. \tag{29}$$

Considering $C=\hbar\omega\frac{\mathrm{d}f}{\mathrm{d}T}D=\hbar\omega\frac{\mathrm{d}f}{\mathrm{d}T}\frac{k^2}{2\pi^2 v_{\mathrm{g}}}$ with wave number k, Eqs. (28) and (29) can be rewritten as

$$\alpha_{\text{Diffuse},ij}(\omega,\mathrm{p}) = \frac{[1-P_j(\omega,\mathrm{p})]k_j^2(\omega,\mathrm{p})}{[1-P_i(\omega,\mathrm{p})]k_i^2(\omega,\mathrm{p})+[1-P_j(\omega,\mathrm{p})]k_j^2(\omega,\mathrm{p})}, \tag{30}$$

$$\alpha_{\text{Diffuse},ji}(\omega,\mathrm{p}) = \frac{[1-P_i(\omega,\mathrm{p})]k_i^2(\omega,\mathrm{p})}{[1-P_i(\omega,\mathrm{p})]k_i^2(\omega,\mathrm{p})+[1-P_j(\omega,\mathrm{p})]k_j^2(\omega,\mathrm{p})}. \tag{31}$$

Equations (30) and (31) will degenerate into one SDMM with the identical specularities on both sides [12,24]. Furthermore, the following specularity dependent on phonon wavelength is considered in this paper [53]:

$$P(\omega,\mathrm{p}) = \exp\left[-\frac{16\pi^2\eta^2}{\lambda^2(\omega,\mathrm{p})}\right], \tag{32}$$

where λ denotes phonon wavelength, obtained from $\lambda(\omega,\mathrm{p})=\frac{2\pi}{k(\omega,\mathrm{p})}$; and η is the interface roughness, also called the root mean square roughness of the interface.

Based on Eqs. (1), (2), (25), (26), and (30)–(32), the present SMMM accounting for spectral specularity and spectral specular and spectral diffuse scatterings is derived as

$$\begin{aligned}\alpha_{ij}(\theta_i,\omega,\mathrm{p}) &= P_i(\omega,\mathrm{p})\alpha_{\text{Specular},ij}(\theta_i,\omega,\mathrm{p})+[1-P_i(\omega,\mathrm{p})]\alpha_{\text{Diffuse},ij}(\omega,\mathrm{p})\\ &= \exp\left[-\frac{16\pi^2\eta^2}{\lambda_i^2(\omega,\mathrm{p})}\right]\min\left\{1,\frac{P_j(\omega,\mathrm{p})C_j(\omega,\mathrm{p})v_{\mathrm{g},j}^3(\omega,\mathrm{p})}{P_i(\omega,\mathrm{p})C_i(\omega,\mathrm{p})v_{\mathrm{g},i}^3(\omega,\mathrm{p})}\right\}\frac{\frac{4\rho_j v_{\mathrm{g},j}(\omega,\mathrm{p})}{\rho_i v_{\mathrm{g},i}(\omega,\mathrm{p})}\frac{\cos\theta_j}{\cos\theta_i}}{\left[\frac{\rho_j v_{\mathrm{g},j}(\omega,\mathrm{p})}{\rho_i v_{\mathrm{g},i}(\omega,\mathrm{p})}+\frac{\cos\theta_j}{\cos\theta_i}\right]^2}\\ &\quad+\left\{1-\exp\left[-\frac{16\pi^2\eta^2}{\lambda_i^2(\omega,\mathrm{p})}\right]\right\}\frac{[1-P_j(\omega,\mathrm{p})]k_j^2(\omega,\mathrm{p})}{[1-P_i(\omega,\mathrm{p})]k_i^2(\omega,\mathrm{p})+[1-P_j(\omega,\mathrm{p})]k_j^2(\omega,\mathrm{p})},\end{aligned} \tag{33}$$

$$\begin{aligned}\alpha_{ji}(\theta_j,\omega,\mathrm{p}) &= P_j(\omega,\mathrm{p})\alpha_{\text{Specular},ji}(\theta_j,\omega,\mathrm{p})+[1-P_j(\omega,\mathrm{p})]\alpha_{\text{Diffuse},ji}(\omega,\mathrm{p})\\ &= \exp\left[-\frac{16\pi^2\eta^2}{\lambda_j^2(\omega,\mathrm{p})}\right]\min\left\{1,\frac{P_i(\omega,\mathrm{p})C_i(\omega,\mathrm{p})v_{\mathrm{g},i}^3(\omega,\mathrm{p})}{P_j(\omega,\mathrm{p})C_j(\omega,\mathrm{p})v_{\mathrm{g},j}^3(\omega,\mathrm{p})}\right\}\frac{\frac{4\rho_j v_{\mathrm{g},j}(\omega,\mathrm{p})}{\rho_i v_{\mathrm{g},i}(\omega,\mathrm{p})}\frac{\cos\theta_j}{\cos\theta_i}}{\left[\frac{\rho_j v_{\mathrm{g},j}(\omega,\mathrm{p})}{\rho_i v_{\mathrm{g},i}(\omega,\mathrm{p})}+\frac{\cos\theta_j}{\cos\theta_i}\right]^2}\\ &\quad+\left\{1-\exp\left[-\frac{16\pi^2\eta^2}{\lambda_j^2(\omega,\mathrm{p})}\right]\right\}\frac{[1-P_i(\omega,\mathrm{p})]k_i^2(\omega,\mathrm{p})}{[1-P_i(\omega,\mathrm{p})]k_i^2(\omega,\mathrm{p})+[1-P_j(\omega,\mathrm{p})]k_j^2(\omega,\mathrm{p})},\end{aligned} \tag{34}$$

where $P_i(\omega, \mathrm{p}) = \exp[-\frac{16\pi^2\eta^2}{\lambda_i^2(\omega,\mathrm{p})}]$ and $P_j(\omega, \mathrm{p}) = \exp[-\frac{16\pi^2\eta^2}{\lambda_j^2(\omega,\mathrm{p})}]$. The present SMMM indicates that the transmissivity depends not only on the phonon spectra and incident angle but also on the specularity; that is, changes in specularity may lead to changes in transmissivity. This model will degenerate into the classical MMM for gray media with identical specularities on both sides [20]. Compared with the recent interface models [27,28], the present SMMM can not only capture the spectrum dependence of specularity and specular and diffuse scatterings but also satisfy the principle of detailed balance.

B. Interface treatment in Monte Carlo framework

Secondly, the Monte Carlo framework for spectral specularity and spectral specular and spectral diffuse scatterings at heterogeneous interfaces is developed based on the above SMMM. Through a random sampling technique, the Monte Carlo method for phonon transport can give the macroscopic information, analogous to its counterpart, the direct simulation Monte Carlo method for rarefied gas flow and photon transport [54,55]. In this paper, we adopt the steady-state version of the kinetic Monte Carlo method, based on the linearized version of deviational formulation of the energy-based phonon Boltzmann transport equation [56,57]. The deviational formulation of the energy-based phonon Boltzmann transport equation is given as below [56]:

$$\frac{\partial e^{\mathrm{d}}}{\partial t} + \mathbf{v}_{\mathrm{g}}(\omega, \mathrm{p}) \cdot \nabla e^{\mathrm{d}} = \frac{(e^{\mathrm{pse}} - e^{\mathrm{ref}}) - e^{\mathrm{d}}}{\tau(\omega, \mathrm{p}, T)}, \tag{35}$$

where $e^{\mathrm{d}} = e - e^{\mathrm{ref}}$ denotes the deviational energy with the energy distribution $e = \hbar\omega f$ with the phonon distribution f, and the referenced equilibrium energy distribution $e^{\mathrm{ref}} = \hbar\omega f^{\mathrm{ref}}$ with the Bose-Einstein distribution $f^{\mathrm{ref}} = 1/[\exp(\frac{\hbar\omega}{k_{\mathrm{B}}T^{\mathrm{ref}}}) - 1]$ at the referenced equilibrium temperature T^{ref}; $e^{\mathrm{pse}} = \hbar\omega f^{\mathrm{pse}}$ is the pseudoequilibrium energy distribution with the Bose-Einstein distribution $f^{\mathrm{pse}} = 1/[\exp(\frac{\hbar\omega}{k_{\mathrm{B}}T^{\mathrm{pse}}}) - 1]$ at pseudoequilibrium temperature T^{pse}; $\mathbf{v}_{\mathrm{g}}$ and τ are the vector of group velocity and the relaxation time, respectively; and T represents the equilibrium temperature. The steady-state formulation of Eq. (35) is considered for the present Monte Carlo method as [56,57]

$$\mathbf{v}_{\mathrm{g}}(\omega, \mathrm{p}) \cdot \nabla e^{\mathrm{d}} = \frac{(e^{\mathrm{pse}} - e^{\mathrm{ref}}) - e^{\mathrm{d}}}{\tau(\omega, \mathrm{p}, T)}. \tag{36}$$

The steady-state version of the kinetic-type Monte Carlo method adopted in the present simulation is obtained by further linearizing Eq. (36) at small temperature difference [56,57].

The steady-state version of the kinetic-type Monte Carlo method directly obtains the macroscopic information at steady state, including the temperature distribution and heat flux, by tracking random walks of several energy packets one by one, more efficiently than its transient counterpart. It totally contains five steps to run the simulation for each energy packet, i.e., initialization, advection, scattering, sampling, and boundary condition, with the detailed algorithm in Ref. [57]. Interface scattering will be implemented in the scattering step when an energy packet interacts with the interface. The present interface treatment in the Monte Carlo framework is like Ref. [45] for gray media, but here, we consider a more general case with spectral specularity and spectral specular and spectral diffuse scatterings at heterogeneous interfaces. Without loss of generality, the energy packet incident on the interface on side i is considered. The detailed Monte Carlo framework for interface treatment in this paper is as follows:

(a) Calculate the distances of the energy packet from its present position to the locations of the interface, boundary, and intrinsic scatterings, respectively. The distances for the interface and boundary scatterings can be determined from its trajectory. The distance for the intrinsic scattering can be derived from the phonon relaxation time expression. If the distance for the interface scattering is the shortest, the energy packet will be scattered by the interface first.

(b) For the energy packet scattered by the interface first, a random number R_1 between 0 and 1 is generated and compared with the specularity $P_i(\omega, \mathrm{p})$. If $R_1 \leqslant P_i(\omega, \mathrm{p})$, this energy packet will be specularly scattered. On the contrary, it will be diffusely scattered. Since the spectral specularity and the heterogeneous interface are considered, the specularity may be different for energy packets with different frequencies or polarizations and on both sides of the interface.

(c) When the energy packet is specularly scattered, another random number R_2 between 0 and 1 is generated and compared with the spectral transmissivity for specular scattering $\alpha_{\mathrm{Specular},ij}$. If $R_2 \leqslant \alpha_{\mathrm{Specular},ij}$, this energy packet will transmit across the interface. For the transmitted energy packet, conserve its frequency and polarization but update the group velocity and relaxation time based on the phonon spectra on the new side, and its advection direction will be also updated based on Snell's law, i.e., Eq. (18). On the contrary, this energy packet will be reflected. The reflection angle is given by $(\pi - \theta_i)$ with the incident angle θ_i. All other properties are conserved for the reflected energy packets. Since the heterogeneous interface is considered, the properties of the incident and transmitted energy packets are different.

(d) When the energy packet is diffusely scattered, another random number R_3 between 0 and 1 is generated and compared with the spectral transmissivity for diffuse scattering $\alpha_{\mathrm{Diffuse},ij}$. If $R_3 \leqslant \alpha_{\mathrm{Diffuse},ij}$, the energy packet will transmit across the interface. Its frequency and polarization are conserved, but group velocity and relaxation time are updated according to the phonon spectra on the new side. Additionally, its advection direction is updated based on Lambert's cosine law [58]. On the contrary, the energy packet will be reflected to the original side with the updated advection direction based on Lambert's cosine law [58]. Except for the advection direction, all other properties of the reflected energy packet are conserved. The implementation of Lambert's cosine law in the Monte Carlo method is as follow [58]. Generating two random numbers between 0 and 1 as R_4 and R_5, the velocity components of the transmitted energy packet in each direction are calculated by

$$\begin{aligned} v_1 &= v_{\mathrm{g},j}\cos\theta = v_{\mathrm{g},j}\sqrt{R_4}, \\ v_2 &= v_{\mathrm{g},j}\sin\theta\cos\phi = v_{\mathrm{g},j}\sqrt{1-R_4}\cos(2\pi R_5), \\ v_3 &= v_{\mathrm{g},j}\sin\theta\sin\phi = v_{\mathrm{g},j}\sqrt{1-R_4}\sin(2\pi R_5), \end{aligned} \tag{37}$$

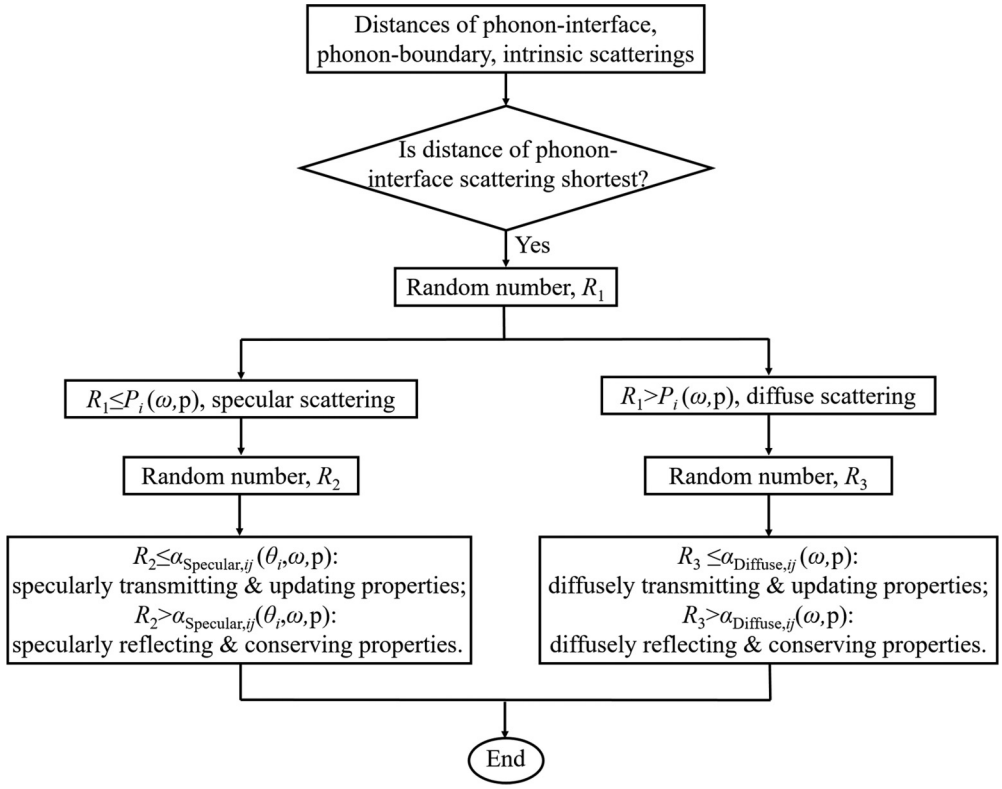

FIG. 1. The flow chart of interface treatment in Monte Carlo framework for spectral specularity and spectral specular and spectral diffuse scatterings.

and those of the reflected energy packet are calculated by

$$\begin{aligned} v_1 &= v_{\mathrm{g},i}\cos(\pi-\theta) = -v_{\mathrm{g},i}\cos\theta = -v_{\mathrm{g},i}\sqrt{R_4}, \\ v_2 &= v_{\mathrm{g},i}\sin(\pi-\theta)\cos\phi \\ &= v_{\mathrm{g},i}\sin\theta\cos\phi \\ &= v_{\mathrm{g},i}\sqrt{1-R_4}\cos(2\pi R_5), \\ v_3 &= v_{\mathrm{g},i}\sin(\pi-\theta)\sin\phi \\ &= v_{\mathrm{g},i}\sin\theta\sin\phi \\ &= v_{\mathrm{g},i}\sqrt{1-R_4}\sin(2\pi R_5), \end{aligned} \tag{38}$$

where v_1 denotes the velocity component perpendicular to the interface, and v_2 and v_3 denote the velocity components parallel to the interface; and θ and ϕ are the polar and azimuthal angles, respectively.

Finally, the algorithm above is summarized in Fig. 1.

For partially specular and partially diffuse scattering, there are generally two approaches to treat the interface scattering in Monte Carlo simulation. The first one is to generate one random number to first determine whether the phonon transmits or is reflected and then generate another random number to determine whether the scattering is specular or diffuse, as Ref. [44] does at the homogenous interface. The second one is to generate one random number to first determine whether the scattering is diffuse or specular and then generate another random number to determine whether the phonon transmits or is reflected, as Ref. [45] does in gray media. Here, we will demonstrate both approaches are correct and consistent with each other. For simplicity, only the case of the phonons incident on the interface from side i to j is considered, with frequency ω, polarization p, and incident angle θ_i. The demonstrations for other cases are similar. Based on Eq. (1), the proportions for specularly transmitted, specularly reflected, diffusely transmitted, and diffusely reflected phonons among all phonons scattered by the interface are $P_i(\omega,\mathrm{p})\alpha_{\mathrm{Specular},ij}(\theta_i,\omega,\mathrm{p})$, $P_i(\omega,\mathrm{p})[1-\alpha_{\mathrm{Specular},ij}(\theta_i,\omega,\mathrm{p})]$, $[1-P_i(\omega,\mathrm{p})]\alpha_{\mathrm{Diffuse},ij}(\omega,\mathrm{p})$, and $[1-P_i(\omega,\mathrm{p})][1-\alpha_{\mathrm{Diffuse},ij}(\omega,\mathrm{p})]$, respectively. The condition to justify the correctness of the Monte Carlo framework for interface treatment is its ability to accurately calculate these proportions.

If following the first approach, one random number is generated and compared with the transmissivity $\alpha_{ij}(\theta_i,\omega,\mathrm{p})$ to first determine whether the phonons transmit. It means that the proportions for transmitted and reflected phonons among all phonons scattered by the interface are $\alpha_{ij}(\theta_i,\omega,\mathrm{p})$ and $1-\alpha_{ij}(\theta_i,\omega,\mathrm{p})$. Then another random number is generated to determine whether the scattering is specular or diffuse. From Eq. (1), the proportions of specularly and diffusely transmitted phonons among transmitted phonons are

$$\frac{P_i(\omega,\mathrm{p})\alpha_{\mathrm{Specular},ij}(\theta_i,\omega,\mathrm{p})}{\alpha_{ij}(\theta_i,\omega,\mathrm{p})}$$

and

$$\frac{[1-P_i(\omega,\mathrm{p})]\alpha_{\mathrm{Diffuse},ij}(\omega,\mathrm{p})}{\alpha_{ij}(\theta_i,\omega,\mathrm{p})},$$

i.e.,

$$\frac{P_i(\omega, \mathrm{p})\alpha_{\mathrm{Specular},ij}(\theta_i, \omega, \mathrm{p})}{P_i(\omega, \mathrm{p})\alpha_{\mathrm{Specular},ij}(\theta_i, \omega, \mathrm{p}) + [1 - P_i(\omega, \mathrm{p})]\alpha_{\mathrm{Diffuse},ij}(\omega, \mathrm{p})}$$

and

$$\frac{[1 - P_i(\omega, \mathrm{p})]\alpha_{\mathrm{Diffuse},ij}(\omega, \mathrm{p})}{P_i(\omega, \mathrm{p})\alpha_{\mathrm{Specular},ij}(\theta_i, \omega, \mathrm{p}) + [1 - P_i(\omega, \mathrm{p})]\alpha_{\mathrm{Diffuse},ij}(\omega, \mathrm{p})}.$$

When $\alpha_{\mathrm{Specular},ij}(\theta_i, \omega, \mathrm{p}) = \alpha_{\mathrm{Diffuse},ij}(\omega, \mathrm{p})$, these two proportions equal $P_i(\omega, \mathrm{p})$ and $1 - P_i(\omega, \mathrm{p})$, as the case in Ref. [44]. Thus, the proportions of specularly and diffusely transmitted phonons among all phonons scattered by the interface are $P_i(\omega, \mathrm{p})\alpha_{\mathrm{Specular},ij}(\theta_i, \omega, \mathrm{p})$ and $[1 - P_i(\omega, \mathrm{p})]\alpha_{\mathrm{Diffuse},ij}(\omega, \mathrm{p})$. Similarly, the proportions of specularly and diffusely reflected phonons among all phonons scattered by the interface are $P_i(\omega, \mathrm{p})[1 - \alpha_{\mathrm{Specular},ij}(\theta_i, \omega, \mathrm{p})]$ and $[1 - P_i(\omega, \mathrm{p})][1 - \alpha_{\mathrm{Diffuse},ij}(\omega, \mathrm{p})]$. Hence, the first approach can reproduce these proportions and satisfies the condition. If following the second approach, one random number is generated and compared with the specularity $P_i(\omega, \mathrm{p})$ to first determine whether the scattering is specular or diffuse. It means that the proportions for specularly and diffusely scattered phonons among all phonons scattered by the interface are $P_i(\omega, \mathrm{p})$ and $1 - P_i(\omega, \mathrm{p})$, respectively. Then another random number is generated to determine whether phonons transmit or are reflected. For specular scattering, this random number is compared with the transmissivity for specular scattering $\alpha_{\mathrm{Specular},ij}(\theta_i, \omega, \mathrm{p})$. It means that the proportions of specularly transmitted and reflected phonons among specularly scattered phonons are $\alpha_{\mathrm{Specular},ij}(\theta_i, \omega, \mathrm{p})$ and $1 - \alpha_{\mathrm{Specular},ij}(\theta_i, \omega, \mathrm{p})$. Thus, the proportions of specularly transmitted and reflected phonons among all phonons scattered by the interface are $P_i(\omega, \mathrm{p})\alpha_{\mathrm{Specular},ij}(\theta_i, \omega, \mathrm{p})$ and $P_i(\omega, \mathrm{p})[1 - \alpha_{\mathrm{Specular},ij}(\theta_i, \omega, \mathrm{p})]$. For diffuse scattering, this random number is compared with the transmissivity for diffuse scattering $\alpha_{\mathrm{Diffuse},ij}(\omega, \mathrm{p})$. It indicates that the proportions of diffusely transmitted and reflected phonons among diffusely scattered phonons are $\alpha_{\mathrm{Diffuse},ij}(\omega, \mathrm{p})$ and $1 - \alpha_{\mathrm{Diffuse},ij}(\omega, \mathrm{p})$. Thus, the proportions of diffusely transmitted and reflected phonons among all phonons scattered by the interface are $[1 - P_i(\omega, \mathrm{p})]\alpha_{\mathrm{Diffuse},ij}(\omega, \mathrm{p})$ and $[1 - P_i(\omega, \mathrm{p})][1 - \alpha_{\mathrm{Diffuse},ij}(\omega, \mathrm{p})]$. Therefore, the second approach can also accurately reproduce the above proportions and thus satisfies the condition, consistent with the first approach. In the present Monte Carlo framework, the interface treatment follows the second approach.

III. VALIDATIONS

In the present section, the SMMM and the Monte Carlo method are validated in cross-plane phonon transport across monolayer films and cross-plane interfacial phonon transport across bilayer films by comparisons with the discrete-ordinates method and experiments.

A. Cross-plane phonon transport

First, in cross-plane phonon transport across monolayer films, the present Monte Carlo method is verified for films without interfaces by comparisons with the discrete-ordinates method. These monolayer films are composed of Al, Si, and Ge, shown in Fig. 2(a). The numerical implementations for the discrete-ordinates method are well developed and referred to in Refs. [37,40,59], solving difference equations of the phonon Boltzmann transport equation discretized by the finite difference method at each discrete angle with the isothermal boundary conditions. The isotropic [100] dispersions of Al are adopted from Ref. [60], and those for Si and Ge are taken from Ref. [61,62], with the contributions from both acoustic and optical polarizations, and their phonon relaxation times are referred to in Ref. [63]. The temperature distributions and heat fluxes along films at steady state are first obtained by the Monte Carlo method and the discrete-ordinates method. Then the thermal conductivities are calculated based on Fourier's law with the temperature distributions and heat fluxes, using the formula $\kappa = q/[L(T_\mathrm{L} - T_\mathrm{R})]$, where q denotes the average heat flux along the film, L being the thickness of the film, and T_L and T_R representing the boundary temperatures on the left and right sides. The numbers of energy packets are simply selected as 150 million, and the boundary temperatures on the left and right sides are fixed at 303 and 297 K, respectively. Concerning too-high computational cost for large thicknesses in both the Monte Carlo method and the discrete-ordinates method, the maximum thicknesses for three materials are selected as 500 nm. Figure 3 gives the temperature distributions and the thermal conductivities at various thicknesses of films by these two methods, showing good agreement. Although thermal conductivities in Fig. 3(d) are not converged due to the nonnegligible boundary scattering effect, the correctness of the present Monte Carlo method is still verified when two methods agree with each other. It means that the present Monte Carlo method can accurately simulate phonon transport through monolayer films, and the boundary temperature jumps increase as the thickness decreases, resulting from stronger nonequilibrium effects by increasingly frequent boundary scattering. Additionally, the thermal conductivity decreases with decreasing the thickness, indicating the increasing thermal resistances at boundaries, also a result of increasingly frequent boundary scattering.

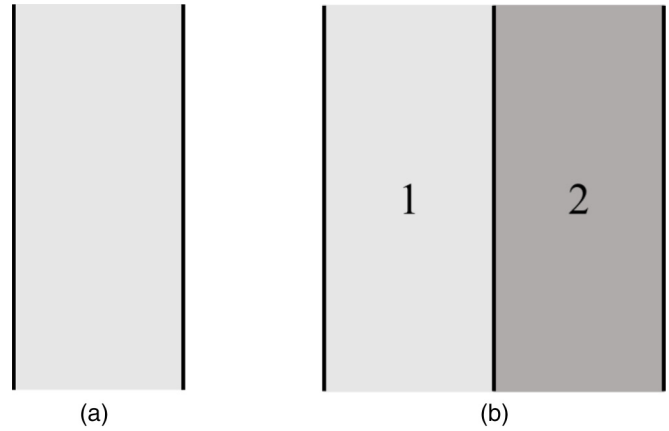

FIG. 2. Monolayer film for cross-plane phonon transport and bilayer film for cross-plane interfacial phonon transport: (a) monolayer film and (b) bilayer film. 1 and 2 label two materials.

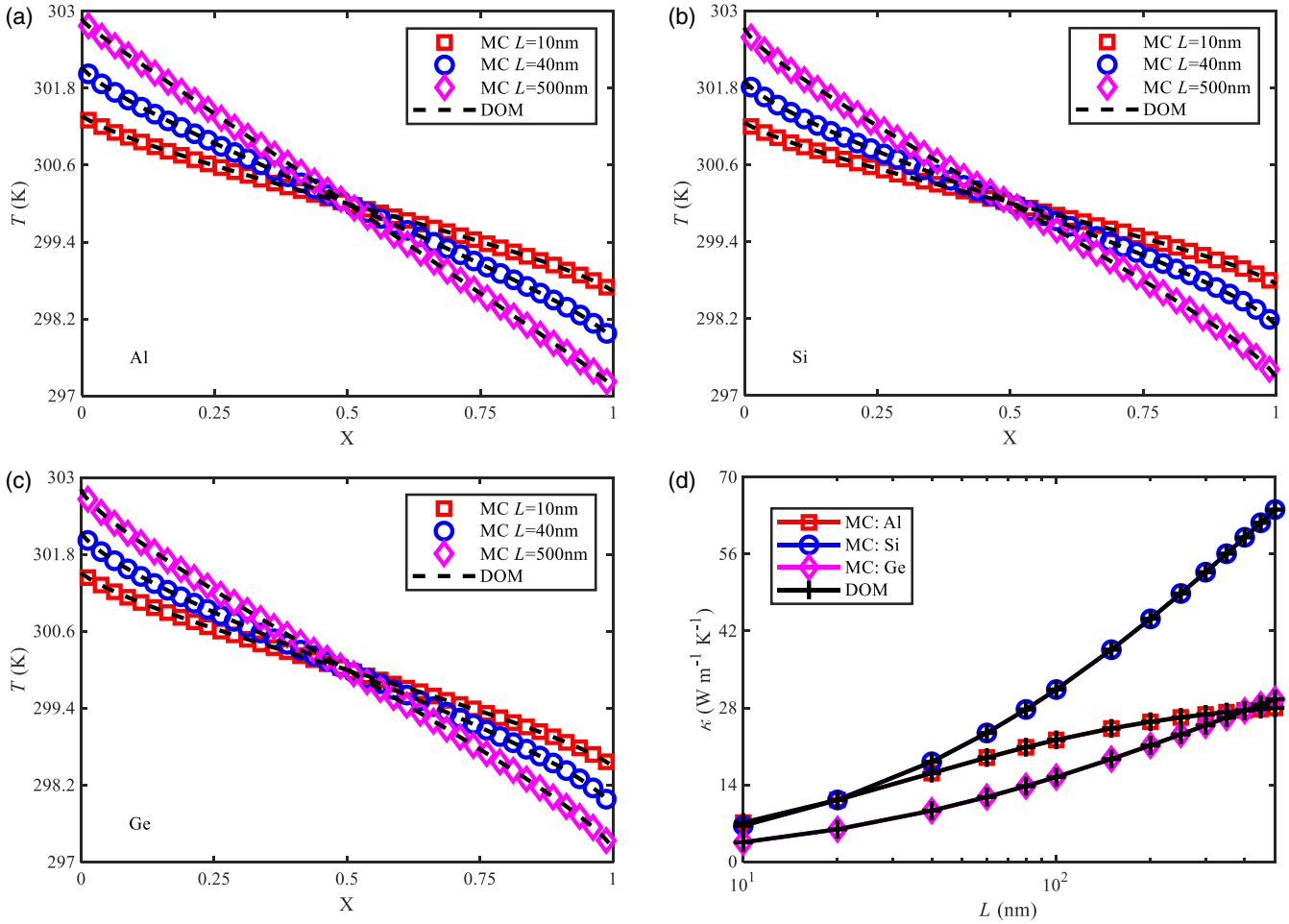

FIG. 3. The temperature distribution and thermal conductivity at various thicknesses of monolayer films: (a) temperature distribution of Al film; (b) temperature distribution of Si film; (c) temperature distribution of Ge film; and (d) thermal conductivities of Al, Si, and Ge films.

B. Cross-plane interfacial phonon transport

Secondly, in cross-plane interfacial phonon transport across bilayer films with planar interfaces, the present SMMM and Monte Carlo framework for the interface scattering are validated by comparisons with the discrete-ordinates method and experiments. The implementations of the discrete-ordinates method inside each layer are the same as those for cross-plane phonon transport in the previous part, and the interface treatment is adopted to bridge two layers. The present interface treatment in the discrete-ordinates method is like that for completely spectral diffuse scattering in Refs. [12,40], with some improvements to account for spectral specularity and spectral specular and spectral diffuse scatterings. The detailed implementations and verifications of the discrete-ordinates method for the interface scattering will be provided in future work. The physical model for validations is shown in Fig. 2(b) with two material pairs, Al(1)/Si(2) and Ge(1)/Si(2). The dispersions and relaxation times of three materials are also referred to in Refs. [60–63], respectively, as the previous part does. The temperature distributions and heat fluxes along films at steady state are first obtained by the Monte Carlo method and the discrete-ordinates method. Then thermal boundary conductances are calculated based on the steady-state temperature distributions and heat fluxes using formula $G = q/\Delta T$, with the heat flux across the interface q and the temperature jump at the interface ΔT. For simplicity, the interface roughnesses, the numbers of energy packets, and the material volume ratios in all cases are uniformly set to 0.15 nm, 200 million, and 1, respectively. The boundary temperatures on the left and right sides are fixed at 303 and 297 K. The spatial steps of both the Monte Carlo method and the discrete-ordinates method are fixed at one identical value for the convenience of comparison. To calculate thermal boundary conductance conveniently, the spatial step is set to a very small value as 0.01 nm for all cases in both methods, with the detailed reason explained later. Since the computational cost is not sensitive to the spatial step in the present steady-state version of the kinetic Monte Carlo method, this setting will not cause the additional computational cost for the Monte Carlo method. For the discrete-ordinates method, this setting will increase the storage consumption but reduce convergence steps so have little effect on the computational cost. Finally, concerning the computational cost as the previous part does, the maximum total thicknesses for both material pairs are selected as 500 nm.

To show the temperature distribution more clearly, the temperatures of part of the cells are selected and plotted in

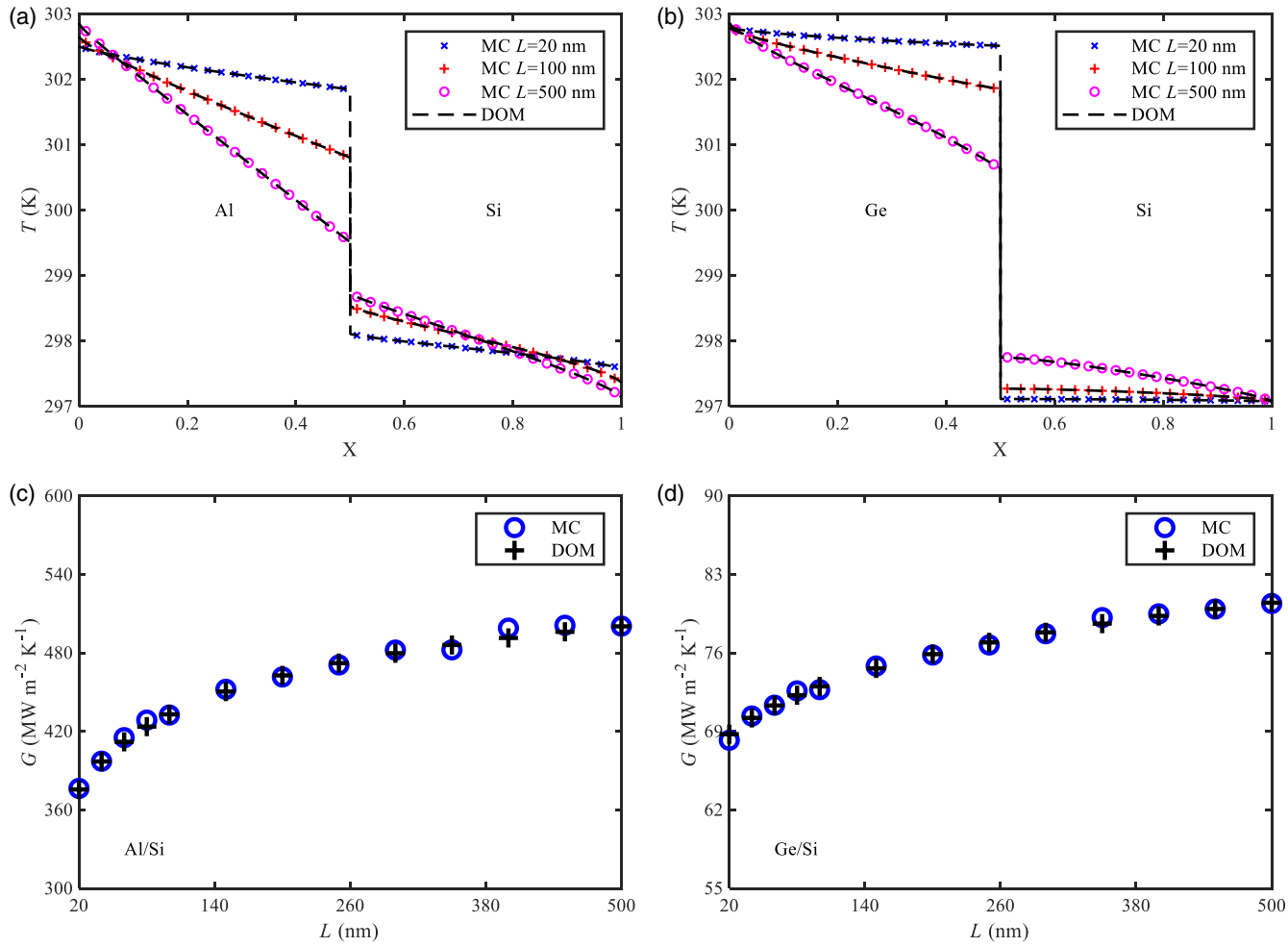

FIG. 4. The temperature distribution and thermal boundary conductance at various thicknesses of bilayer films: (a) temperature distribution of Al/Si film, (b) temperature distribution of Ge/Si film, (c) thermal boundary conductance of Al/Si film, and (d) thermal boundary conductance of Ge/Si film.

Figs. 4(a) and 4(b) at various thicknesses of films, showing good agreement. To calculate the thermal boundary conductance, it is crucial to obtain the accurate temperature jump which is nonlinear due to the nonequilibrium phonons at the interface [64,65]. Due to the strongly nonequilibrium effect near the interface, the equivalent equilibrium temperature is adopted to define the temperature at the interface with detailed explanations at the end of this part. This temperature is calculated by statistically summing the energy density within the cells in the simulation. As the spatial step becomes smaller, the cell is smaller, and the temperature of the cell closest to the interface becomes closer to the temperature at the interface. Due to the very small spatial step in this paper, it is inferred that the temperature jump at the interface can be regarded as the temperature difference between two cells closest to the interface on both sides and thus can be directly obtained from their equivalent equilibrium temperatures. To verify this inference, the temperature distributions of all cells for Al/Si and Ge/Si at thicknesses being 20 and 500 nm are given in Figs. 5 and 6. For the thickness being 20 nm, the temperatures of five cells from the interface to the inner volume on the Al side by the Monte Carlo method are 301.8384, 301.8439, 301.8432, 301.8370, and 301.8480 K, and the irregular variations are caused by the noise error. The variations of the temperatures of these five cells are much smaller than the overall temperature difference along the present layer as 0.6573 K, and the temperature difference between two cells closest to the interface on both sides is 3.7305 K. For the thickness being 500 nm, these temperatures on the Al side by the Monte Carlo method are 299.5178, 299.5159, 299.5105, 299.5144, and 299.5048 K, where the irregular variations are also the result of the noise error. Their variations are also much smaller than the overall temperature difference within this present layer as 3.3454 K, and the temperature difference between two cells closest to the interface on both sides is 0.7838 K. The above conclusions hold true for the Si side and Ge/Si.

It should be noted that the above inference has also been verified for the various thicknesses at the interface roughness being 0.15 nm, and the thickness being 20 and 500 nm at the interface roughness varied from 0.02 to 0.2 nm with a common difference 0.02 nm, and from 0.2 to 1.8 nm with a common difference 0.2 nm, which interface roughness will be considered in the following parts. It means that, due to the very small spatial step, the temperatures of two cells closest

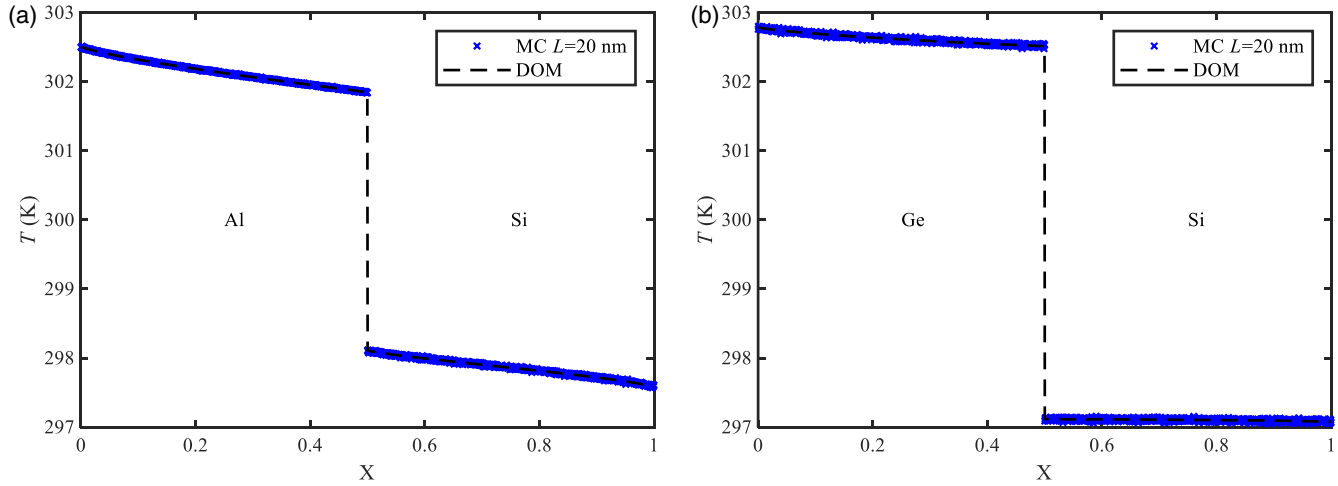

FIG. 5. The temperature distribution of all cells in the bilayer films at the total thickness as 20 nm: (a) Al/Si and (b) Ge/Si.

to the interface on both sides can be regarded as those at the interface, and their temperature difference roughly equals the temperature jump at the interface. Therefore, calculating the temperature difference between two cells closest to the interface on both sides is an effective way to determine the temperature jump at the interface. Knowing the temperature jumps, the thermal boundary conductances are calculated and given in Figs. 4(c) and 4(d). The small deviations for thermal boundary conductances result from the noise error of the Monte Carlo method. Thus, the present Monte Carlo method is verified in interfacial phonon transport, although thermal boundary conductances are not converged. For the temperature distributions, the temperature jump at the interface increases with decreasing the film thickness because of stronger nonequilibrium effects by increasingly frequent interface scattering. Additionally, the thermal boundary conductance decreases or thermal boundary resistance increases with decreasing film thickness, also a result of increasingly frequent interface scattering.

To further validate the present SMMM and the Monte Carlo framework, thermal boundary conductances between Al/Si by simulations and experiments are compared in the bilayer film, shown in Fig. 2(b). The thickness of Al is set to 100 nm to reproduce the situation in experiments [66], and that of Si is set to 1000 nm to ensure that it is sufficiently larger than its phonon mean free path and simultaneously avoid the excessive computational cost. Due to the lack of characterization of the interface in the experiment, it is difficult to determine the interface roughness for this comparison, but as mentioned in Ref. [66], the thermal boundary conductance between Al/Si was measured after removing the natural oxide at the interface, at which the interface can be regarded as the highest-quality one. Then referring to the measured interface roughness by transmission electron microscopy in Ref. [22], in this paper, we just select four small interface roughnesses as 0, 0.02, 0.04, and 0.06 nm, and a larger one as 0.3 nm, to simulate phonon transport. The numbers of energy packets for all simulations are fixed at 250 million. The boundary temperatures on the left and right sides are fixed at 303 and 297 K to obtain thermal boundary conductance under 300 K. For comparisons, the results by the Monte Carlo method based on SDMM are also given since

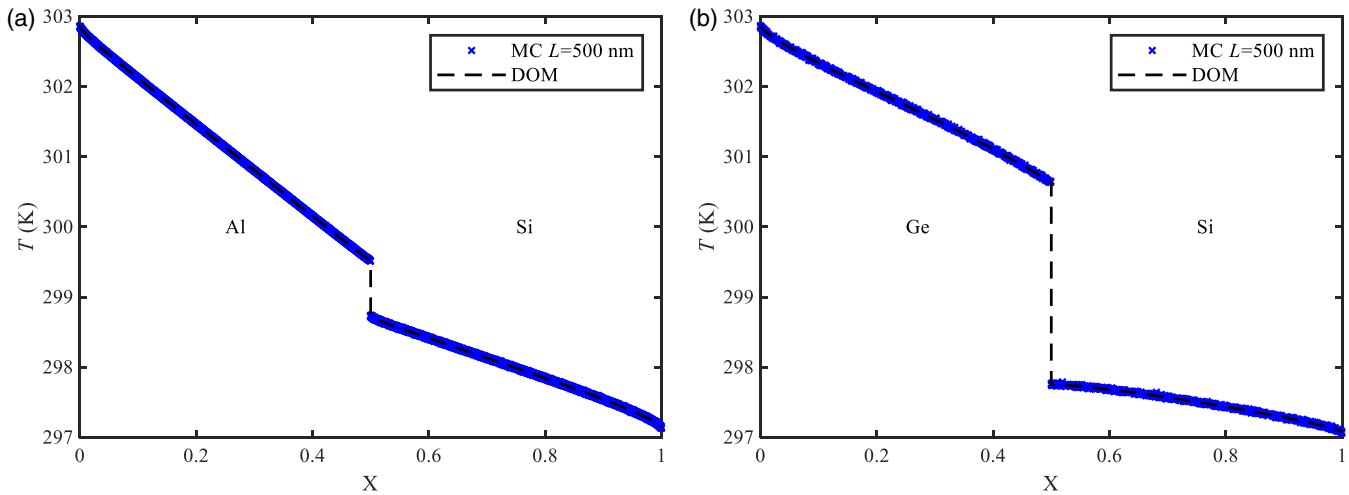

FIG. 6. The temperature distribution of all cells in the bilayer films at the total thickness as 500 nm: (a) Al/Si and (b) Ge/Si.

this model is currently the most appropriate theoretical model at room temperature [24]. For this thickness, the above way to determine the temperature jump at the interface is also verified at the adopted interface roughnesses. The thermal boundary conductances predicted by the present SMMM are 363, 389, 457, 542, and 552 MW/(m^2 K), respectively, close to the experiments 305–385 MW/(m^2 K) [66,67], validating the present SMMM and Monte Carlo method. Furthermore, the predictions by the present SMMM are better than that by SDMM as 572 MW/(m^2 K) [12,24], indicating that the specular scattering contributes significantly to phonon-interface scattering in experiments. It should be noted that thermal boundary conductance predicted by SDMM in this paper is different from that in Ref. [67]. The reason for this is that the thermal boundary conductance in Ref. [67] is calculated by Landauer formalism, based on emitted phonon temperatures, but the present simulation results are obtained based on equivalent equilibrium temperatures. Two definitions for the temperature have different physical meanings. The previous one denotes the ideal temperature and is defined as conjectured phonons emitted ballistically from the boundary at this emitted phonon temperature with infinite mean free paths. For the latter one, considering the strongly nonequilibrium effect, the equilibrium temperature near the interface cannot be defined using the conventional way based on the thermal equilibrium state. Thus, the equivalent equilibrium temperature is defined to reproduce the average energy of all phonons near the interface [12,20] and calculated as above, which is consistent with the experiments. Through above comparisons, the present SMMM and Monte Carlo framework for spectral specularity and spectral specular and spectral diffuse scatterings at heterogeneous interfaces have been validated.

IV. RESULTS AND DISCUSSIONS

This section will first give the transmissivities predicted by the present SMMM and then apply the Monte Carlo method with the SMMM to investigate the roughness dependence of phonon-interface thermal transport across bilayer films with planar and nanostructured interfaces. The impact of nanostructured interfaces on thermal boundary conductance will be studied in detail.

A. Spectral and angular-dependent transmissivity

To investigate the impact of the interface roughness on interfacial phonon transport, the dependence of spectral specularity and spectral transmissivity on interface roughness is studied based on the SMMM first. Two material pairs are considered, i.e., Al/Si and Ge/Si, with the same dispersions and relaxation times in Sec. III. Their spectral specularities are calculated by Eq. (32), dependent on the phonon wavelength and interface roughness. Although the transmissivities of the optical polarizations equal 0 due to the neglect of the inelastic scattering and polarization conversion, their contributions to interfacial phonon transport are nonnegligible by scattering with low-frequency phonons near the interface [68]. Therefore, the specularities of the optical polarizations are still calculated. Figures 7 and 8 give the spectral specularities for two acoustic polarizations of Si, Al, and Ge and two optical polarizations of Si and Ge at interface roughnesses being 0.02, 0.06, and 1 nm. For acoustic polarizations, as Fig. 7 shows, due to different spectra for three materials, the wavelengths of phonons with the same frequency should be different, and thus, spectral specularities on each side are also different. The specularity increases with decreasing phonon frequency and finally approaches 1. This is because, with decreasing phonon frequency, the wave number of the acoustic phonon decreases, and its wavelength increases and becomes increasingly larger than the interface roughness. Acoustic phonons with larger wavelengths are more likely to be scattered specularly by the interface so their specularities are larger. The acoustic phonons with frequencies approaching 0, whose wavelengths are close to infinity, will be nearly completely specularly scattered, and their specularities are $\sim$1. However, the relationship between the specularity and phonon frequency for the optical polarizations is different from the acoustic polarizations. As Fig. 8 shows, the specularity increases with increasing phonon frequency, opposite to the acoustic polarizations, and finally approaches 1. The reason for this is that the relationship between the phonon wavelength and phonon frequency of the optical polarizations is opposite to that of the acoustic polarizations. With increasing phonon frequency, the wave number of the optical phonon decreases, and its wavelength increases, and thus, the specularity increases as well. The wavelengths of optical phonons with frequencies approaching the maximum value are close to infinity, and they will undergo nearly completely specular scattering with specularities $\sim$1.

After obtaining the specularity, the total phonon transmissivity can be calculated through Eqs. (33) and (34). As Sec. II shows, the transmissivity predicted by the SMMM depends on both phonon frequency and incident angle. Therefore, to first plot the relationship between the transmissivity and the frequency, an average spectral transmissivity over the incident angle is defined with detailed derivations as below. The heat flux in Eq. (10) equals 0, so the equation below is valid:

$$\sum_p \int_0^1 \int_0^{\omega_{\max,p}} \alpha_{ij}(\theta_i, \omega, \mathrm{p}) C_i(\omega, \mathrm{p}) v_{\mathrm{g},i}(\omega, \mathrm{p}) \mu_i d\omega d\mu_i = \sum_p \int_0^1 \int_0^{\omega_{\max,p}} \alpha_{ji}(\theta_j, \omega, \mathrm{p}) C_j(\omega, \mathrm{p}) v_{\mathrm{g},j}(\omega, \mathrm{p}) \mu_j d\omega d\mu_j. \tag{39}$$

Based on Eqs. (15) and (16), the equation below is obtained:

$$\int_0^1 \alpha_{ij}(\theta_i, \omega, \mathrm{p}) C_i(\omega, \mathrm{p}) v_{\mathrm{g},i}(\omega, \mathrm{p}) \mu_i d\mu_i = \int_0^1 \alpha_{ji}(\theta_j, \omega, \mathrm{p}) C_j(\omega, \mathrm{p}) v_{\mathrm{g},j}(\omega, \mathrm{p}) \mu_j d\mu_j. \tag{40}$$

Equation (40) is the result of the application of the principle of detailed balance to the total phonon transmissivity. Then the average spectral transmissivities in different directions are

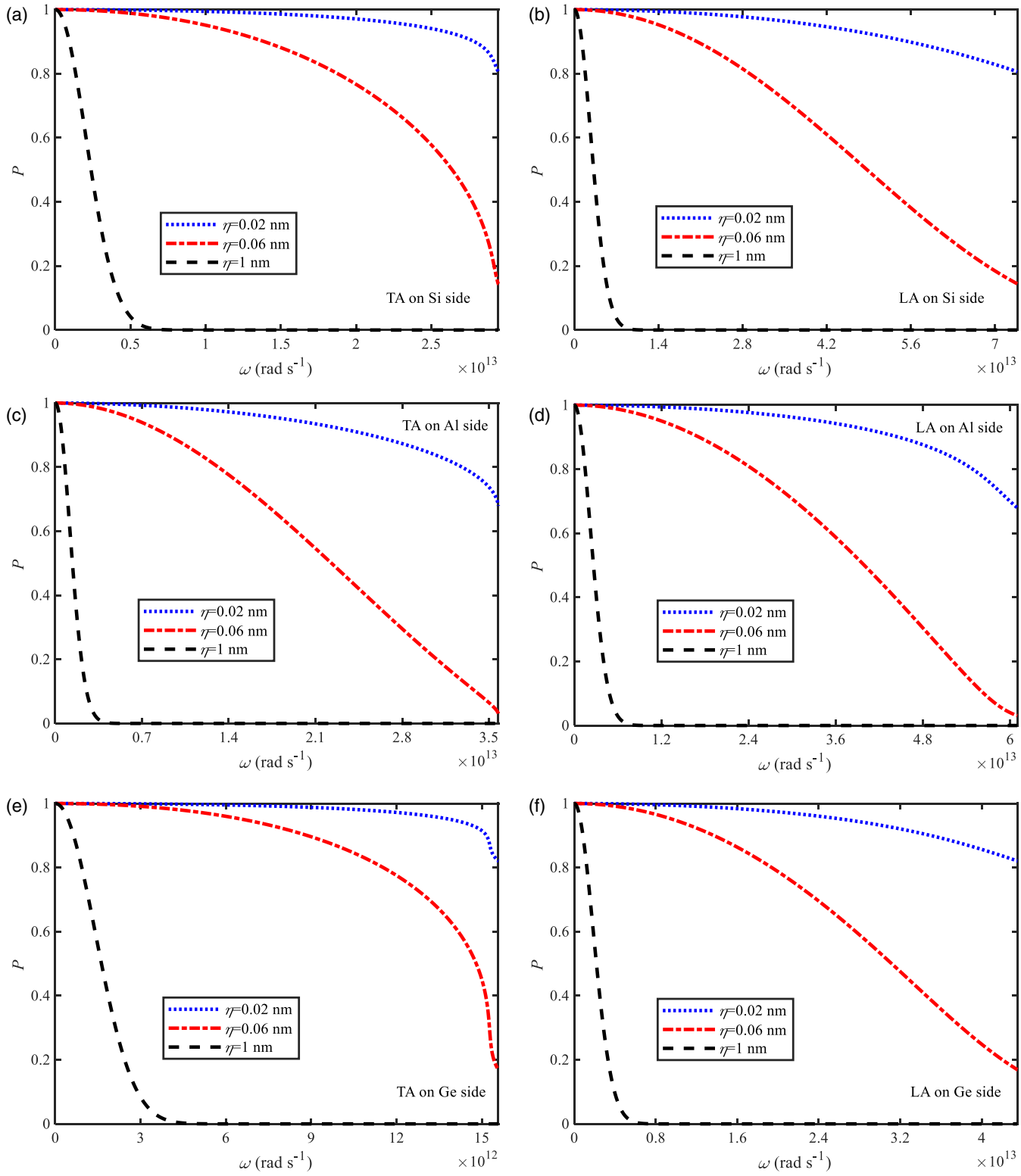

FIG. 7. The spectral specularity for various acoustic polarizations of three materials at three interface roughnesses: (a) transverse acoustic phonons on Si side, (b) longitudinal acoustic phonons on Si side, (c) transverse acoustic phonons on Al side, (d) longitudinal acoustic phonons on Al side, (e) transverse acoustic phonons on Ge side, and (f) longitudinal acoustic phonons on Ge side. Blue dot lines, red dot dash lines, and double dash lines represent the specularities with interface roughness being 0.02, 0.06, and 1 nm, respectively. TA and LA refer to transverse and longitudinal acoustic polarizations, respectively.

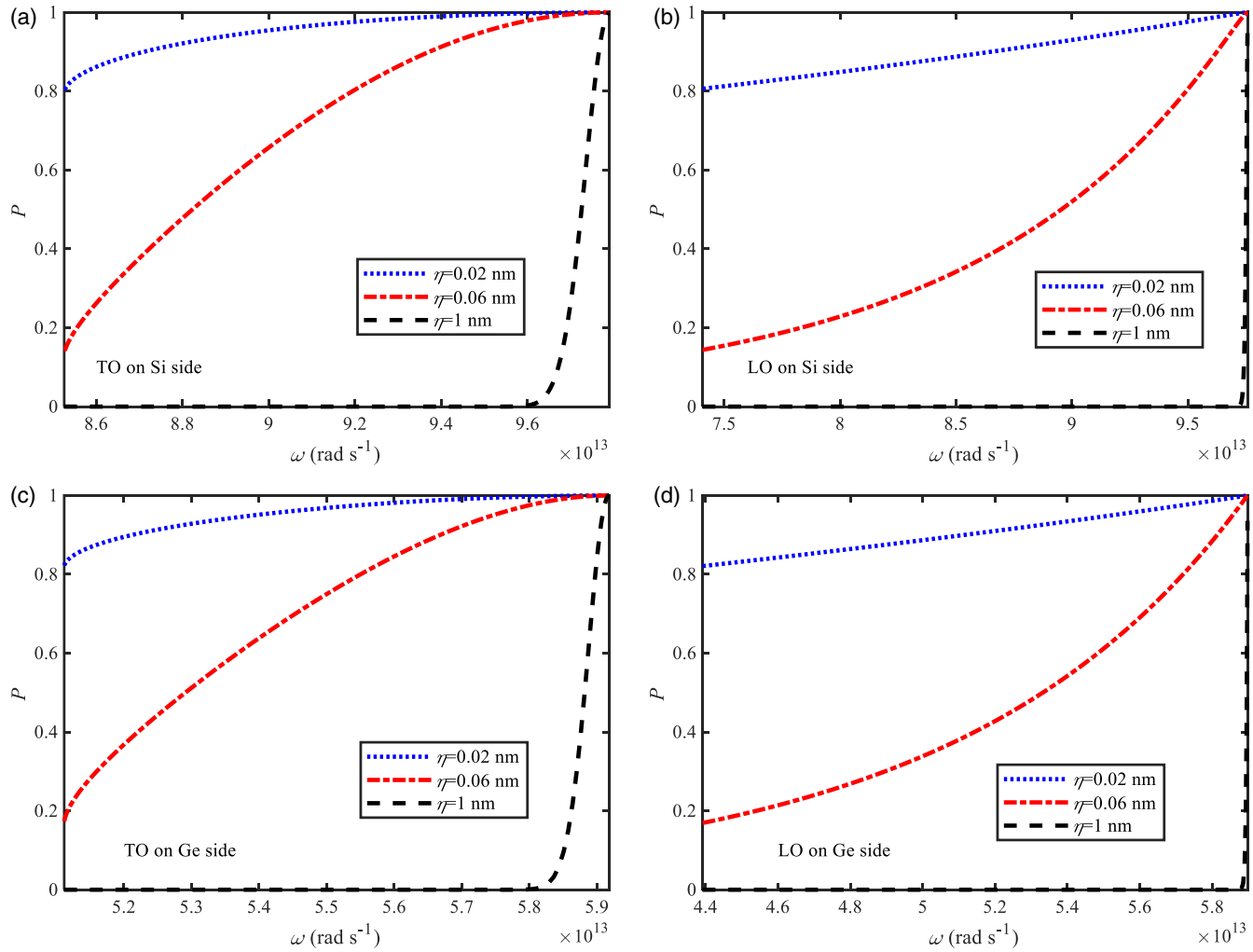

FIG. 8. The spectral specularity for various optical polarizations of three materials at three interface roughnesses: (a) transverse optical phonons on Si side, (b) longitudinal optical phonons on Si side, (c) transverse optical phonons on Ge side, and (d) longitudinal optical phonons on Ge side. TO and LO refer to transverse and longitudinal optical polarizations, respectively.

defined as

$$\int_0^1 \bar{\alpha}_{ij}(\omega, \mathrm{p}) C_i(\omega, \mathrm{p}) v_{\mathrm{g},i}(\omega, \mathrm{p}) \mu_i d\mu_i = \int_0^1 \alpha_{ij}(\theta_i, \omega, \mathrm{p}) C_i(\omega, \mathrm{p}) v_{\mathrm{g},i}(\omega, \mathrm{p}) \mu_i d\mu_i, \tag{41}$$

$$\int_0^1 \bar{\alpha}_{ji}(\omega, \mathrm{p}) C_j(\omega, \mathrm{p}) v_{\mathrm{g},j}(\omega, \mathrm{p}) \mu_j d\mu_j = \int_0^1 \alpha_{ji}(\theta_j, \omega, \mathrm{p}) C_j(\omega, \mathrm{p}) v_{\mathrm{g},j}(\omega, \mathrm{p}) \mu_j d\mu_j. \tag{42}$$

The average spectral transmissivities are finally given as

$$\bar{\alpha}_{ij}(\omega, \mathrm{p}) = \frac{2\int_0^1 \alpha_{ij}(\theta_i, \omega, \mathrm{p}) C_i(\omega, \mathrm{p}) v_{\mathrm{g},i}(\omega, \mathrm{p}) \mu_i d\mu_i}{C_i(\omega, \mathrm{p}) v_{\mathrm{g},i}(\omega, \mathrm{p})}, \tag{43}$$

$$\bar{\alpha}_{ji}(\omega, \mathrm{p}) = \frac{2\int_0^1 \alpha_{ji}(\theta_j, \omega, \mathrm{p}) C_j(\omega, \mathrm{p}) v_{\mathrm{g},j}(\omega, \mathrm{p}) \mu_j d\mu_j}{C_j(\omega, \mathrm{p}) v_{\mathrm{g},j}(\omega, \mathrm{p})}. \tag{44}$$

Figures 9 and 10 show the average spectral transmissivities for various polarizations of Al/Si and Ge/Si at four interface roughnesses being 0, 0.02, 0.06, and 1 nm, varying differently with the frequency. For Al/Si, the transmissivity of the low-frequency phonon decreases with increasing interface roughness, but the pattern is opposite for the high-frequency phonon. For Ge/Si, at smaller interface roughnesses, the transmissivity for both low- and high-frequency phonons decreases with increasing interface roughness. However, at larger interface roughnesses, the transmissivity of the low-frequency phonon decreases with increasing interface roughness, and the pattern is opposite for the high-frequency phonon, like Al/Si. It is noted that the transmissivity from Si to Ge for the phonon with frequency $\sim 0 \approx 0.845$, very close to the value in Ref. [23] as 0.85.

Additionally, the relationships between the transmissivity and incident angle at four interface roughnesses as 0, 0.02, 0.06, and 1 nm are directly obtained by Eqs. (33) and (34) and shown in Figs. 11–14, where phonon frequencies are fixed at 1×10^{13} and 2×10^{13} rad/s for Al/Si and 0.5×10^{13} and 1×10^{13} rad/s for Ge/Si. The illustrations for these

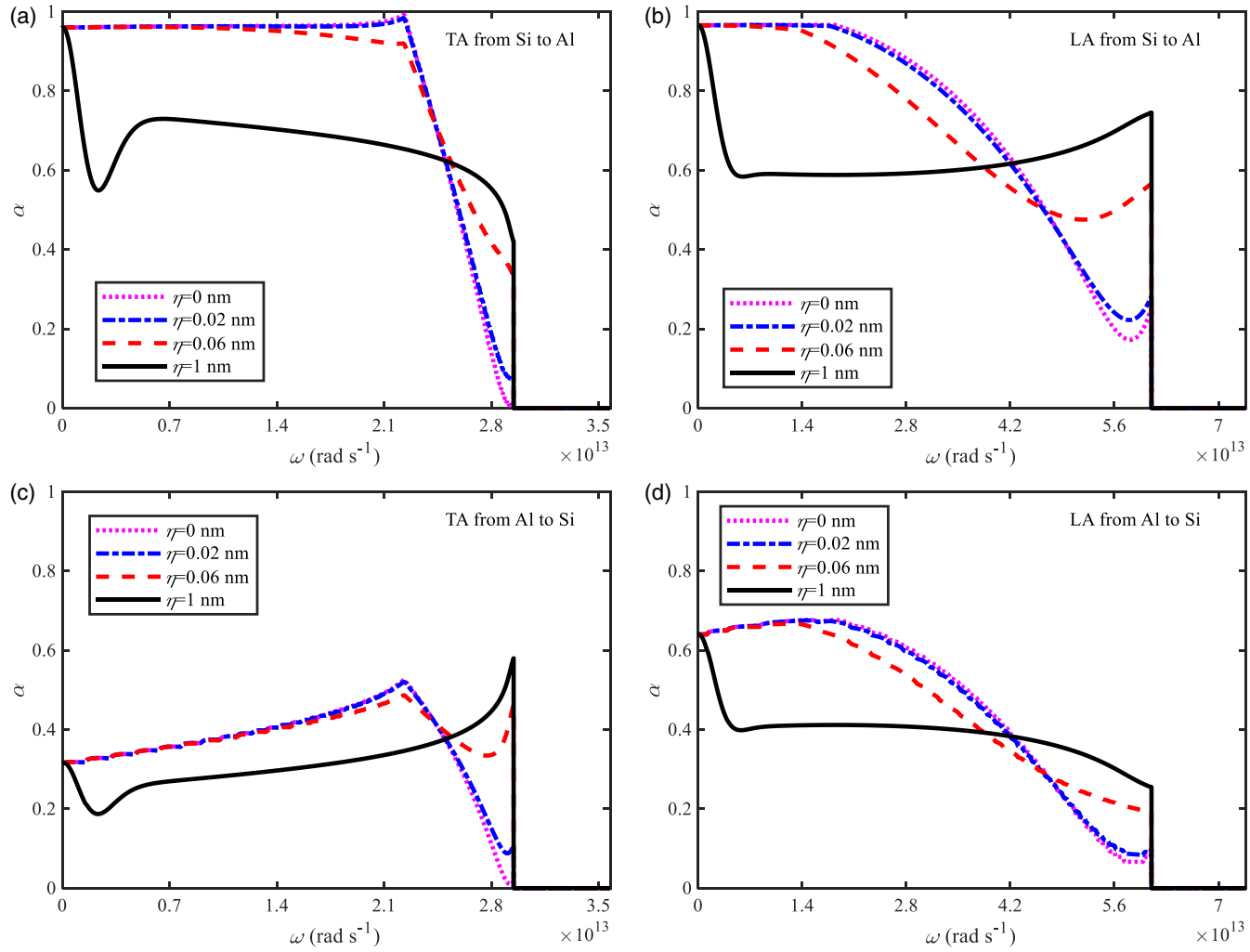

FIG. 9. The average spectral transmissivity for various polarizations of Al/Si in different directions at four interface roughnesses: (a) transverse acoustic phonons from Si to Al, (b) longitudinal acoustic phonons from Si to Al, (c) transverse acoustic phonons from Al to Si, and (d) longitudinal acoustic phonons from Al to Si.

relationships are given as follows: (a) for the interface roughness being 0 nm, the specularity equals 1 throughout the entire incident angle range, so phonons will be completely specularly scattered by the interface. There are cutoff angles for some cases, which correspond to the critical angle for the total reflection for specular scattering. For the relationship with the critical angle, phonons will completely specularly transmit across the interface or be reflected and be completely specularly reflected, for the incident angle smaller and larger than the critical angle, respectively. For the relationship without the critical angle, phonons will completely specularly transmit across the interface or be reflected. (b) For the interface roughness being 0.02 and 0.06 nm, the transmissivity significantly monotonically increases with decreasing incident angle, and there are also critical angles for some cases. As shown in Fig. 7, the specularities for these cases are <1 and >0, and hence, the transmissivities for both specular and diffuse scatterings should be >0. Accordingly, phonons will be partially specularly and partially diffusely scattered by interface. Considering the cases with the critical angles, phonons will partially specularly and partially diffusely transmit across the interface or be reflected below the critical angles but will completely diffusely transmit across the interface and be partially specularly and partially diffusely reflected upper the critical angles. Considering the cases without the critical angles, phonons will partially specularly and partially diffusely transmit across the interface or be reflected throughout the entire incident angle range. Due to the large specularities shown in Fig. 7, the specular scattering dominates over the diffuse scattering at these two interface roughnesses. (c) For the interface roughness being 1 nm, with reducing incident angle, the transmissivity monotonically increases by a small amount or almost keeps constant, and the critical angles also exist for some cases. Since the specularities for these cases are <1 and >0, the transmissivity for both specular and diffuse scatterings should also be >0. For the cases with the critical angle, phonons will partially specularly and partially diffusely transmit across the interface or be reflected below the critical angle and will completely diffusely transmit across the interface and be partially specularly and partially diffusely reflected upper the critical angle. Phonons will partially specularly and partially diffusely transmit across the interface or

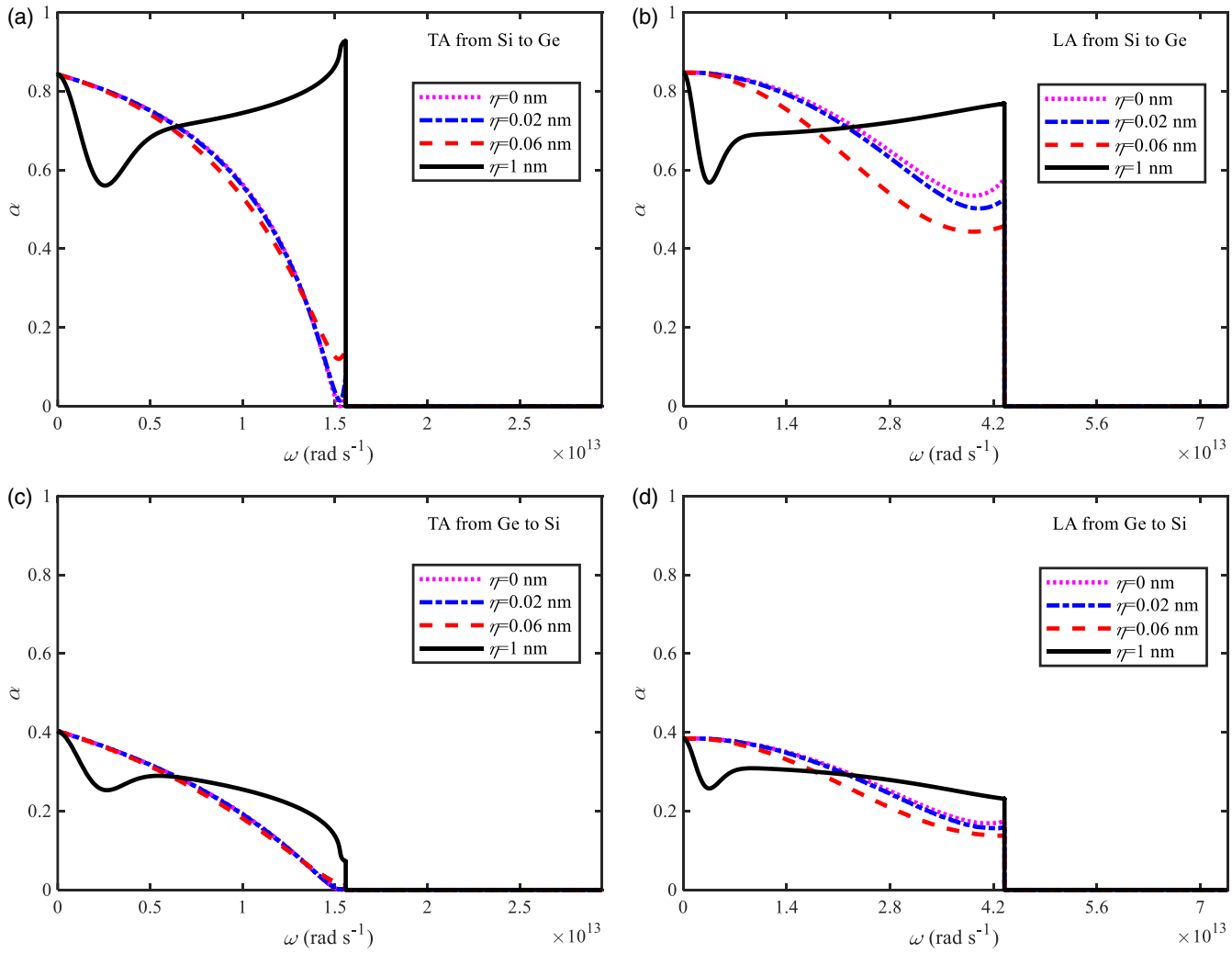

FIG. 10. The average spectral transmissivity for various polarizations of Ge/Si in different directions at four interface roughnesses: (a) transverse acoustic phonons from Si to Ge, (b) longitudinal acoustic phonons from Si to Ge, (c) transverse acoustic phonons from Ge to Si, and (d) longitudinal acoustic phonons from Ge to Si.

be reflected throughout the entire incident angle range for the cases without the critical angle. Since only the transmissivity for the diffuse scattering is angular independent, phonons will undergo nearly completely diffuse scattering at the interface for the cases with the approximately constant transmissivity. Owing to the small specularities shown in Fig. 7, the interface scattering for interface roughness being 1 nm is dominated by the diffuse scattering.

To further verify the SMMM, the present angular-dependent transmissivity at the interface roughness as 0 nm is compared with that by the atomistic Green's function (AGF) method from Ref. [47]. Two phonon frequencies from Ge to Si are considered, i.e., 1 and 4 THz, shown in Figs. 15(a) and 15(b), respectively. For the phonon frequency being 1 THz, the transmissivities for both transverse and longitudinal acoustic polarizations by the SMMM agree well with those by AGF, especially at the small incident angle. It means that the present SMMM can capture the physical mechanisms of interface scattering at low phonon frequencies. However, for the phonon frequency being 4 THz, the transmissivity by the SMMM significantly deviates from that by AGF. It indicates that the present SMMM cannot accurately describe the relationship between the transmissivity and incident angle at high phonon frequencies. Above all, it is inferred that the neglect of inelastic scattering and polarization conversion and the consideration of isotropic dispersions in the present SMMM are more accurate and less accurate at low and high phonon frequencies, respectively.

B. Planar interface

The physical model in Fig. 2(b) is still adopted for the case of the planar interface. Al/Si and Ge/Si are considered using the same dispersions and relaxation times as in Sec. III with volume ratios as 1. To avoid the high computational cost of the Monte Carlo method for large-scale films, two small total thicknesses are used, i.e., $L = 40$ and 60 nm, with the total numbers of energy packets as 40 million and 60 million, respectively. The boundary temperatures on the left and right sides are fixed at 303 and 297 K. To reveal the roughness dependence of phonon-interface thermal transport, the interface roughnesses are varied from 0.02 to 0.2 nm with a common

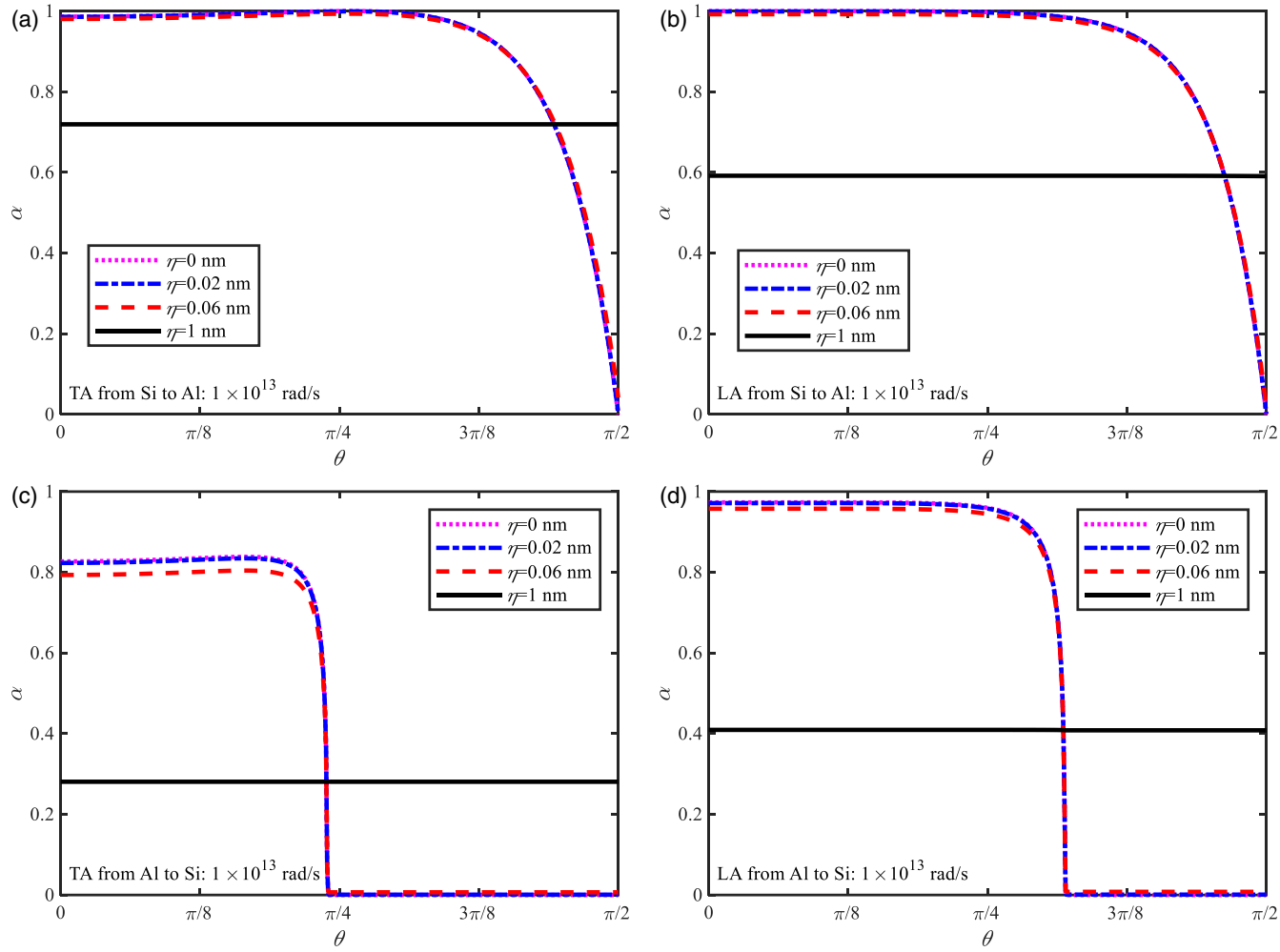

FIG. 11. The angular-dependent transmissivity of phonons with frequency as 1×10^{13} rad/s for various polarizations of Al/Si in different directions at four interface roughnesses: (a) transverse acoustic phonons from Si to Al, (b) longitudinal acoustic phonons from Si to Al, (c) transverse acoustic phonons from Al to Si, and (d) longitudinal acoustic phonons from Al to Si.

difference 0.02 nm and from 0.2 to 1.8 nm with a common difference 0.2 nm. The present setting for the interface roughness is roughly consistent with the experiments, typically within 0.11 ± 0.04 nm [22]. The thermal conductivity and thermal boundary conductance are calculated based on the steady-state temperature distributions and heat fluxes, using formulas $\kappa = qL/(T_L - T_R)$ and $G = q/\Delta T$, respectively. The temperature jump at the interface is determined through the same way as in Sec. III B, which has also been demonstrated to be effective for these two thicknesses at the adopted interface roughnesses. It should be noted that, as the previous section shows, the boundary scattering effect is nonnegligible and will influence the thermal boundary conductance at these two thicknesses. However, this paper only concerns the roughness dependence of the interface on the thermal conductivity and thermal boundary conductance, which is revealed at the fixed length and volume ratio. The nonequilibrium effects from boundary scattering are roughly equivalent for the fixed length and volume ratio so the size effect should not be included. The purpose of using two total thicknesses is to investigate whether the roughness dependences are different at different sizes. Therefore, even though the thermal boundary conductance differs from that for bulk materials due to the boundary scattering, its value still has reference significance for small-scale films, and its roughness dependence and corresponding analyses and explanations below are meaningful for other systems. This note is also valid for the following two parts on nanostructured interfaces.

Figure 16 gives the thermal conductivity and the thermal boundary conductance, showing nonmonotonic relationships with the interface roughness and different variation trends for two material pairs but similar variation trends for two total thicknesses. For Al/Si, the thermal conductivity and thermal boundary conductance first increase, next decrease, and then slightly increase with increasing interface roughness, ultimately tending to a constant. For Ge/Si, the thermal conductivity and thermal boundary conductance first decrease, then increase with increasing interface roughness, ultimately tending to a constant. Here, $\eta = 0.06$ nm gives the minimum thermal boundary conductance for Ge/Si. This nonmonotonic relationship is different from the conventional understanding based on the frequency-independent specularity, providing the monotonic relationship with minimum and maximum thermal boundary conductances at completely specular and

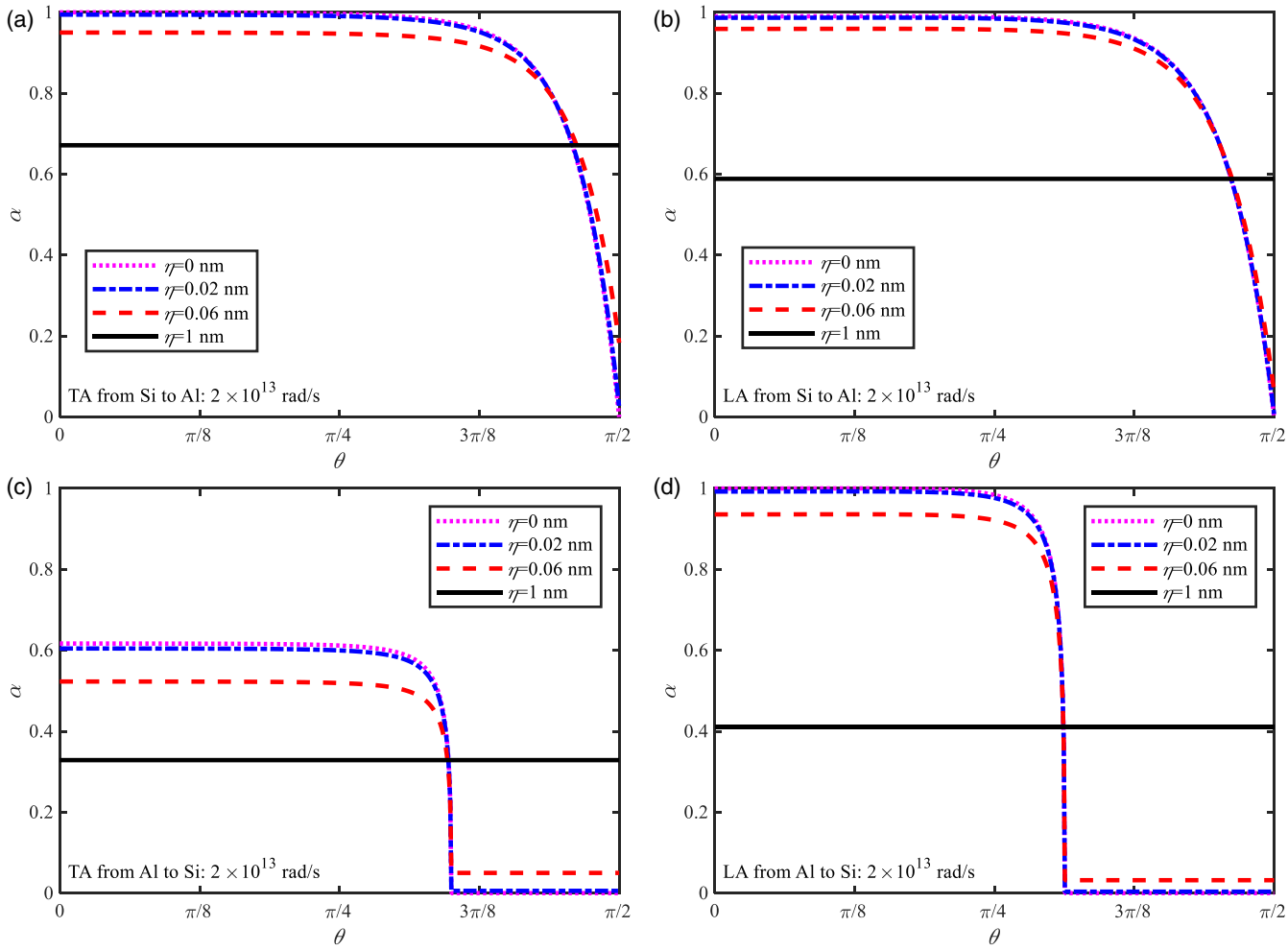

FIG. 12. The angular-dependent transmissivity of phonons with frequency as 2×10^{13} rad/s for various polarizations of Al/Si in different directions at four interface roughnesses: (a) transverse acoustic phonons from Si to Al, (b) longitudinal acoustic phonons from Si to Al, (c) transverse acoustic phonons from Al to Si, and (d) longitudinal acoustic phonons from Al to Si.

completely diffuse scatterings. A similar conclusion is found in Ref. [28], but the details differ, as its specular scattering is frequency independent. The nonmonotonic relationship is attributed to the spectral specularity, which will be roughly explained using Landauer formalism at first. Thermal boundary conductance in Landauer formalism is dependent on the phonon transmissivity, given as below [67]:

$$G = 2\pi \sum_p \int_0^{\pi/2} \int_0^{\omega_{\max,p}} \alpha_{ij}(\theta_i, \omega, \mathrm{p}) C_i(\omega, \mathrm{p}) v_{\mathrm{g},i}(\omega, \mathrm{p}) \times \cos\theta_i \sin\theta_i d\omega d\theta_i. \quad (45)$$

Considering partially specular and partially diffuse scattering, the phonon transmissivity is derived through weighted averaging, with the weight being the specularity, and the following equation is obtained:

$$G = 2\pi \sum_p \int_0^{\pi/2} \int_0^{\omega_{\max,p}} [P_i \alpha_{\mathrm{Specular},ij} + (1 - P_i)\alpha_{\mathrm{Diffuse},ij}] \times C_i(\omega, \mathrm{p}) v_{\mathrm{g},i}(\omega, \mathrm{p}) \cos\theta_i \sin\theta_i d\omega d\theta_i. \quad (46)$$

For frequency-independent specularity, Eq. (46) can be rewritten as

$$G = 2\pi P_i \sum_p \int_0^{\pi/2} \int_0^{\omega_{\max,p}} \alpha_{\mathrm{Specular},ij} C_i(\omega, \mathrm{p}) v_{\mathrm{g},i}(\omega, \mathrm{p}) \times \cos\theta_i \sin\theta_i d\omega d\theta_i + 2\pi(1 - P_i) \sum_p \int_0^{\pi/2} \int_0^{\omega_{\max,p}} \alpha_{\mathrm{Diffuse},ij} C_i(\omega, \mathrm{p}) v_{\mathrm{g},i}(\omega, \mathrm{p}) \times \cos\theta_i \sin\theta_i d\omega d\theta_i. \quad (47)$$

Equation (47) indicates that thermal boundary conductance varies monotonically with the specularity. Therefore, the minimum and maximum thermal boundary conductances are obtained at completely specular scattering and completely diffuse scattering. However, for spectral specularity, Eq. (47) cannot be deduced from Eq. (45), so the minimum or maximum thermal boundary conductance cannot be obtained at completely specular or completely diffuse scattering.

To provide more in-depth explanations for this nonmonotonic roughness dependence of thermal boundary conduc-

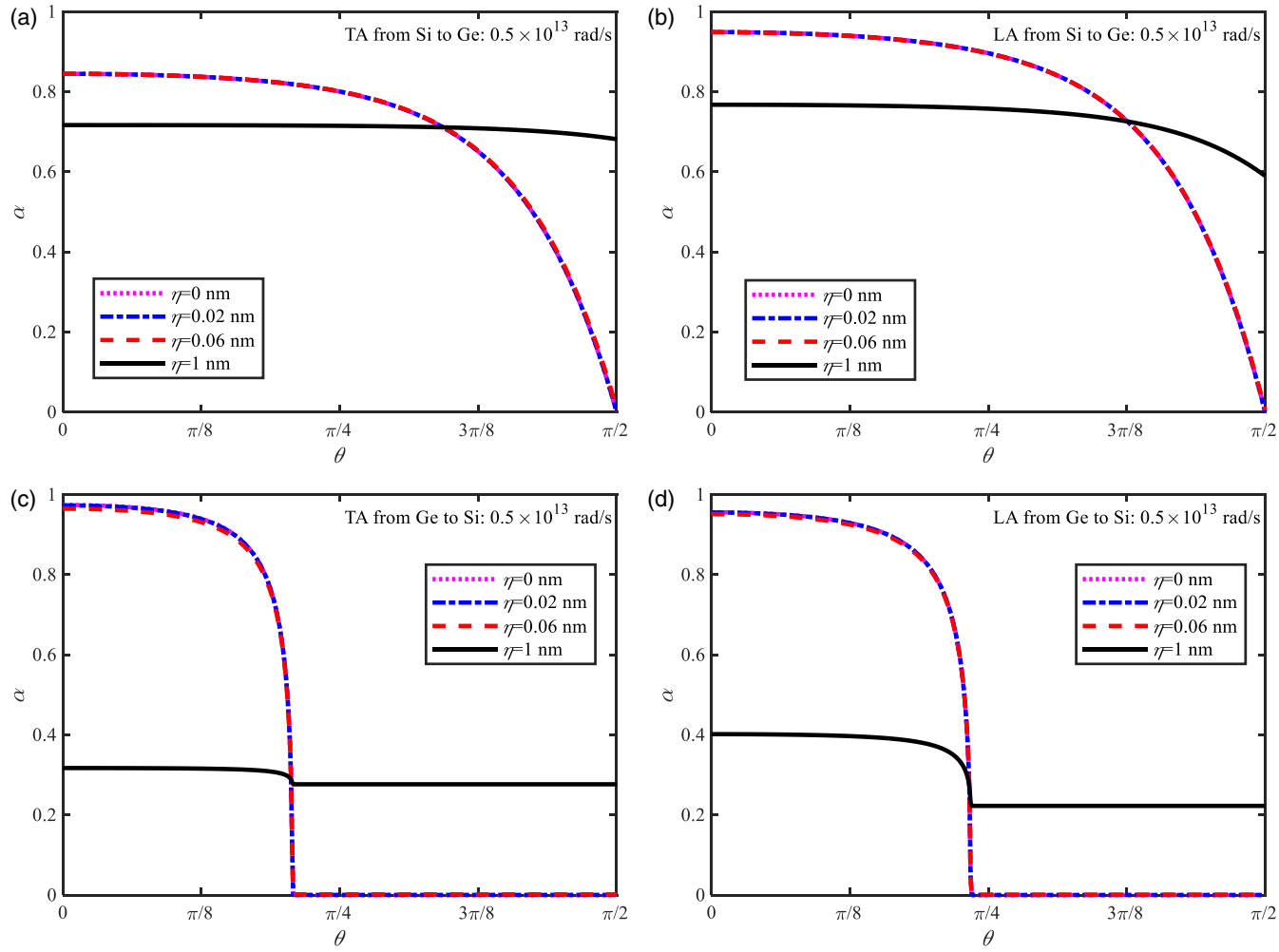

FIG. 13. The angular-dependent transmissivity of phonons with frequency as 0.5×10^{13} rad/s for various polarizations of Ge/Si in different directions at four interface roughnesses: (a) transverse acoustic phonons from Si to Ge, (b) longitudinal acoustic phonons from Si to Ge, (c) transverse acoustic phonons from Ge to Si, and (d) longitudinal acoustic phonons from Ge to Si.

tance, the spectral thermal boundary conductances are defined as below based on Landauer formalism:

$$G_{ij}(\omega, \mathrm{p}) = \int_0^1 \alpha_{ij}(\theta_i, \omega, \mathrm{p}) C_i(\omega, \mathrm{p}) v_{\mathrm{g},i}(\omega, \mathrm{p}) \mu_i d\mu_i, \quad (48)$$

$$G_{ji}(\omega, \mathrm{p}) = \int_0^1 \alpha_{ji}(\theta_j, \omega, \mathrm{p}) C_j(\omega, \mathrm{p}) v_{\mathrm{g},j}(\omega, \mathrm{p}) \mu_j d\mu_j. \quad (49)$$

With Eqs. (43) and (44), the spectral thermal boundary conductances are rewritten as

$$G_{ij}(\omega, \mathrm{p}) = 2\bar{\alpha}_{ij}(\omega, \mathrm{p}) C_i(\omega, \mathrm{p}) v_{\mathrm{g},i}(\omega, \mathrm{p}), \quad (50)$$

$$G_{ji}(\omega, \mathrm{p}) = 2\bar{\alpha}_{ji}(\omega, \mathrm{p}) C_j(\omega, \mathrm{p}) v_{\mathrm{g},j}(\omega, \mathrm{p}). \quad (51)$$

Since the thermal boundary conductance calculated by Landauer formalism from side i to j equals that from side j to i at a fixed equilibrium temperature, the explanation below is only based on $G_{ij}(\omega, \mathrm{p})$. Here, $\bar{\alpha}_{ij}(\omega, \mathrm{p})$ has been given in Figs. 9 and 10, and thus, the spectral thermal boundary conductances are obtained in Fig. 17 with i and j referring to Al or Ge and Si, respectively. As the results in Figs. 9, 10, and 17 show, for a fixed material pair, the interface roughness strongly impacts the average spectral transmissivity and the spectral thermal boundary conductance. With increasing interface roughness, the average spectral transmissivity increases for some frequencies but decreases for the others. This will lead to an increase or decrease in spectral thermal boundary conductance, resulting in the nonmonotonic roughness dependence of thermal boundary conductance. Due to different dispersions, the impact of interface roughness on the average spectral transmissivity and the spectral thermal boundary conductance is different for two material pairs, resulting in different dependences. For Al/Si at smaller interface roughnesses, with increasing interface roughness, the average spectral transmissivity and spectral thermal boundary conductance decrease less for low-frequency phonons but increase more for high-frequency phonons, which leads to an increase in thermal boundary conductance. However, their decrease and increase are comparable with each other at larger interface roughnesses, resulting in slight fluctuations in thermal boundary conductance. For Ge/Si at smaller interface roughnesses, with increasing interface roughness, the average spectral

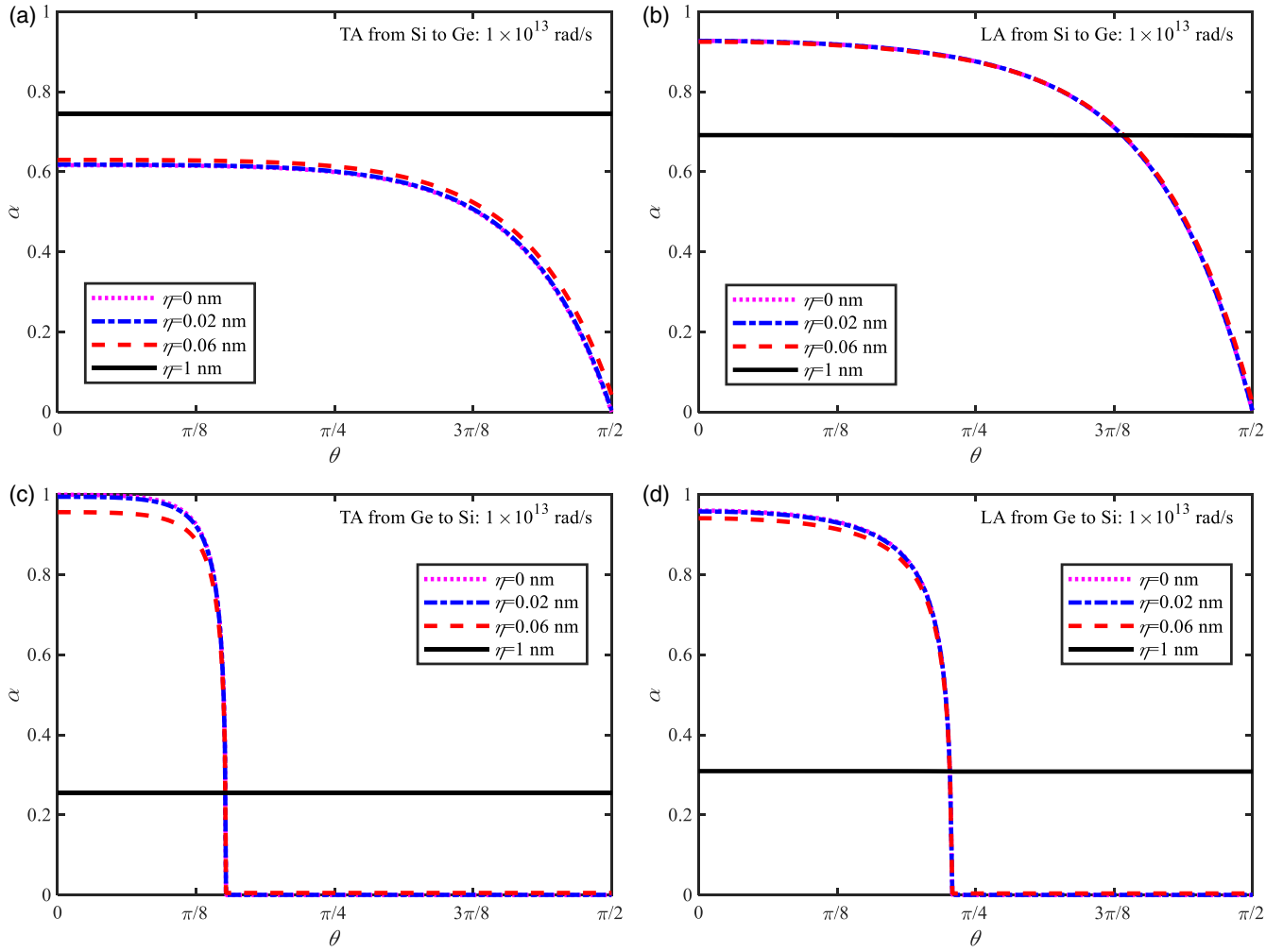

FIG. 14. The angular-dependent transmissivity of phonons with frequency as 1×10^{13} rad/s for various polarizations of Ge/Si in different directions at four interface roughnesses: (a) transverse acoustic phonons from Si to Ge, (b) longitudinal acoustic phonons from Si to Ge, (c) transverse acoustic phonons from Ge to Si, and (d) longitudinal acoustic phonons from Ge to Si.

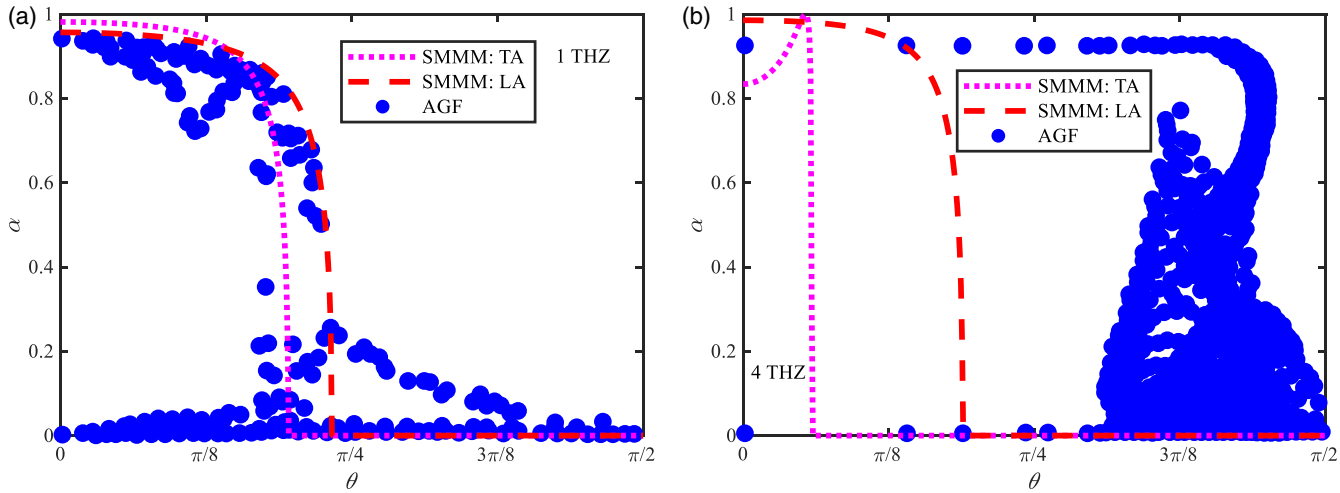

FIG. 15. Comparisons of the angular-dependent transmissivity by the present SMMM and atomistic Green's function (AGF) method at the interface roughness as 0 nm: (a) the transmissivity from Ge to Si at phonon frequency 1 THz and (b) the transmissivity from Ge to Si at phonon frequency 4 THz. The transmissivity by AGF method depicted in blue solid circles is referred to Ref. [47].

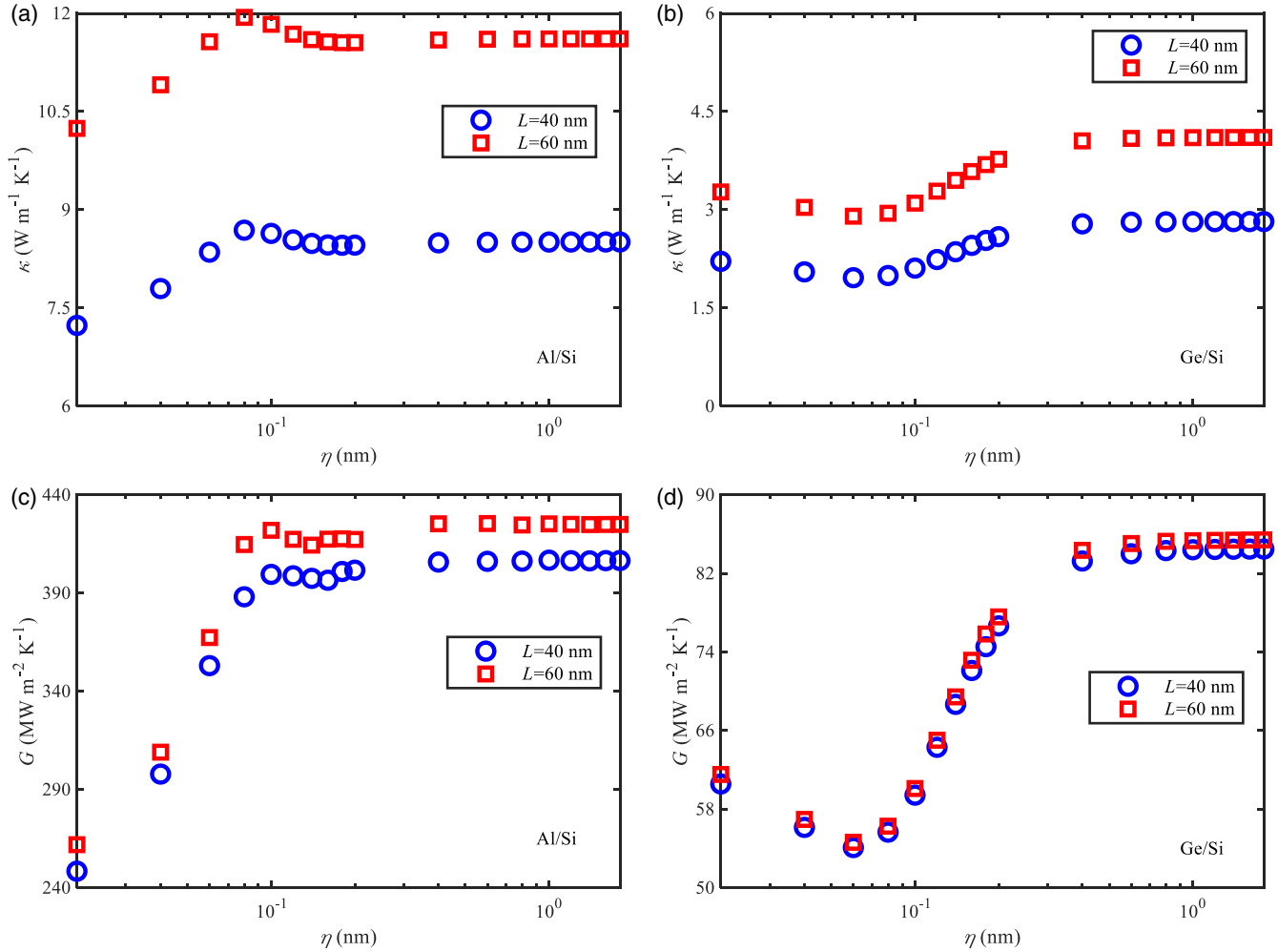

FIG. 16. The thermal conductivity and thermal boundary conductance at various interface roughnesses for bilayer films with planar interface: (a) thermal conductivity of Al/Si film, (b) thermal conductivity of Ge/Si film, (c) thermal boundary conductance of Al/Si film, and (d) thermal boundary conductance of Ge/Si film.

transmissivity and spectral thermal boundary conductance decrease for phonons over a wide frequency range, leading to a decrease in thermal boundary conductance, whereas at larger interface roughnesses, they decrease less for low-frequency phonons but increase more for high-frequency phonons with increasing interface roughness, leading to an increase in thermal boundary conductance. Totally, the nonmonotonic roughness dependence of thermal boundary conductance is the result of the irregular variation of spectral transmissivity by varying the interface roughness, and the dispersions of the material pairs strongly impact this variation and hence the dependence.

C. Nanostructured interface with uniform roughness

After investigating the roughness dependence of phonon-interface thermal transport through the planar interface, in this subsection, we discuss the dependence for nanostructured interfaces with uniform roughness. Three physical models are considered, shown in Fig. 18, i.e., 6 × 6 nm square, 3 × 6 nm rectangle, and 9 × 6 nm rectangle interfaces, with the fixed interface height as 6 nm. The material pairs are made of Al/Si and Ge/Si, with the same dispersions and relaxation times as before. The material volume ratios in all cases are set to 1. The total thicknesses of films are set to $L = 40$ and 60 nm, with the numbers of energy packets of 40 million and 60 million. The reason to select these two total thicknesses is the same as that in the previous part, and the boundary temperatures on the left and right sides are fixed at 303 and 297 K, respectively. The periodic boundary conditions are implemented on the upper and lower sides. The nanostructured interface consists of two kinds of interfaces, namely, the horizontal and vertical interfaces, parallel and perpendicular to the heat flux. Uniform roughness means that the horizontal and vertical interfaces have identical interface roughnesses, varied from 0.02 to 0.2 nm with a common difference 0.02 nm and from 0.2 to 1.8 nm with a common difference 0.2 nm.

The thermal conductivities κ_{eff} are calculated by the formula $\kappa_{\text{eff}} = (L\int_0^{L_y} q_x \mathrm{d}y)/[L_y(T_{\text{L}} - T_{\text{R}})]$ after obtaining the temperature distributions and heat fluxes, where x and y denote horizontal and vertical coordinates, and L_y is the film width in the vertical direction. Figures 19 and 20 give the thermal conductivity of Al/Si and Ge/Si bilayer films with the nanostructured interface at various roughnesses, with those of

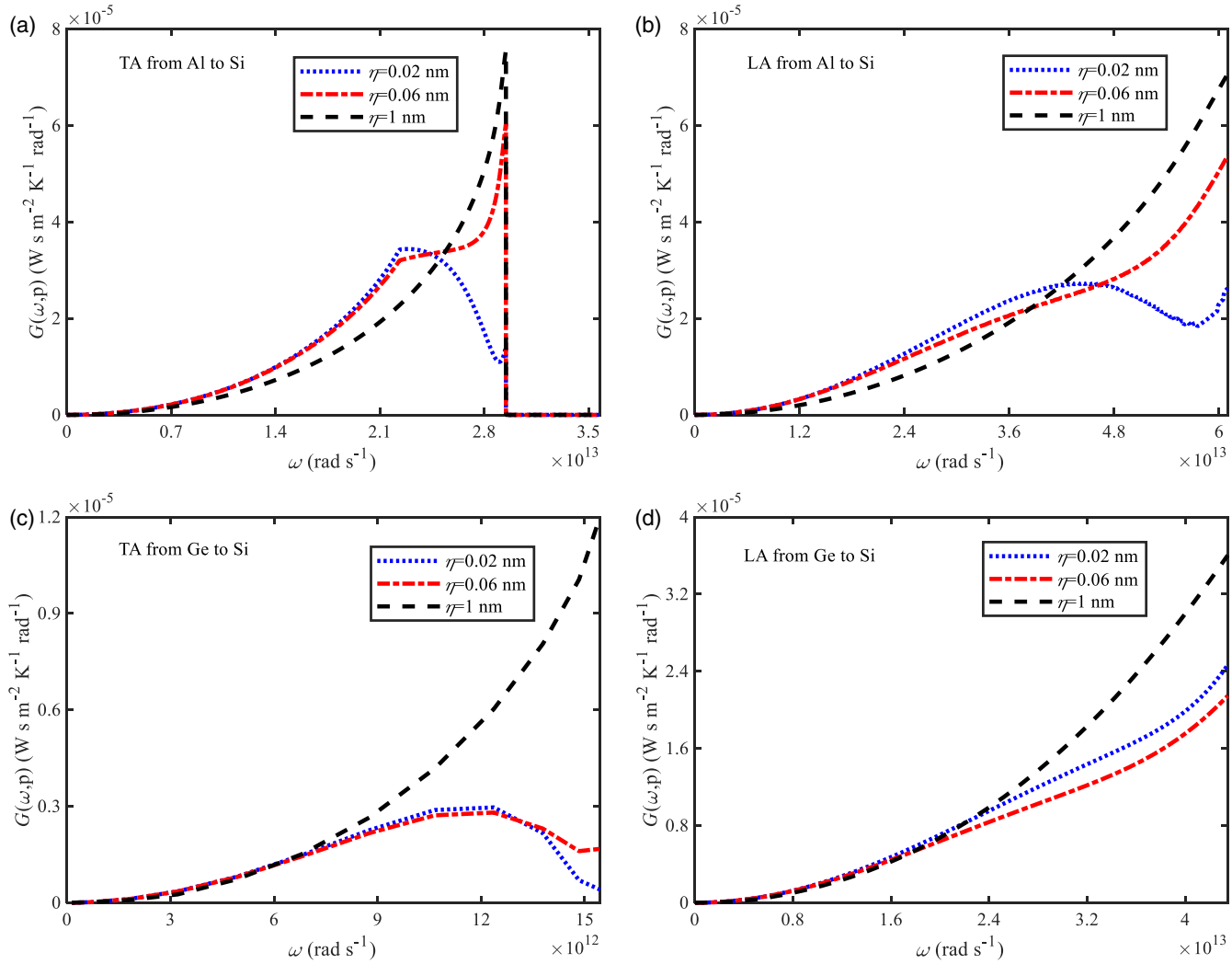

FIG. 17. The spectral thermal boundary conductance for various polarizations of two material pairs at three interface roughnesses: (a) transverse acoustic phonons from Al to Si, (b) longitudinal acoustic phonons from Al to Si, (c) transverse acoustic phonons from Ge to Si, and (d) longitudinal acoustic phonons from Ge to Si.

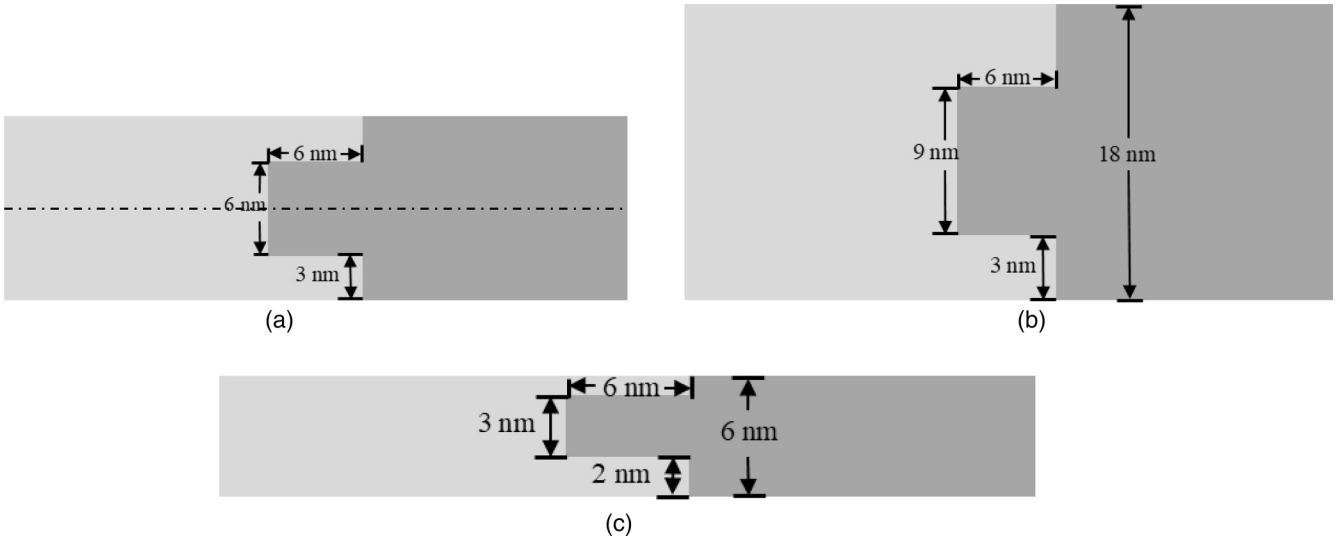

FIG. 18. Bilayer films with nanostructured interface: (a) 6 × 6 nm square interface, (b) 9 × 6 nm rectangle interface, and (c) 3 × 6 nm rectangle interface.

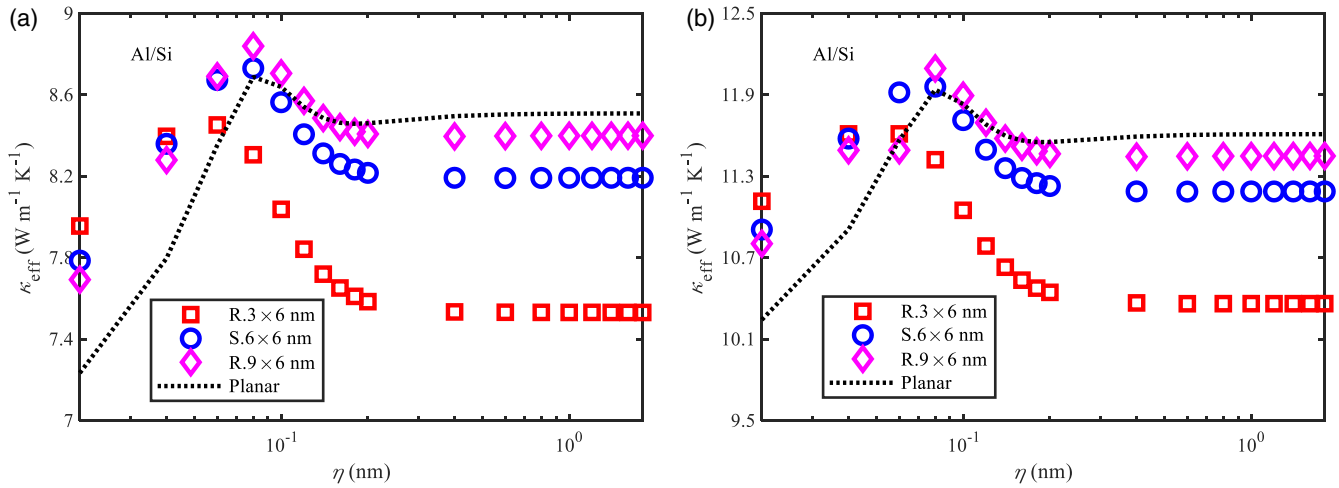

FIG. 19. The thermal conductivity of Al/Si bilayer film with the nanostructured interface with uniform roughness: (a) total thickness as 40 nm and (b) total thickness as 60 nm. R. and S. represent rectangle and square interfaces, respectively.

planar interfaces for comparisons. The results show that the thermal conductivities of nanostructured interfaces are larger and smaller than those of planar interfaces at smaller and larger interface roughnesses, respectively. Due to the same total thickness and volume ratio as well as the same interface roughness, the difference in thermal conductivity between planar and nanostructured interfaces only comes from their different interface geometries. It means that, by introducing the nanostructured interface, interfacial phonon transport is enhanced and suppressed at smaller and larger interface roughnesses, respectively. The thermal boundary conductance is calculated to further investigate the impact of nanostructured interfaces. Since the interface height is small, the lateral heat transport can be ignored, and thermal transport through the nanostructured interface can be regarded as one dimensional. Thus, the one-dimensional model is introduced as below, considering the series relation for thermal resistance [12,69]:

$$\frac{L}{\kappa_{\rm eff}} = R_0 + \frac{1}{G_{\rm eff}}, \tag{52}$$

where R_0 denotes the sum of thermal resistances excluding thermal boundary resistance, including boundary and intrinsic resistances; and $G_{\rm eff}$ is the thermal boundary conductance. Owing to the small interface height, the boundary and intrinsic resistances are roughly equivalent for the films with planar and nanostructured interfaces at the same total thickness and volume ratio and the same interface roughness. Hence, different interface geometries only lead to the different thermal boundary conductances and thermal conductivities at each total thickness, volume ratio, and interface roughness. The thermal boundary conductances of the film with planar interfaces at each interface roughness can be directly calculated through $G = q/\Delta T$, and knowing the thermal conductivity, the sum of its boundary and intrinsic resistances R_0 at each interface roughness can be obtained through Eq. (52). Based on the analyses above, the sum of the boundary and intrinsic resistances of the film with nanostructured interfaces also equals R_0 at the same total thickness and volume ratio and the same interface roughness. Finally, based on their thermal conductivities calculated before, the thermal boundary conductances

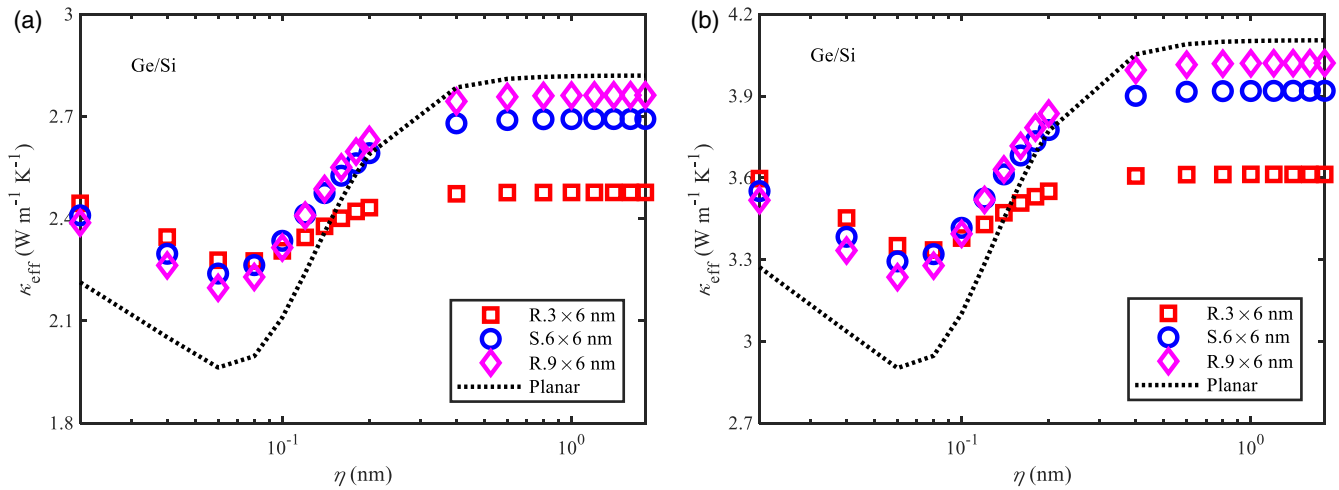

FIG. 20. The thermal conductivity of Ge/Si bilayer film with the nanostructured interface with uniform roughness: (a) total thickness as 40 nm and (b) total thickness as 60 nm.

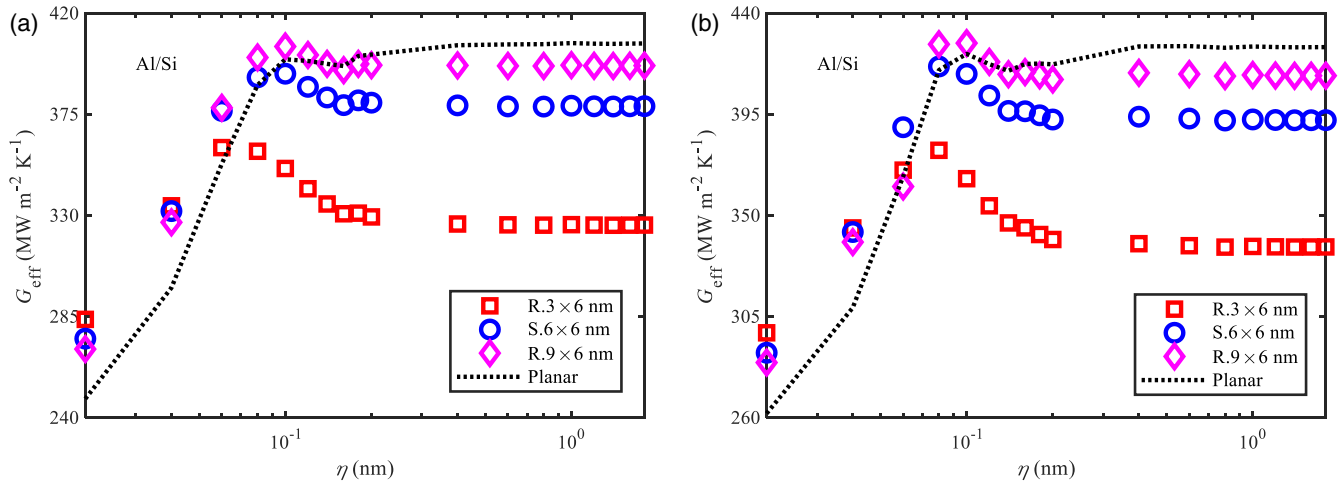

FIG. 21. The thermal boundary conductance of Al/Si bilayer film with the nanostructured interface with uniform roughness: (a) total thickness as 40 nm and (b) total thickness as 60 nm.

of the films with nanostructured interfaces can be obtained at various interface roughnesses. It should be noted that the thermal boundary conductance of nanostructured interfaces at a fixed interface roughness is calculated with R_0 of planar interfaces with the same interface roughness. Therefore, since the way for obtaining the thermal boundary conductance of planar interfaces has been verified in Sec. III B, the calculation of the thermal boundary conductance of nanostructured interfaces is on the same level of accuracy for all nanostructured interfaces at each interface roughness. Figures 21 and 22 give the thermal boundary conductance, with the analogous variation trend to that of the thermal conductivity. At smaller interface roughnesses, the thermal boundary conductance of nanostructured interfaces is larger than that of planar interfaces, but at larger interface roughnesses, it is smaller than that of planar interfaces. As noted before, due to the small interface height, the boundary and intrinsic scattering effects are roughly equivalent at the fixed total length, volume ratio, and interface roughness. Therefore, the difference in thermal boundary conductance between planar and nanostructured interfaces also results from the different interface geometries. Whether to enhance or reduce thermal boundary conductance by nanostructured interfaces strongly depends on the interface roughness. In detail, the small and large interface roughnesses lead to the enhancement and reduction of thermal boundary conductance, respectively, which explains the conclusion in Ref. [12] corresponding to the large interface roughness.

All the above studies are for films with a thickness of tens of nanometers, and further studies in films with larger size are implemented particularly for comparisons with experiments [11,13–15]. The physical model for films with larger size is shown in Fig. 23, and referring to that in Ref. [11], its total size is taken as (87 nm + L_s) × (87 nm + L_s) × 1100 nm with pillar spacing L_s as 15, 57, 104, and 148 nm. For simplicity, the truncated cone in Ref. [11] is approximated as the cuboid with the same volume. The size of the cuboid is derived as 65 nm × 65 nm × L_h with pillar height L_h as 30, 50, and 64 nm. The upper and lower boundaries in the y direction are fixed at 303 and 297 K, respectively,

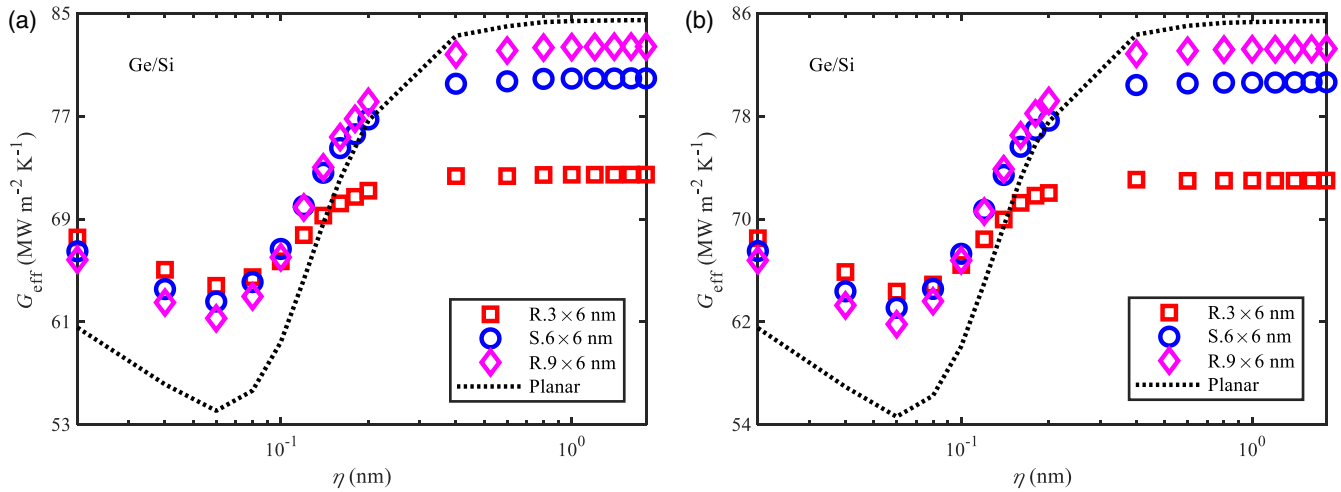

FIG. 22. The thermal boundary conductance of Ge/Si bilayer film with the nanostructured interface with uniform roughness: (a) total thickness as 40 nm and (b) total thickness as 60 nm.

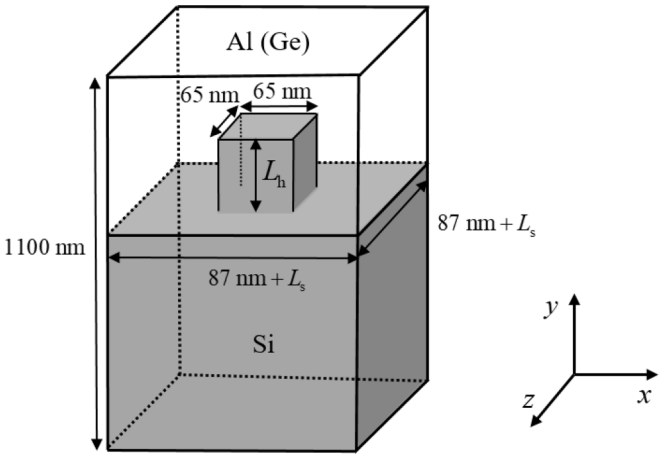

FIG. 23. Three-dimensional physical model for the bilayer film with the nanostructured interface of a cuboid shaped nanopillar.

and periodic boundary conditions are applied along x and z directions. Al/Si is first considered as the material pair for comparisons with experiment with the volume ratio as 1(Al) : 10(Si) for both planar and nanostructured interfaces, and their dispersions and relaxation times are the same as before. Three interface roughnesses are considered, i.e., 0 nm, 0.3 nm, and infinity, referring to completely specular, partially specular and partially diffuse, and completely diffuse scatterings, respectively. The total numbers of energy packets in all simulations are taken as 120 million. Based on Fourier's law, the thermal conductivity is calculated through the formula $\kappa_{\text{eff}} = (L_y \int_0^{L_z} \int_0^{L_x} q_y \mathrm{d}x\mathrm{d}z)/[L_x L_z (T_{\text{L}} - T_{\text{R}})]$, where $L_y = 1100$ nm denotes the total thickness of the film in the y direction, and $L_x = L_z = (87\ \text{nm} + L_s)$ represent the sizes of the physical model in x and z directions. To obtain the thermal boundary conductance, referring to the approach in Ref. [11], the above physical model is treated as a one-dimensional model. For simplicity, the boundary and intrinsic resistances are assumed to be the same for films with planar and nanostructured interfaces at the same total thickness and volume ratio and the same interface roughness, as done in Eq. (52). Thus, the thermal boundary conductance for nanostructured interfaces can be derived as before.

Figures 24 gives the thermal conductivities and thermal boundary conductances obtained by the present simulation for Al/Si at interface roughnesses being 0 nm and infinity. Those for interface roughness being 0.3 nm are shown in Figs. 25(a) and 25(c), with comparisons with experiment [11]. For the experiment, only thermal boundary conductance was provided in the original data [11]. Its thermal conductivities for planar and nanostructured interfaces are approximately calculated based on the one-dimensional model for thermal resistance in this paper as Eq. (52). The R_0 in Eq. (52) equals $(L_{\text{Al}}/\kappa_{\text{Al}} + L_{\text{Si}}/\kappa_{\text{Si}})$ with the thicknesses of Al and Si being $L_{\text{Al}} = 100$ nm and $L_{\text{Si}} = 1000$ nm, and the bulk thermal conductivities of Al and Si, κ_{Al} and κ_{Si}, calculated based on the above dispersions and relaxation times. The bulk thermal conductivity of Al is selected as its lattice thermal conductivity since only phonon transport is considered in the present simulation. The G_{eff} in Eq. (52) for each film with the planar or nanostructured interface is taken as the average value of its error bar from the experiment [11]. This one-dimensional model for thermal resistance is roughly consistent with that in the experiment since, in the experiment, the bulk thermal conductivities of Al and Si were also used to fit to obtain the thermal boundary conductance [11]. For interface roughness being 0.3 nm and infinity, only the thermal boundary conductances with pillar spacings as 104 and 148 nm are shown due to the remaining thermal boundary conductances being negative. The negative thermal boundary conductance is caused by the inappropriateness of two assumptions, i.e., one-dimensional thermal transport, and identical boundary and intrinsic resistances for planar and nanostructured interfaces. Given the enhancement of the thermal conductivity, despite the inappropriateness of the assumptions, it can still be concluded that the nanostructured interface can enhance interfacial phonon transport and the thermal boundary conductance. Figures 25(b) and 25(d) give the enhancement ratios by the nanostructured interface, calculated through $(\kappa_{\text{eff,nano}} - \kappa_{\text{eff,planar}})/\kappa_{\text{eff,planar}}$ and $(G_{\text{eff,nano}} - G_{\text{eff,planar}})/G_{\text{eff,planar}}$, where $\kappa_{\text{eff,planar}}$ and $\kappa_{\text{eff,nano}}$ denote the thermal conductivities of the planar and nanostructured interfaces, and $G_{\text{eff,planar}}$ and $G_{\text{eff,nano}}$ are their thermal boundary conductances. The enhancements of both thermal conductivity and thermal boundary conductance by nanostructured interfaces are found from the results compared with the planar interface.

To further verify the above conclusion, Ge/Si is simulated in the above physical model with the volume ratio as 1(Ge) : 10(Si), whose dispersions and relaxation times are adopted as before. Figure 26 shows the results for the thermal conductivity and thermal boundary conductance at three interface roughnesses as 0 nm, 0.3 nm, and infinity. Similarly, both thermal conductivity and thermal boundary conductance are enhanced by nanostructured interfaces at all interface roughnesses. Therefore, it is concluded that the nanostructured interface always promotes thermal transport at each interface roughness in films with large size, which can be attributed to the additional thermal conduction pathway by increasing the contact area, as explained in Refs. [11,13–15]. Thus, the additional thermal conduction pathway by nanostructured interfaces is the dominant impact factor in large systems.

Totally, the above investigations indicate that the previous contradictory conclusions for the impact of nanostructured interfaces on the thermal boundary conductance or interfacial phonon transport were caused by the combined effect of the interface roughness and the additional thermal conduction pathway. In large systems, the additional thermal conduction pathway by the nanostructured interface dominates over the interface roughness. Thus, the thermal boundary conductance or interfacial phonon transport is always enhanced, like the macroscale fin arrays for the enhancement of heat transfer between solid surfaces and fluids. In small systems, the effect of interface roughness prevails over that of the additional thermal conduction pathway, and the interface roughness determines whether the nanostructured interface can enhance or reduce the thermal boundary conductance or interfacial phonon transport. At small and large interface roughnesses, the nanostructured interface will enhance and reduce the thermal boundary conductance or interfacial phonon transport, respectively. Further underlying mechanisms for the impact of the

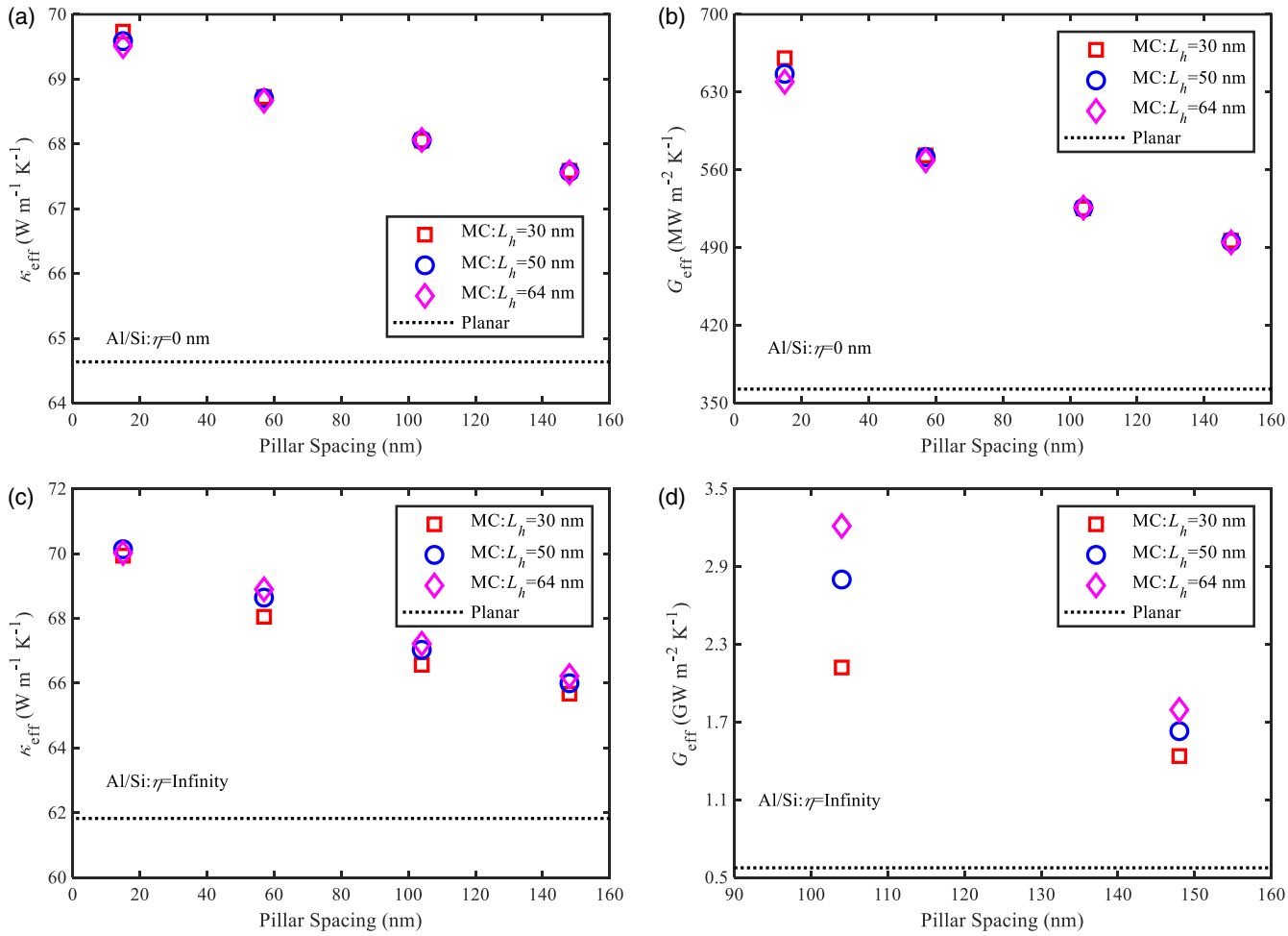

FIG. 24. The comparisons of the thermal conductivity and thermal boundary conductance of Al/Si with various nanostructured interfaces and the planar interface at two interface roughnesses: (a) thermal conductivity at the interface roughness as 0 nm, (b) thermal boundary conductance at the interface roughness as 0 nm, (c) thermal conductivity at the interface roughness as infinity, and (d) thermal boundary conductance at the interface roughness as infinity.

interface roughness in small systems will be analyzed in the following subsection. Particularly Figs. 21 and 22 indicate that the maximum and minimum thermal boundary conductances are still obtained by planar interfaces over the entire range of interface roughness. Combined with the underlying mechanisms, the next subsection will finally propose an effective way to break through these maximum and minimum values using nanostructured interfaces in small systems.

D. Nanostructured interface with nonuniform roughness

The nanostructured interface consists of two kinds of interfaces, i.e., the horizontal and vertical interfaces, parallel and perpendicular to the direction of the heat flux. In this subsection, we investigate the impact of roughness dependence of these two kinds of interfaces on phonon-interface thermal transport in small systems. Based on this impact, an effective way will be provided to expand the manipulation of the thermal boundary conductance through nanostructured interfaces for small systems. Three types of nanostructured interfaces are simulated as well, shown in Fig. 18. The interfaces are also formed by Al/Si and Ge/Si with the same dispersions and relaxation times as before and volume ratios as 1. With the same reason in the previous part, two total thicknesses of films are set to $L = 40$ and 60 nm with the numbers of energy packets being 40 million and 60 million. The boundary temperatures on the left and right sides are kept at $T_L = 303$ K and $T_R = 297$ K. To investigate the impact, the roughness of one interface is fixed, and that of the other is varied; that is, the roughness of the nanostructured interface is nonuniform. For one case, the roughnesses of the horizontal interfaces are fixed at 0.14 nm, and those of the vertical interfaces are varied from 0.02 to 0.2 nm with a common difference 0.02 nm and from 0.2 to 1.8 nm with a common difference 0.2 nm. For the other case, the roughnesses of the vertical interfaces are fixed at 0.14 nm, and those of the horizontal interfaces are varied from 0.02 to 0.2 nm with a common difference 0.02 nm and from 0.2 to 1.8 nm with a common difference 0.2 nm.

Figures 27 and 28 give the thermal conductivities of Al/Si and Ge/Si bilayer films with nanostructured interfaces at various roughnesses of horizontal and vertical interfaces. The thermal conductivities of planar interfaces with the same roughness as the vertical interface are also given for comparisons. The results indicate that the thermal conduc-

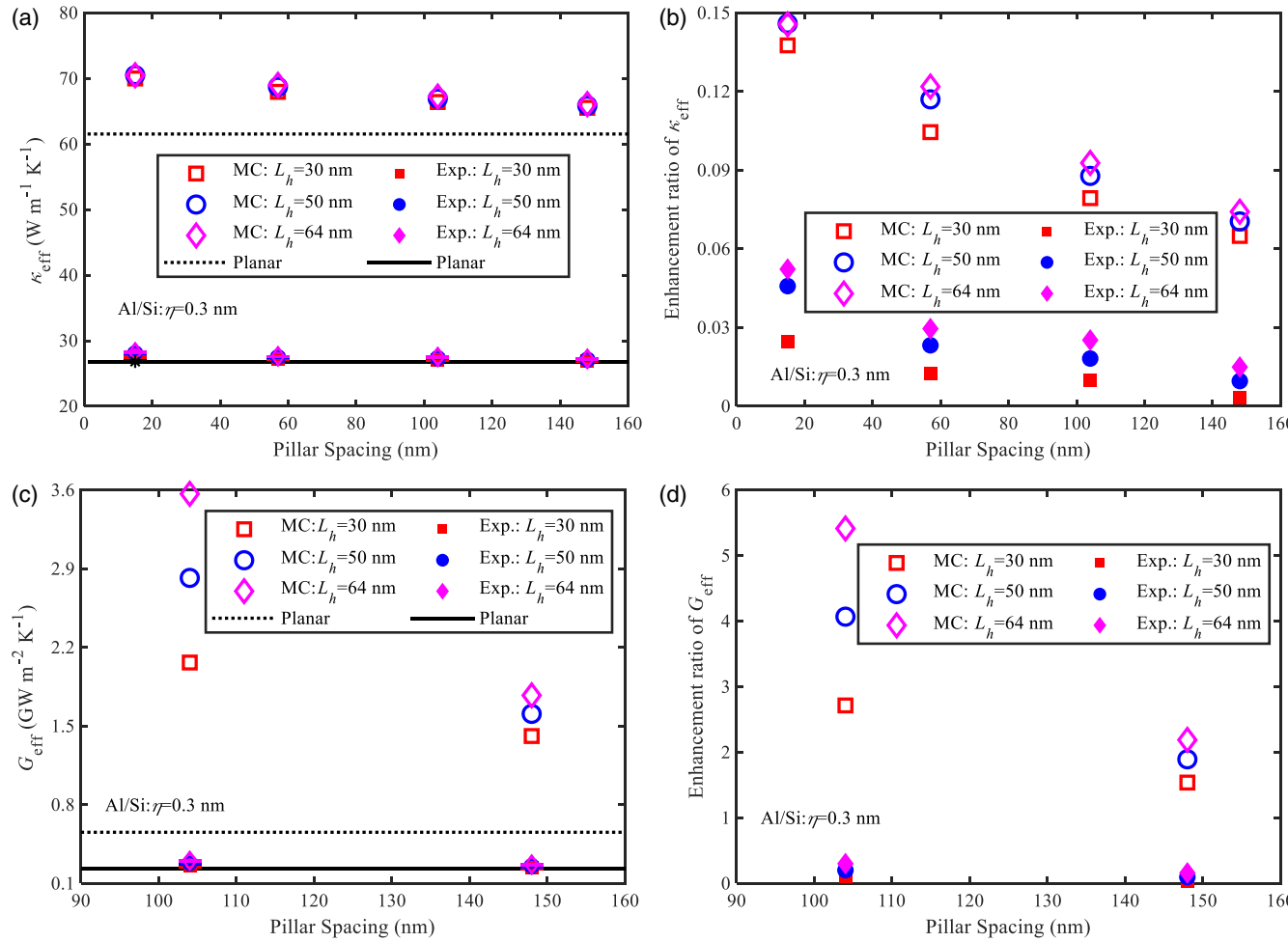

FIG. 25. The comparisons of the thermal conductivity and thermal boundary conductance of Al/Si with various nanostructured interfaces and the planar interface at the interface roughness as 0.3 nm: (a) thermal conductivity, (b) enhancement ratio of thermal conductivity, (c) thermal boundary conductance, and (d) enhancement ratio of thermal boundary conductance. Exp. refers to the data by experiments.

tivity varies differently with the roughness of horizontal and vertical interfaces. To focus on the impact of nanostructured interfaces, the thermal boundary conductances are calculated based on the one-dimensional model, i.e., Eq. (52). Here, R_0 of nanostructured interfaces are taken as R_0 of planar interfaces with the same roughness as their vertical interfaces. Figures 29 and 30 show the results with an analogous conclusion for the thermal conductivity, namely, that different variation trends are found for horizontal and vertical interfaces. In detail, for Al/Si, when fixing the roughness of the horizontal interface and increasing that of the vertical interface, the thermal boundary conductance first increases, next decreases, and then increases, ultimately tending to a constant. This trend is analogous to that of planar interfaces for Al/Si, whereas when fixing the roughness of the vertical interface and increasing that of the horizontal interface, the thermal boundary conductance first decreases and ultimately tends to a constant. For Ge/Si, when fixing the roughness of the horizontal interface and increasing that of the vertical interface, the thermal boundary conductance first decreases, then increases, ultimately tending to a constant. This trend is also analogous to that of planar interfaces for Ge/Si. When fixing the roughness of the vertical interface and increasing that of the horizontal interface, the thermal boundary conductance first decreases and tends to a constant for 6 × 6 nm square and 3 × 6 nm rectangle interfaces. However, for the 9 × 6 nm rectangle interface, the thermal boundary conductance first decreases, then slightly increases, and ultimately tends to a constant, different from other two types of nanostructured interfaces, which is caused by different geometries. Totally, for these two material pairs, when varying the roughness of the vertical interface, the maximum and minimum thermal boundary conductances are obtained at larger and smaller interface roughnesses, respectively. However, when varying the roughness of the horizontal interface, the maximum and minimum thermal boundary conductances are obtained at smaller and larger interface roughnesses, respectively.

Therefore, in small systems, the smaller the roughness of the horizontal interface and the larger the roughness of the vertical interface, the more favorable for thermal transport. Since the effect of interface roughness prevails over that of the additional thermal conduction pathway for small systems, this contrary impact can be explained by the physical figures for specularly and diffusely scattering with two kinds of inter-

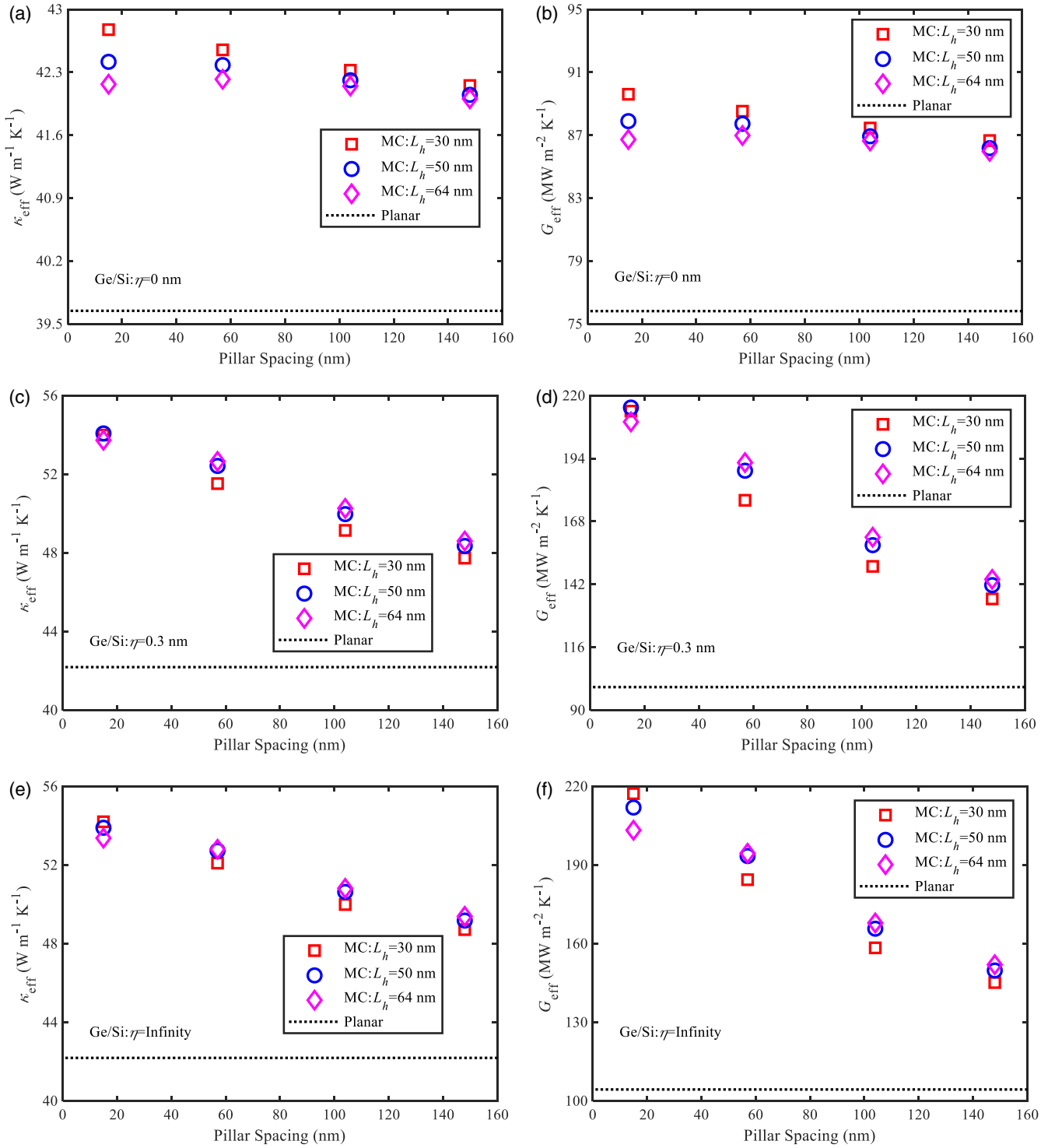

FIG. 26. The thermal conductivity and thermal boundary conductance of Ge/Si with various nanostructured interfaces and the planar interface at three interface roughnesses: (a) thermal conductivity at the interface roughness as 0 nm, (b) thermal boundary conductance at the interface roughness as 0 nm, (c) thermal conductivity at the interface roughness as 0.3 nm, (d) thermal boundary conductance at the interface roughness as 0.3 nm, (e) thermal conductivity at the interface roughness as infinity, and (f) thermal boundary conductance at the interface roughness as infinity.

faces, shown in Fig. 31. When a phonon is specularly scattered by the horizontal interface, as Fig. 31(a) shows, the reflected or transmitted phonon will conserve the momentum along the direction of the heat flux. Thus, specularly scattering with the horizontal interface does not pose the thermal resistance in the direction of the heat flux. When a phonon is diffusely scattered by the horizontal interface, as Fig. 31(c) shows, the momentum of the reflected or transmitted phonon along the direction

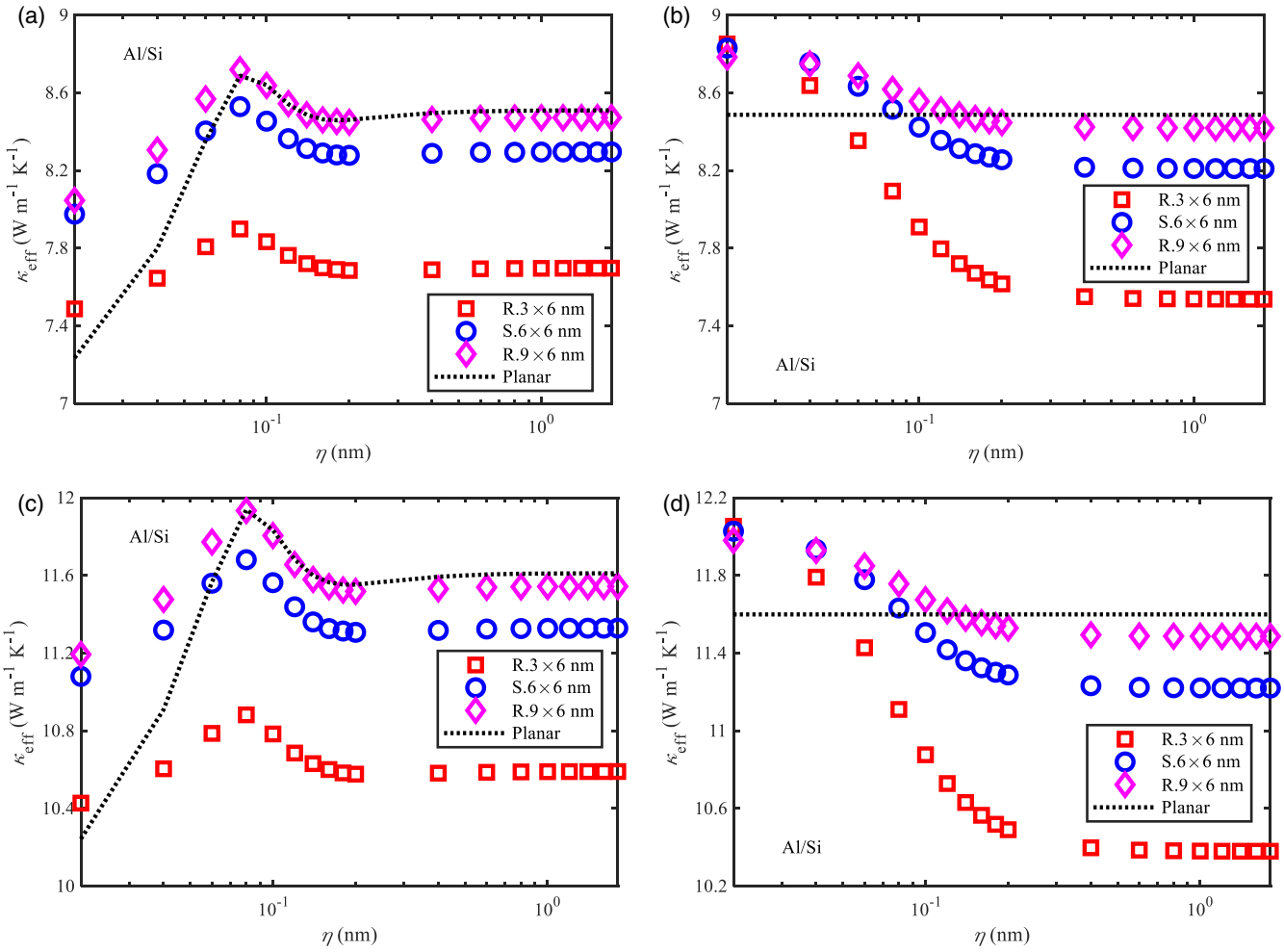

FIG. 27. The thermal conductivity of Al/Si bilayer film with the nanostructured interface with nonuniform roughness: (a) total thickness as 40 nm, fixing the roughnesses of horizontal interfaces at 0.14 nm and varying those of vertical interfaces; (b) total thickness as 40 nm, fixing the roughnesses of vertical interfaces at 0.14 nm and varying those of horizontal interfaces; (c) total thickness as 60 nm, fixing the roughnesses of horizontal interfaces at 0.14 nm and varying those of vertical interfaces; and (d) total thickness as 60 nm, fixing the roughnesses of vertical interfaces at 0.14 nm and varying those of horizontal interfaces.

of heat flux possibly changes. Thus, diffusely scattering with the horizontal interface poses the thermal resistance in the direction of the heat flux because of the resistive scattering. It is inferred that the thermal resistance posed by the horizontal interface decreases with decreasing proportion of the diffuse scattering and thus decreasing interface roughness, whereas for the vertical interface, both specular and diffuse scatterings do not conserve the momentum along the heat flux, shown in Figs. 31(b) and 31(d), consequently contributing to the thermal resistance. The influence of its roughness on thermal transport is like that of planar interfaces in Sec. IV B, namely, a larger interface roughness is more conducive to thermal transport, and it strongly depends on the dispersions of the material pairs. Totally, the contrary impacts of the interface roughness on thermal transport are caused by contrary impacts of specularly and diffusely scattering on thermal resistances with these two kinds of interfaces. Based on this, the impact of the interface roughness in small systems mentioned at the end of the previous subsection is explained as follows: Compared with the planar interface, the nanostructured interface has not only vertical interfaces but also horizontal interfaces. At small interface roughnesses, the horizontal interface poses the small thermal resistance but results in the additional thermal conduction pathway for phonon transport. Hence, in this case, the nanostructured interface enhances the thermal boundary conductance and promotes thermal transport, whereas at large interface roughnesses, the horizontal interface results in both large thermal resistance and additional thermal conduction pathway. In small systems, the impact of this large thermal resistance prevails over that of the additional thermal conduction pathway, and thus, the nanostructured interface reduces the thermal boundary conductance and deteriorates thermal transport at large interface roughnesses.

Based on the results and analyses above, nonuniform roughness of the horizontal and vertical interfaces is proposed to break through the maximum and minimum thermal boundary conductances by planar interfaces, mentioned at the end of the previous subsection. To confirm this proposal, the interface roughnesses are set as follows in the simulations: (a) to break through the maximum thermal

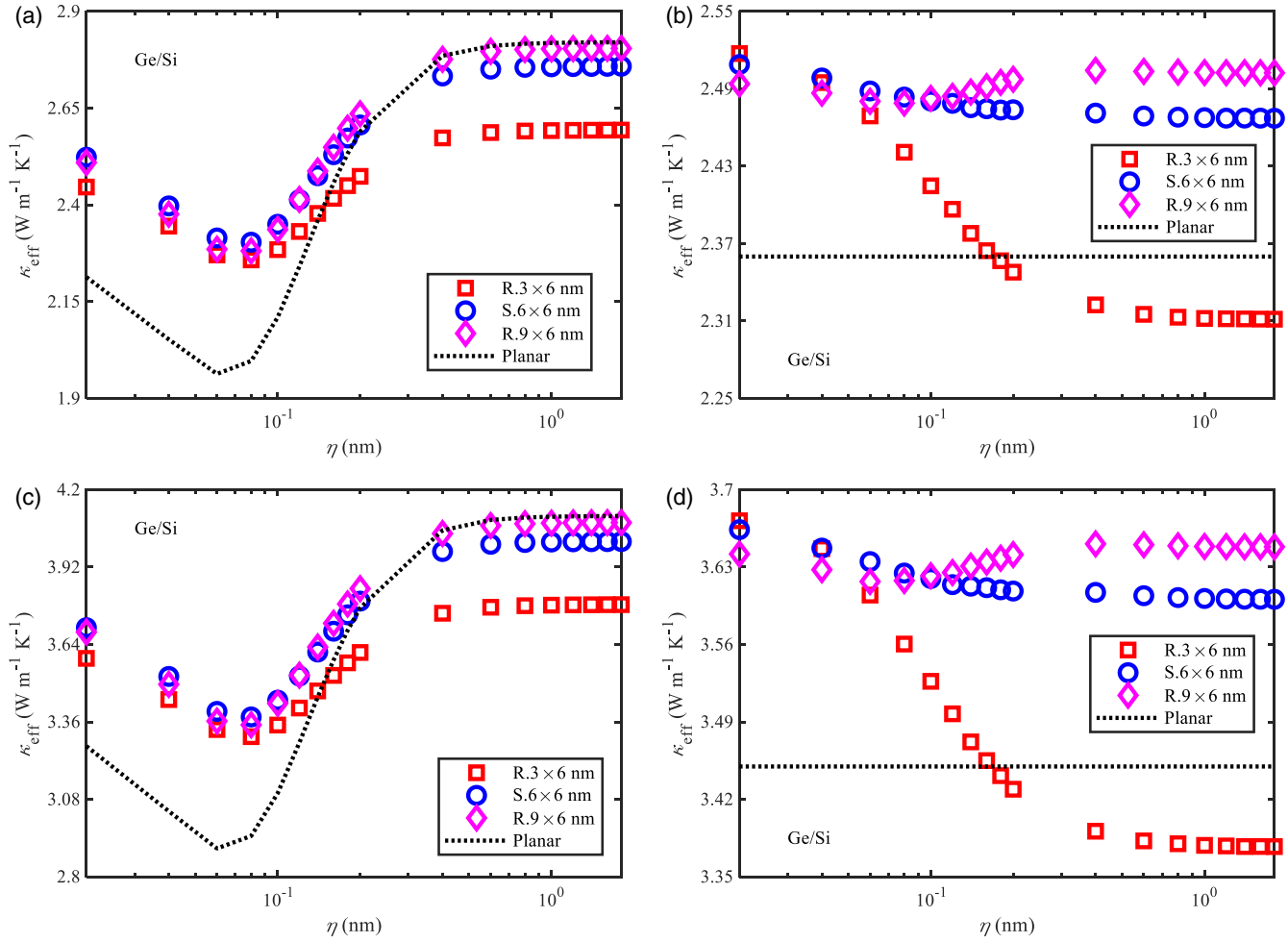

FIG. 28. The thermal conductivity of Ge/Si bilayer films with the nanostructured interface with nonuniform roughness: (a) total thickness as 40 nm, fixing the roughnesses of horizontal interfaces at 0.14 nm and varying those of vertical interfaces; (b) total thickness as 40 nm, fixing the roughnesses of vertical interfaces at 0.14 nm and varying those of horizontal interfaces; (c) total thickness as 60 nm, fixing the roughnesses of horizontal interfaces at 0.14 nm and varying those of vertical interfaces; and (d) total thickness as 60 nm, fixing the roughnesses of vertical interfaces at 0.14 nm and varying those of horizontal interfaces.

boundary conductance, the horizontal and vertical interfaces are considered as completely specular scattering and completely diffuse scattering, respectively, for both Al/Si and Ge/Si; (b) to break through the minimum thermal boundary conductance, the horizontal and vertical interfaces for Al/Si are considered as completely diffuse scattering and completely specular scattering, respectively, but those for Ge/Si are considered as completely diffuse scattering and partially specular and partially diffuse scattering with $\eta =$ 0.06 nm, respectively. Table I presents the results of the maximum and minimum thermal boundary conductances of nanostructured interfaces with nonuniform roughness, where as a comparison, the results of planar interfaces and nanostructured interfaces with uniform roughness are also given. For nanostructured interfaces with nonuniform roughness, the thermal boundary conductances are expanded to a wider range. They can not only be larger than the maximum values of planar interfaces but also smaller than their minimum values. Although nanostructured interfaces with uniform roughness can either increase or decrease the thermal boundary conductance in small systems, the maximum or minimum value still cannot be broken through. Therefore, the nanostructured interface with nonuniform roughness is a more effective way to manipulate the thermal boundary conductance than that with uniform roughness for small systems.

Even though the interface heights are the same, the results for three types of nanostructured interfaces are different from each other, suggesting the geometry as another factor affecting the thermal boundary conductance. Hence, it is inferred that the thermal boundary conductances for nonuniform roughness in Table I are not the maximum and minimum values that can be achieved by the nanostructured interface. By optimizing the geometry or other roughness combinations for horizontal and vertical interfaces, the manipulation of thermal boundary conductance can be further expanded. The impact of the geometry of nanostructured interfaces on thermal boundary conductance at various roughnesses and corresponding optimization measures are not the primary focus in this paper, so it is not discussed in detail.

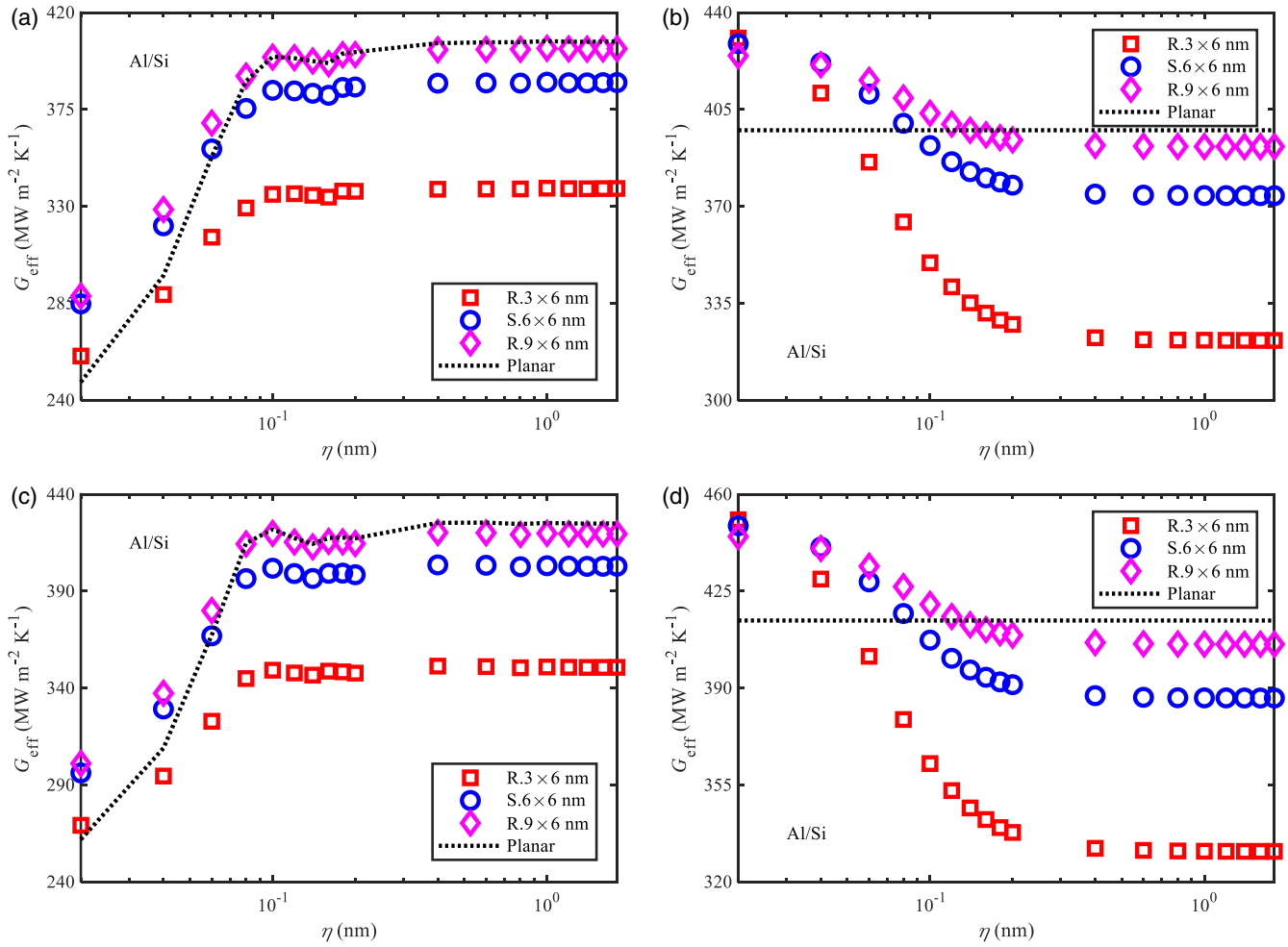

FIG. 29. The thermal boundary conductance of Al/Si bilayer film with the nanostructured interface with nonuniform roughness: (a) total thickness as 40 nm, fixing the roughnesses of horizontal interfaces at 0.14 nm and varying those of vertical interfaces; (b) total thickness as 40 nm, fixing the roughnesses of vertical interfaces at 0.14 nm and varying those of horizontal interfaces; (c) total thickness as 60 nm, fixing the roughnesses of horizontal interfaces at 0.14 nm and varying those of vertical interfaces; and (d) total thickness as 60 nm, fixing the roughnesses of vertical interfaces at 0.14 nm and varying those of horizontal interfaces.

TABLE I. The comparison of thermal boundary conductances of nanostructured interfaces with nonuniform and uniform roughnesses and planar interfaces. The abbreviations Max., Min., Nonuni., and Uni. refer to maximum, minimum, nonuniform, and uniform, respectively. The unit for thermal boundary conductance is MW/(m^2 K).

	Planar	3 × 6 nm rectangle		6 × 6 nm square		9 × 6 nm rectangle	
	Max./Min.	Nonuni.	Uni. and Max./Min.	Nonuni.	Uni. and Max./Min.	Nonuni.	Uni. and Max./Min.
Al/Si							
40 nm	406.74	444.66	360.23	439.50	393.13	434.32	405.24
	232.80	239.83	254.53	265.99	251.05	270.95	249.01
60 nm	425.39	467.87	379.04	461.96	416.34	456.48	426.72
	242.51	244.01	264.51	272.43	261.18	278.57	258.75
Ge/Si							
40 nm	84.48	88.16	72.47	87.89	79.95	87.48	82.43
	54.09	52.90	63.82	53.25	62.59	51.16	61.29
60 nm	85.43	89.06	73.07	88.88	80.66	88.41	83.27
	54.63	53.23	64.36	53.66	63.10	51.60	61.83

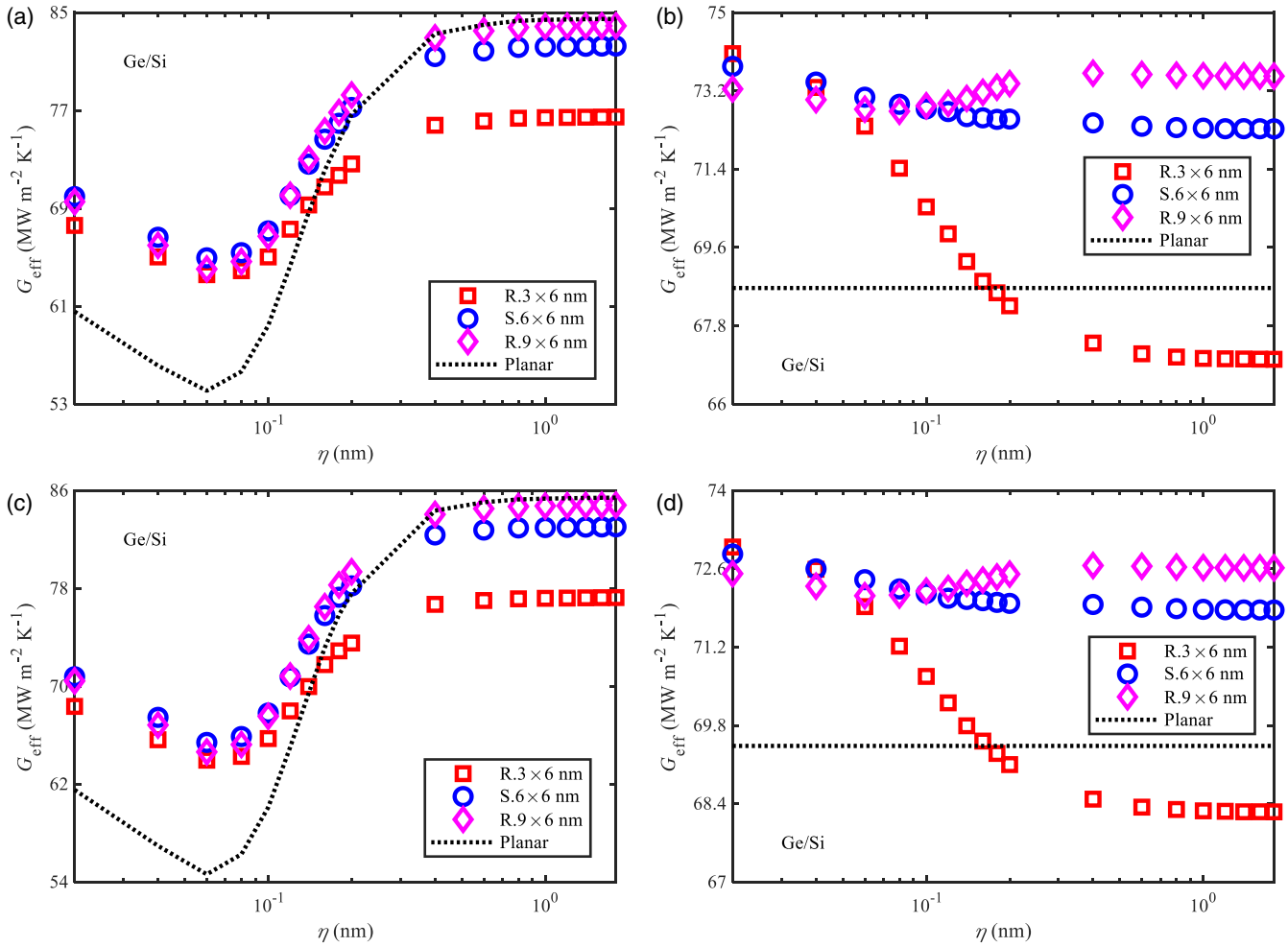

FIG. 30. The thermal boundary conductance of Ge/Si bilayer film with the nanostructured interface with nonuniform roughness: (a) total thickness as 40 nm, fixing the roughnesses of horizontal interfaces at 0.14 nm and varying those of vertical interfaces; (b) total thickness as 40 nm, fixing the roughnesses of vertical interfaces at 0.14 nm and varying those of horizontal interfaces; (c) total thickness as 60 nm, fixing the roughnesses of horizontal interfaces at 0.14 nm and varying those of vertical interfaces; and (d) total thickness as 60 nm, fixing the roughnesses of vertical interfaces at 0.14 nm and varying those of horizontal interfaces.

V. CONCLUSIONS

In summary, in this paper, we have investigated the impact of nanostructured interfaces on thermal boundary conductance via considering roughness dependence. First, an interface model accounting for spectral specularity and spectral specular and spectral diffuse scatterings is deduced based on partially specular and partially diffuse scattering, called the SMMM. Next, the Monte Carlo framework of interface treatment for spectral specularity and spectral specular and spectral diffuse scatterings is developed based on SMMM. Then they are validated by comparisons with the discrete-ordinates method and experiments. Finally, implementing this interface model and the Monte Carlo method, interfacial phonon transport across the planar and nanostructured interfaces are sequentially studied. The results mainly show:

(a) Thermal boundary conductance of planar interfaces varies nonmonotonically with roughness, different from the conventional understanding based on the frequency-independent specularity. The maximum and minimum values are obtained at partially specular and partially diffuse scattering, rather than completely specular or completely diffuse scattering. The nonmonotonic dependence of thermal boundary conductance on interface roughness results from the irregular variation of the spectral transmissivity with varying interface roughness, and the dispersions of the material pairs strongly impact this variation and consequently the dependence.

(b) The system and interface geometries and the interface roughness impact the manipulation of thermal boundary conductance by nanostructured interfaces. For large systems, the additional thermal conduction pathway by the nanostructured interface dominates over the interface roughness, and thermal boundary conductance is always enhanced, and thermal transport is always promoted compared with the planar interface, whereas for small systems, the enhancement and reduction of thermal boundary conductance are derived at small and large roughnesses, respectively. This manipulation can be explained by the combined effect of different thermal resistances and additional thermal conduction pathways caused by the horizontal interface under different interface roughnesses. However, the maximum and minimum thermal

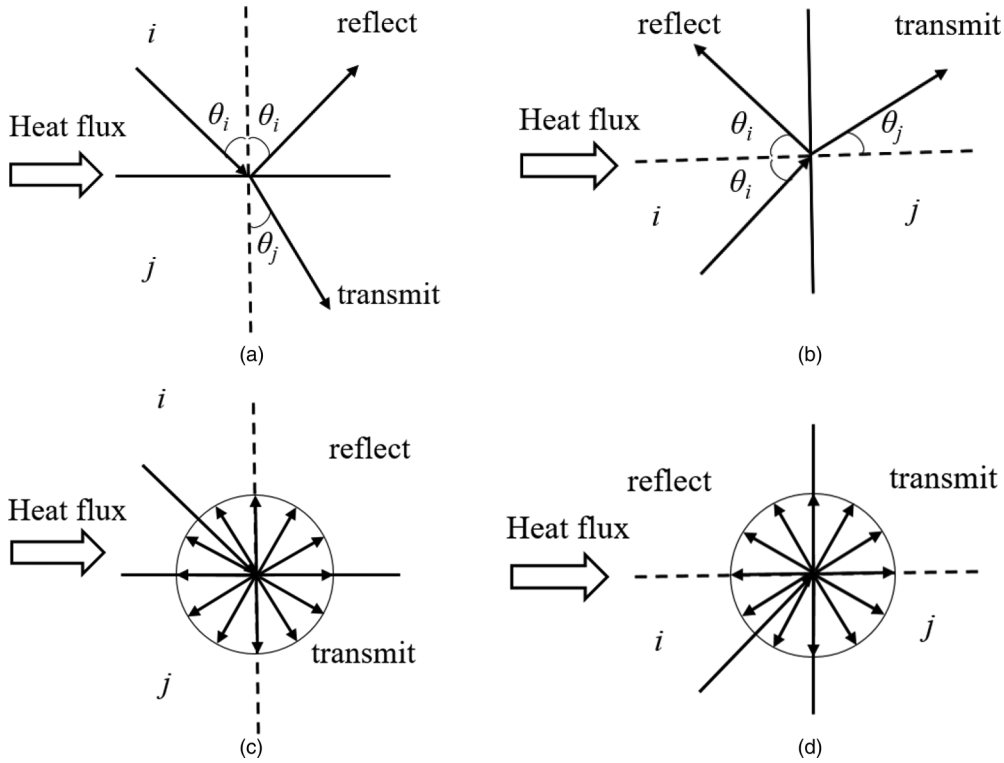

FIG. 31. The physical figure for specularly and diffusely scattering with the horizontal and vertical interfaces: (a) specularly scattering with the horizontal interface, (b) specularly scattering with the vertical interface, (c) diffusely scattering with the horizontal interface, and (d) diffusely scattering with the vertical interface.

boundary conductances are still obtained by planar interfaces rather than nanostructured interfaces.

(c) In small systems, the interface roughnesses of horizontal and vertical interfaces impact thermal boundary conductance of nanostructured interfaces differently. Overall, the smaller the roughness of the horizontal interface and the larger the roughness of the vertical interface, the larger the thermal boundary conductance. Contrary impacts of specularly and diffusely scattering on thermal resistances with the horizontal and vertical interfaces result in this contrary roughness dependence of thermal boundary conductance. Therefore, for small systems, the nonuniform roughness of horizontal and vertical interfaces is proposed, and the maximum and minimum thermal boundary conductances for planar interfaces are successfully broken through, hence expanding the manipulation of thermal boundary conductance.

In this paper, we not only enrich the research means and reveal the fundamental knowledge of interfacial phonon transport, particularly for nanostructured interfaces, but also propose an effective measure to optimize the thermal properties of nanostructured interfaces.

ACKNOWLEDGMENT

This paper was financially supported by the National Natural Science Foundation of China (Grants No. 51825601, No. U20A20301, and No. 52250273).

[1] H. Choi, K. Jeong, J. Chae, H. Park, J. Baeck, T. H. Kim, J. Y. Song, J. Park, K.-Ho. Jeong, and M.-H. Cho, Enhancement in thermoelectric properties of Te-embedded Bi_2Te_3 by preferential phonon scattering in heterostructure interface, Nano Energy **47**, 374 (2018).

[2] K. Ren, H. Qin, H. Liu, Y. Chen, X. Liu, and G. Zhang, Manipulating interfacial thermal conduction of 2D Janus heterostructure via a thermo-mechanical coupling, Adv. Funct. Mater. **32**, 2110846 (2022).

[3] J. Chen, X. Xu, J. Zhou, and B. Li, Interfacial thermal resistance: Past, present, and future, Rev. Mod. Phys. **94**, 025002 (2022).

[4] B. Benbakhti, A. Soltani, K. Kalna, M. Rousseau, and J.-C. De Jaeger, Effects of self-heating on performance degradation in AlGaN/GaN-Based devices, IEEE Trans. Electron Devices **56**, 2178 (2009).

[5] L. W. da Silva and M. Kaviany, Micro-thermoelectric cooler: Interfacial effects on thermal and electrical transport, Int. J. Heat Mass Transfer **47**, 2417 (2004).

[6] P. E. Hopkins, L. M. Phinney, J. R. Serrano, and T. E. Beechem, Effects of surface roughness and oxide layer on the thermal boundary conductance at aluminum/silicon interfaces, Phys. Rev. B **82**, 085307 (2010).

[7] P. E. Hopkins, J. C. Duda, C. W. Petz, and J. A. Floro, Controlling thermal conductance through quantum dot roughening at interfaces, Phys. Rev. B **84**, 035438 (2011).

[8] M. Hu, X. Zhang, D. Poulikakos, and C. P. Grigoropoulos, Large "near junction" thermal resistance reduction in electronics by interface nanoengineering, Int. J. Heat Mass Transfer **54**, 5183 (2011).

[9] X. W. Zhou, R. E. Jones, C. J. Kimmer, J. C. Duda, and P. E. Hopkins, Relationship of thermal boundary conductance to structure from an analytical model plus molecular dynamics simulations, Phys. Rev. B **87**, 094303 (2013).

[10] E. Lee, T. Zhang, M. Hu, and T. Luo, Thermal boundary conductance enhancement using experimentally achievable nanostructured interfaces—Analytical study combined with molecular dynamics simulation, Phys. Chem. Chem. Phys. **18**, 16794 (2016).

[11] E. Lee, T. Zhang, T. Yoo, Z. Guo, and T. Luo, Nanostructures significantly enhance thermal transport across solid interfaces, ACS Appl. Mater. Interfaces **8**, 35505 (2016).

[12] X. Ran, Y. Guo, and M. Wang, Interfacial phonon transport with frequency-dependent transmissivity by Monte Carlo simulation, Int. J. Heat Mass Transfer **123**, 616 (2018).

[13] W. Park, A. Sood, J. Park, M. Asheghi, R. Sinclair, and K. E. Goodson, Enhanced thermal conduction through nanostructured interfaces, Nanoscale Microscale Thermophys. Eng. **21**, 134 (2017).

[14] E. Lee, E. Menumerov, R. A. Hughes, S. Neretina, and T. Luo, Low-cost nanostructures from nanoparticle-assisted large-scale lithography significantly enhance thermal energy transport across solid interfaces, ACS Appl. Mater. Interfaces **10**, 34690 (2018).

[15] Z. Cheng, T. Bai, J. Shi, T. Feng, Y. Wang, M. Mecklenburg, C. Li, K. D. Hobart, T. I. Feygelson, M. J. Tadjer *et al.*, Tunable thermal energy transport across diamond membranes and diamond-Si interfaces by nanoscale graphoepitaxy, ACS Appl. Mater. Interfaces **11**, 18517 (2019).

[16] X. Zhao, X. Qian, X. Li, and R. Yang, Thermal conductance of nanostructured interfaces from Monte Carlo simulations with *ab initio*-based phonon properties, J. Appl. Phys. **129**, 215105 (2021).

[17] E. Yin, Q. Li, and W. Lian, Mechanisms for enhancing interfacial phonon thermal transport by large-size nanostructures, Phys. Chem. Chem. Phys. **25**, 3629 (2023).

[18] W. Little, The transport of heat between dissimilar solids at low temperatures, Can. J. Phys. **37**, 334 (1959).

[19] E. T. Swartz and R. O. Pohl, Thermal boundary resistance, Rev. Mod. Phys. **61**, 605 (1989).

[20] G. Chen, Thermal conductivity and ballistic-phonon transport in the cross-plane direction of superlattices, Phys. Rev. B **57**, 14958 (1998).

[21] C. Hua, X. Chen, N. K. Ravichandran, and A. J. Minnich, Experimental metrology to obtain thermal phonon transmission coefficients at solid interfaces, Phys. Rev. B **95**, 205423 (2017).

[22] P. Jiang, L. Lindsay, X. Huang, and Y. K. Koh, Interfacial phonon scattering and transmission loss in >1 μm thick silicon-on-insulator thin films, Phys. Rev. B **97**, 195308 (2018).

[23] X. Li and R. Yang, Effect of lattice mismatch on phonon transmission and interface thermal conductance across dissimilar material interfaces, Phys. Rev. B **86**, 054305 (2012).

[24] J. C. Duda, P. E. Hopkins, J. L. Smoyer, M. L. Bauer, T. S. English, C. B. Saltonstall, and P. M. Norris, On the assumption of detailed balance in prediction of diffusive transmission probability during interfacial transport, Nanoscale Microscale Thermophys. Eng. **14**, 21 (2010).

[25] B. Liu and V. I. Khvesyuk, Analytical model for thermal boundary conductance based on elastic wave theory, Int. J. Heat Mass Transfer **159**, 120117 (2020).

[26] M. Kazan, Interpolation between the acoustic mismatch model and the diffuse mismatch model for the interface thermal conductance: Application to InN/GaN superlattice, J. Heat Transfer **133**, 112401 (2011).

[27] Y. Zhang, D. Ma, Y. Zang, X. Wang, and N. Yang, A modified theoretical model to accurately account for interfacial roughness in predicting the interfacial thermal conductance, Front. Energy Res. **6**, 1 (2018).

[28] J.-Y. Lin and M.-J. Huang, An investigation into the roughness and film thickness effects on the interfacial thermal resistance, Nanoscale Microscale Thermophys. Eng. **27**, 149 (2023).

[29] X. Gu, Z. Fan, and H. Bao, Thermal conductivity prediction by atomistic simulation methods: Recent advances and detailed comparison, J. Appl. Phys. **130**, 210902 (2021).

[30] Y. Guo, Z. Zhang, M. Bescond, S. Xiong, M. Nomura, and S. Volz, Anharmonic phonon-phonon scattering at the interface between two solids by nonequilibrium Green's function formalism, Phys. Rev. B **103**, 174306 (2021).

[31] P. R. Chowdhury, J. Shi, T. Feng, and X. Ruan, Prediction of Bi_2Te_3-Sb_2Te_3 interfacial conductance and superlattice thermal conductivity using molecular dynamics simulations, ACS Appl. Mater. Interfaces **13**, 4636 (2021).

[32] Z. Tian, K. Esfarjani, and G. Chen, Enhancing phonon transmission across a Si/Ge interface by atomic roughness: First-principles study with the Green's function method, Phys. Rev. B **86**, 235304 (2012).

[33] Y. Xiong, X. Yu, Y. Huang, J. Yang, L. Li, N. Yang, and D. Xu, Ultralow thermal conductance of the van der Waals interface between organic nanoribbons, Mater. Today Phys. **11**, 100139 (2019).

[34] H.-A. Yang and B.-Y. Cao, Mode-resolved phonon transmittance using lattice dynamics: Robust algorithm and statistical characteristics, J. Appl. Phys. **134**, 155302 (2023).

[35] H. Zhao and J. B. Freund, Lattice-dynamical calculation of phonon scattering at ideal Si-Ge interfaces, J. Appl. Phys. **97**, 024903 (2005).

[36] Y. Xu, L. Yang, and Y. Zhou, The interfacial thermal conductance spectrum in nonequilibrium molecular dynamics simulations considering anharmonicity, asymmetry and quantum effects, Phys. Chem. Chem. Phys. **24**, 24503 (2022).

[37] H. Ali and B. S. Yilbas, Phonon transport in silicon-diamond thin film Pairs: Consideration of thermal boundary resistance due to cutoff mismatch and diffusive mismatch models, Numer. Heat Transf. A **68**, 1307 (2015).

[38] B. Hu, W. Bao, G. Chen, Z. Wang, and D. Tang, Boltzmann transport equation simulation of phonon transport across GaN/AlN interface, Comput. Mater. Sci. **230**, 112485 (2023).

[39] M.-S. Jeng, R. Yang, D. Song, and G. Chen, Modeling the thermal conductivity and phonon transport in nanoparticle composites using Monte Carlo simulation, J. Heat Transfer **130**, 042410 (2008).

[40] X. Ran and M. Wang, Efficiency improvement of discrete-ordinates method for interfacial phonon transport by Gauss-Legendre integral for frequency domain, J. Comput. Phys. **399**, 108920 (2019).
[41] Z.-K. Liu, G. Yang, and B.-Y. Cao, Pulsed thermoreflectance imaging for thermophysical properties measurement of GaN epitaxial heterostructures, Rev. Sci. Instrum. **94**, 094902 (2023).
[42] M. M. Sadeghi, I. Jo, and L. Shi, Phonon-interface scattering in multilayer graphene on an amorphous support, Proc. Natl. Acad. Sci. USA **110**, 16321 (2013).
[43] G. Yang and B.-y. Cao, Three-sensor 3ω-2ω method for the simultaneous measurement of thermal conductivity and thermal boundary resistance in film-on-substrate heterostructures, J. Appl. Phys. **133**, 045104 (2023).
[44] C. Hua and A. J. Minnich, Importance of frequency-dependent grain boundary scattering in nanocrystalline silicon and silicon-germanium thermoelectrics, Semicond. Sci. Technol. **29**, 124004 (2014).
[45] M.-J. Huang, T.-C. Tsai, L.-C. Liu, M.-s. Jeng, and C.-C. Yang, A fast Monte-Carlo solver for phonon transport in nanostructured semiconductors, Comput. Model. Eng. Sci. **42**, 107 (2009).
[46] Y.-C. Hua and B.-Y. Cao, Study of phononic thermal transport across nanostructured interfaces using phonon Monte Carlo method, Int. J. Heat Mass Transfer **154**, 119762 (2020).
[47] B. Latour, N. Shulumba, and A. J. Minnich, *Ab initio* study of mode-resolved phonon transmission at Si/Ge interfaces using atomistic Green's functions, Phys. Rev. B **96**, 104310 (2017).
[48] T. Maranets and Y. Wang, Ballistic phonon lensing by the non-planar interfaces of embedded nanoparticles, New J. Phys. **25**, 103038 (2023).
[49] M. Martinez, L. Cardani, N. Casali, A. Cruciani, G. Pettinari, and M. Vignati, Measurements and simulations of athermal phonon transmission from silicon absorbers to aluminum sensors, Phys. Rev. Appl. **11**, 064025 (2019).
[50] T. Murakami, T. Hori, T. Shiga, and J. Shiomi, Probing and tuning inelastic phonon conductance across finite-thickness interface, Appl. Phys. Express **7**, 121801 (2014).
[51] J. Wang and J.-S. Wang, Characteristics of phonon transmission across epitaxial interfaces: A lattice dynamic study, J. Phys. Condens. Matter **19**, 236211 (2007).
[52] C. Dames and G. Chen, Theoretical phonon thermal conductivity of Si/Ge superlattice nanowires, J. Appl. Phys. **95**, 682 (2004).
[53] J. M. Ziman, *Electrons and Phonons: The Theory of Transport Phenomena in Solids* (Oxford University Press, London, 2001).
[54] M. F. Modest and S. Mazumder, *Radiative Heat Transfer* (Academic Press, London, 2021).
[55] M. Wang and Z. Li, Nonideal gas flow and heat transfer in micro-and nanochannels using the direct simulation Monte Carlo method, Phys. Rev. E **68**, 046704 (2003).
[56] J.-P. M. Péraud and N. G. Hadjiconstantinou, Efficient simulation of multidimensional phonon transport using energy-based variance-reduced Monte Carlo formulations, Phys. Rev. B **84**, 205331 (2011).
[57] J. Yu, W. Ye, B. Huang, D. J. Villaroman, and Q. Wang, MFP-based Monte Carlo method for nanostructure phonon transport, in *Proceedings of the ASME 2019 6th International Conference on Micro/Nanoscale Heat Transfer* (American Society of Mechanical Engineers, 2019), p. V001T10A006.
[58] L. Maurer, S. Mei, and I. Knezevic, in *Nanophononics: Thermal Generation, Transport, and Conversion at the Nanoscale* (CRC Press, United Kingdom, 2017), pp. 109.
[59] A. Raisi and A. A. Rostami, Unsteady heat transport in direction perpendicular to a double-layer thin-film structure, Numer. Heat Transf. A **41**, 373 (2002).
[60] R. Stedman and G. Nilsson, Dispersion relations for phonons in aluminum at 80 and 300°K, Phys. Rev. **145**, 492 (1966).
[61] Si - Silicon, available from: http://www.ioffe.ru/SVA/NSM/Semicond/Si/mechanic.html
[62] Ge - Germanium, available from: http://www.ioffe.ru/SVA/NSM/Semicond/Ge/mechanic.html
[63] X. Ran and M. Wang, In-plane interfacial phonon transport through multi-layer thin films by theoretical analyses and Monte Carlo simulations, Int. J. Heat Mass Transfer **176**, 121438 (2021).
[64] T. Feng, Y. Zhong, J. Shi, and X. Ruan, Unexpected high inelastic phonon transport across solid-solid interface: Modal nonequilibrium molecular dynamics simulations and Landauer analysis, Phys. Rev. B **99**, 045301 (2019).
[65] X. Li, J. Han, and S. Lee, Thermal resistance from non-equilibrium phonons at Si-Ge interface, Mater. Today Phys. **34**, 101063 (2023).
[66] A. J. Minnich, J. A. Johnson, A. J. Schmidt, K. Esfarjani, M. S. Dresselhaus, K. A. Nelson, and G. Chen, Thermal conductivity spectroscopy technique to measure phonon mean free paths, Phys. Rev. Lett. **107**, 095901 (2011).
[67] C. Monachon, L. Weber, and C. Dames, Thermal boundary conductance: A materials science perspective, Annu. Rev. Mater. Res. **46**, 433 (2016).
[68] J. Maassen and V. Askarpour, Phonon transport across a Si-Ge interface: The role of inelastic bulk scattering, APL Mater. **7**, 013203 (2019).
[69] P. E. Hopkins, J. R. Serrano, L. M. Phinney, S. P. Kearney, T. W. Grasser, and C. T. Harris, Criteria for cross-plane dominated thermal transport in multilayer thin film systems during modulated laser heating, J. Heat Transfer **132**, 081302 (2010).